





# Chapter 4

## The DUNE 35 ton Prototype

The 35 ton is the first experimental prototype of the DUNE far detector design and was briefly introduced in Section 3.5. It was originally constructed to demonstrate the unique design features of the LBNE far detector and was the only planned prototype for this experiment. Following the dissolution of LBNE and the subsequent formation of the DUNE collaboration, the 35 ton has become an integral part of the design and execution of the DUNE far detector design.

As discussed in Section 3.1, the use of LArTPCs in future long-baseline experiments shows great promise. To facilitate development of the detector technology, Fermilab has an extensive program of LArTPC experiments culminating in the flagship DUNE project. Prototyping is essential to the success of DUNE as understanding of how to operate progressively larger detectors evolves. The strategy is staged, with each subsequent phase building on previous success.

The most pertinent issues facing large-scale LArTPCs concern:

- the ability to achieve and maintain the necessary LAr purity for successful data taking;
- the design and construction of huge underground cryostats.

The research and development performed thus far have demonstrated viable solutions to these obstacles and has resulted in the situation where ProtoDUNE can be attempted with confidence.

The outcomes of each of these projects at Fermilab are the subject of this present chapter. The first of the above issues, regarding LAr purity, is discussed in Section 4.1 with reference to the Materials Test Stand and the Liquid Argon Purity Demonstrator. The second complication, concerning the construction of large underground cryostats, was the main motivation for the 35 ton Phase I experiment and is the subject of Section 4.2. The culmination of all these

developments involved operating a small scale LArTPC alongside these improvements and was achieved in the 35 ton Phase II run, discussed in Section 4.3. Since this experiment forms the basis for later chapters, it will be reviewed in much greater detail. A summary of all this R&D is presented in Section 4.4.

## 4.1 The Materials Test Stand and Liquid Argon Purity Demonstrator

The work on developing LArTPCs for future neutrino experiments began at FNAL in 2007 with a view to eventually facilitating a multi-kton LAr experiment. Even utilising a modular design, as with the DUNE far detector (Section 3.3.2), drift distances on the order of a few metres are realistically required, necessitating a low concentration of electronegative impurities. Attaining and holding the requisite LAr purity in a huge underground cryostat over many years of running is a considerable challenge addressed by the test stands reviewed in this section.

### 4.1.1 The Materials Test Stand

The Materials Test Stand (MTS) [111–114] was constructed at FNAL to develop LAr purification techniques and to characterise the effect of various materials on the electron lifetime when submerged in the liquid. It consists of a small cryostat and two filters containing activated-copper-coated granules and an adsorbent molecular sieve respectively; a schematic of the MTS setup is shown in Figure 4.1. The filters are designed to remove oxygen and water contaminants with functionality similar to that successfully demonstrated by the ICARUS collaboration [115]. Oxygen is removed by the copper beads using the chemical reaction



and water molecules are physically trapped in the microporous structure of the sieve. The filters additionally contain the ability to be regenerated in situ, a necessity when planning a long-running experiment, multi-kton experiment; those used previously were primarily proprietary [116, 117].

The MTS successfully demonstrated good argon purity ( $< 3 \text{ ppb H}_2\text{O}$ ) and showed the primary opposition to electron lifetime is water contamination, demonstrated in Figure 4.2. It was found that exposure to warm surfaces in the cryostat, such as above the liquid level, facilitated contamination from water impurities as they remain on surfaces even in a vacuum.

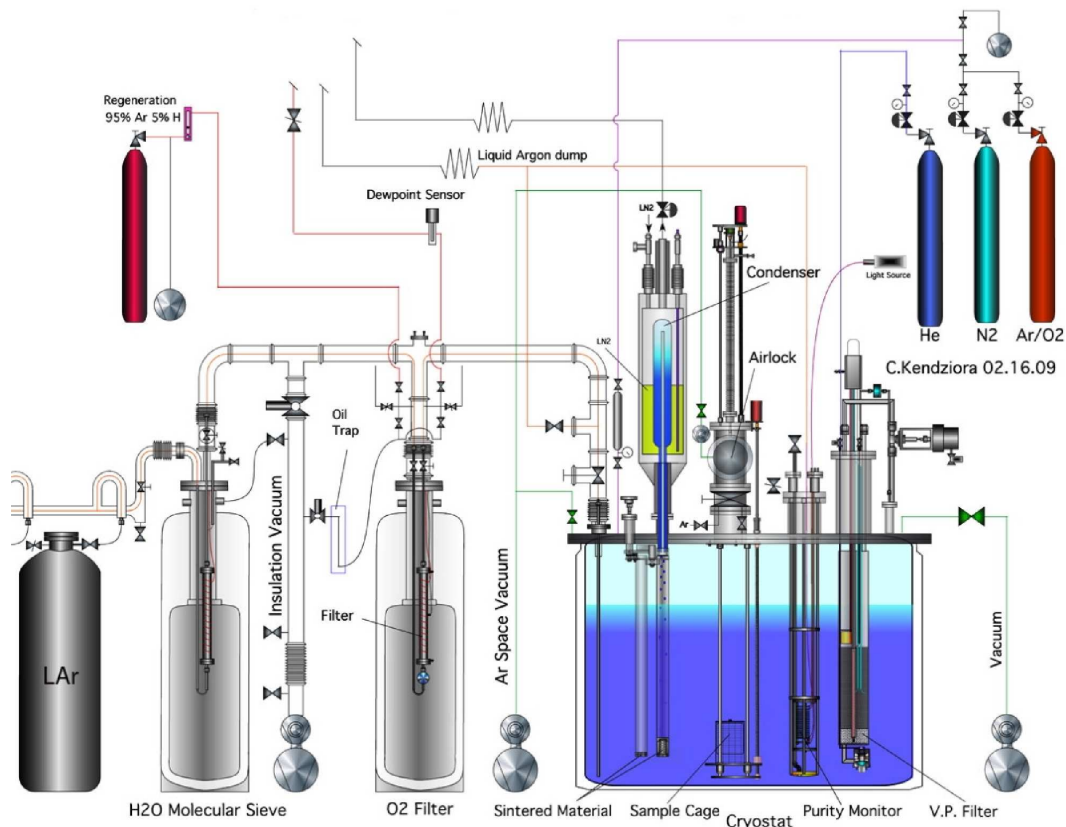


Fig. 4.1 The Materials Test Stand at FNAL [113]. Liquid argon used to fill the cryostat flows from left to right in the schematic, through two filters designed to reduce the H<sub>2</sub>O and O<sub>2</sub> contamination respectively. A second filter system (the ‘vapour pump’ (V.P.)), using the same materials, is installed within the cryostat to remove impurities introduced by the materials being examined.

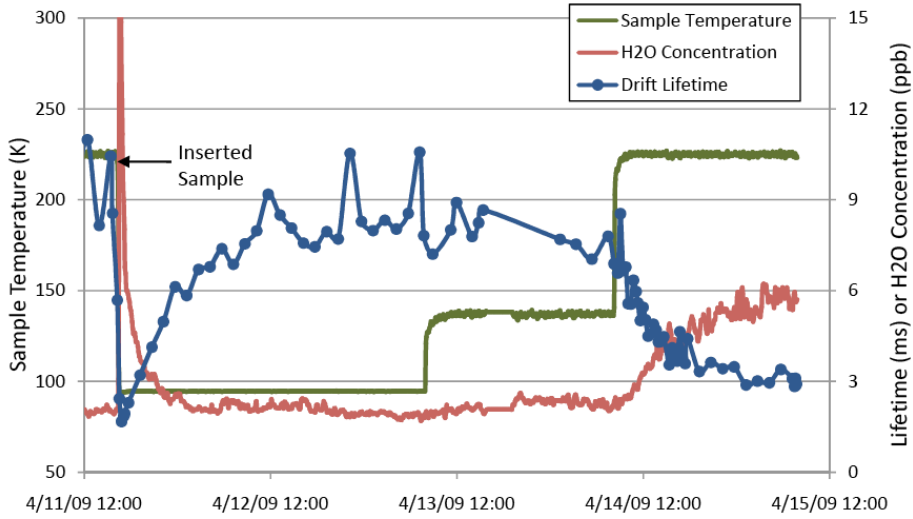


Fig. 4.2 Results from the Materials Test Stand showing the water contamination in LAr and the corresponding electron lifetime [112]. There is an obvious inverse correlation between the density of electronegative ( $\text{H}_2\text{O}$ ) impurities and the resulting lifetime.

The condenser used in the MTS to recondense gaseous argon returned it directly to the liquid in the cryostat (as ‘raining’ condensation) and was found to dramatically reduce the LAr purity when in use. This is due to contaminants introduced into the gas by exposure to the warm croystat walls which could be negated by returning the liquid via a different path which maximised subjection to cold surfaces. Notably, the electron lifetime was found to be unaffected on the introduction of test materials, although as suspected the temperature of the materials did have an impact. This is a hugely promising result for the future of LArTPC design and construction.

#### 4.1.1.1 Filter Regeneration

Over time, the filters become less effective as electronegative impurities accumulate. A significant success of the MTS was demonstrating the process of regenerating the filters in situ. This is achieved by heating the vessels to  $250^\circ\text{C}$  and, in the case of the molecular sieve, simply using a vacuum pump to remove the water vapour or, in the case of the activated copper, by pumping through a 95:5 mixture of Ar:H<sub>2</sub> gas to capture the oxygen through the reduction reaction



During the running of the test stand, the filters were regenerated after the passage of around 1000 litres of liquid argon.

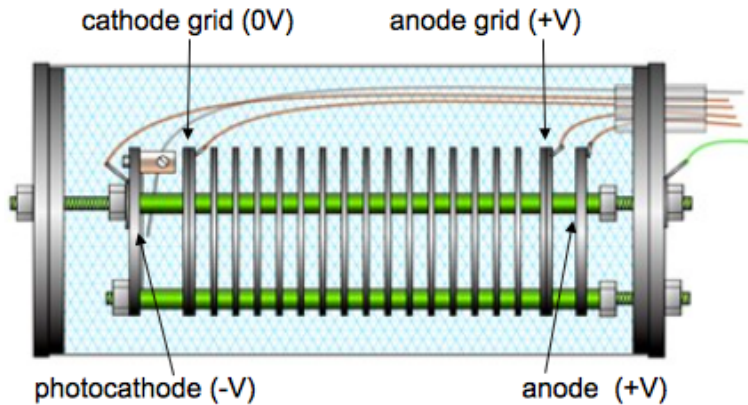


Fig. 4.3 Schematic design of the purity monitors utilised at the FNAL LAr test stands [118]. Purity monitors using this design were pioneered by ICARUS [118] and used in the MTS along with the subsequent Liquid Argon Purity Demonstrator (Section 4.1.2) and 35 ton Runs I (Section 4.2) and II (Section 4.3).

#### 4.1.1.2 Purity Monitoring

The ability to constantly evaluate the LAr purity during an experimental run is hugely important to ensure high quality data. The impurity concentrations are typically beyond the capabilities of many conventional gas analysers and so a custom device, known as a ‘purity monitor’ (PrM), is utilised. The design is based on the purity monitors developed by ICARUS [118] and is shown in Figure 4.3.

The PrM consists of a cylindrical volume containing LAr from its surrounding environment and an anode and photocathode separated by a short drift region. When taking purity measurements, light from a Xenon flash lamp is incident on the cathode, liberating photoelectrons which traverse towards the anode. Electronegative impurities in the LAr will decrease the electron lifetime and therefore the number of electrons reaching a certain point along the drift volume. A measurement of the ratio of the charge arriving at the anode to that at the cathode is hence a measurement of the inherent purity of the liquid.

The MTS cryostat contains a purity monitor and they were subsequently used in the Liquid Argon Purity Demonstrator and the 35 ton. When developed for the Liquid Argon Purity Demonstrator and 35 ton cryostats, two sizes were used; long (47 cm) and short (16 cm).

#### 4.1.2 The Liquid Argon Purity Demonstrator

The Liquid Argon Purity Demonstrator (LAPD) [114, 119, 120] was designed to demonstrate the required purity of LArTPC experiments is possible without the use of large scale vacuum

pumps. Previous and current LArTPC experiments, such as ICARUS, Argoneut, LArIAT and MicroBooNE, have been constructed as flat plane vessels and have used an evacuation method as the first step in removing atmospheric impurities to facilitate the required LAr purity. The necessary mechanical capability of the cryostat to withstand this process, along with the associated equipment, results in unfeasible engineering challenges and costs as detectors increase to multi-kton scales.

In order to circumvent these issues, a design utilising multiple smaller-scale cryostats was proposed. This however leads to greater complexity relating to both the engineering requirements of the piping infrastructure and the reconstruction capabilities of interactions spanning multiple active volumes. LAPD successfully pioneering an alternative approach, using a ‘piston purge’ as a first purification step to remove atmospheric impurities. This is a hugely important result and has significantly influenced the design of future LArTPC experiments, including the 35 ton. Additionally, although designed to be evacuated with vacuum pumps, MicroBooNE was filled using the piston purge technique following the success of LAPD.

#### **4.1.2.1 LAPD Experimental Setup**

The LAPD cryostat is shown in Figure 4.4. It consists of a cylindrical tank, diameter 10 feet and height 10 feet, with a domed head capable of holding 32.6 ton LAr. It is physically next to the MTS and uses the purification system prototyped by this previous effort. Insulation for the tank is provided by fibreglass sheets covering the outer volume which, along with the tank, is refrigerated by liquid nitrogen ( $\text{LN}_2$ ) from an external supply. As with the MTS, a condenser is utilised above the croystat to recondense argon gas using coils also cooled with  $\text{LN}_2$ . This liquid is subsequently sent through the filtration system before being returned to the main volume, a consequense of the previous R&D with the MTS. After filling, the system is closed and a good LAr purity is maintained by constant circulation of the cryostat content through the filters.

The system is instrumented with PrMs, gas analysers and temperature sensors. Four PrMs are contained within the cryostat to measure the purity gradient with an additional one just after the filters to sample to liquid before it is returned to the main volume. Along with purity, the temperature gradient is measured in order to study the effect of this on electron drift velocity. The contaminants in the LAr are quantified using nitrogen, oxygen and water analysers outside of the main volume.

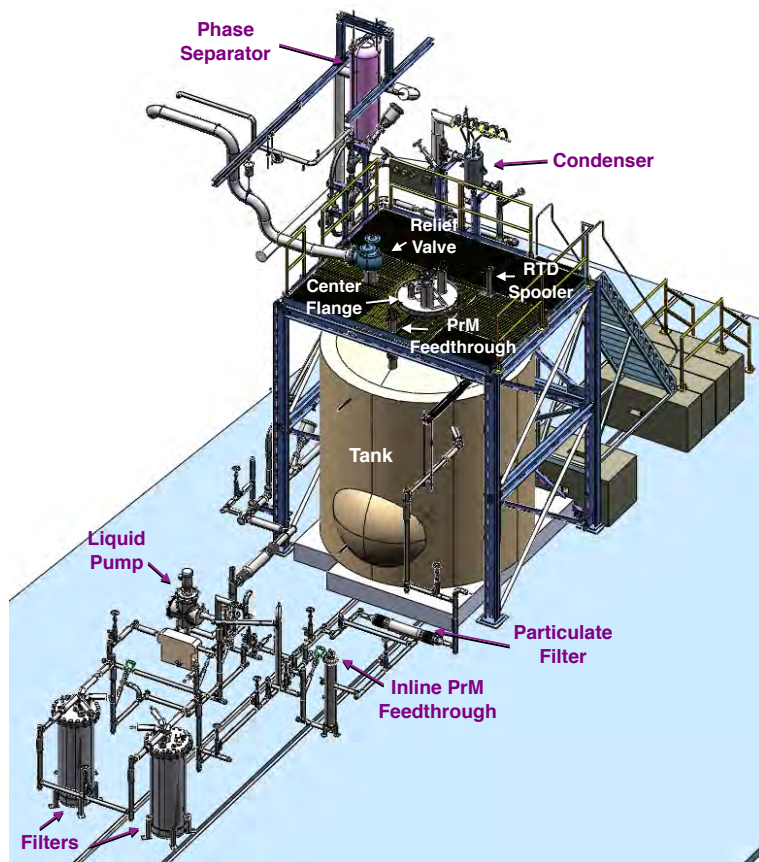
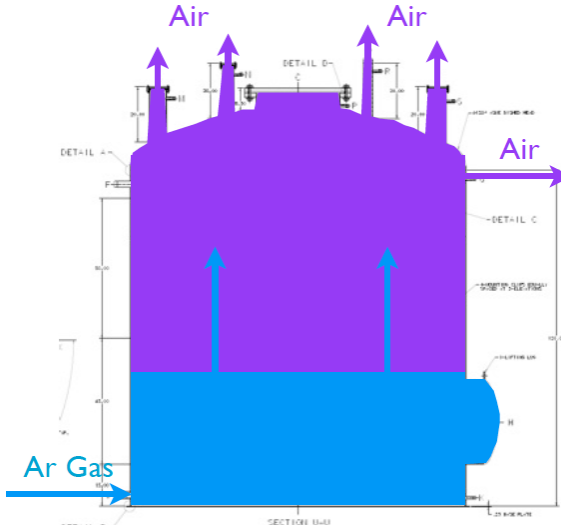
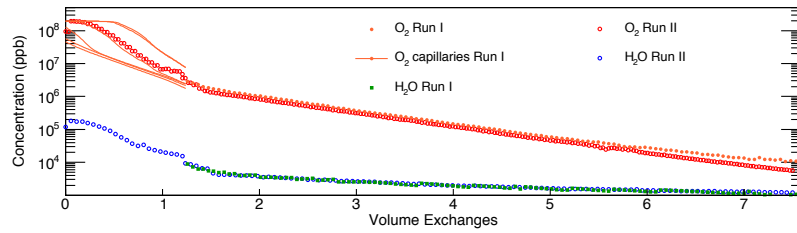


Fig. 4.4 The Liquid Argon Purity Demonstrator cryostat and purification system [120]. The two cylinders at the bottom left are the filters described in Section 4.1.1. The piping facilitates the transport of LAr into and out of the cryostat so continual purification within a closed system may be achieved.



(a) Schematic of the LAPD piston purge.



(b) LAPD impurity concentration during the piston purge.

Fig. 4.5 The piston purge technique in the Liquid Argon Purity Demonstrator to remove atmospheric impurities before filling [120]. The results from two LAPD runs are shown, the first with the cryostat only half filled to prototype the technique. Discontinuities between the impurity concentrations are caused by switches between gas analysers.

#### 4.1.2.2 Filling LAPD

The piston purge technique involves injecting warm argon gas at high pressure at the bottom of the cryostat with the top open for venting, demonstrated in Figure 4.5a. The heavier than air argon gas acts as a piston, forcing the ambient air out of the top of the cryostat. Figure 4.5b demonstrates how this successfully reduces the impurity concentration in the cryostat, shown as a function of complete volume changes. After completion of the piston purging, the O<sub>2</sub> contamination had decreased from 21% to 6 ppm, N<sub>2</sub> from 78% to 18 ppm and H<sub>2</sub>O from 200 ppm to 1.2 ppm.

Following the filling of the cryostat with gaseous argon, the contents are then continually circulated through the filters to further reduce the impurities present. The improved electronegative concentrations are shown, again with reference to the number of complete

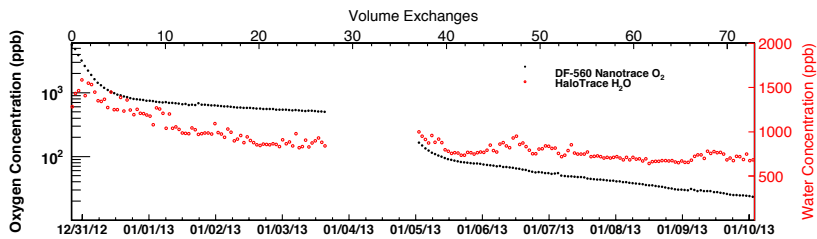


Fig. 4.6 The concentration of electronegative impurities during the gas circulation stage in the Liquid Argon Purity Demonstrator following the piston purge [120]. The stabilisation of the oxygen contamination signified a leak, which was fixed during the break in readings.

volume changes, in Figure 4.6. This lasted, as can also be observed in the figure, for a number of days and resulted in a much improved  $O_2$  contamination of around 20 ppb and an  $H_2O$  level which balanced the outgassing rate from the warm cryostat surfaces.

The filling can thus proceed by transporting LAr through the filter system into the cryostat to ensure a high purity is maintained. The impurity concentrations were inspected before filling and after filtration and in total, a volume of 29.7 tons LAr was supplied to the LAPD cryostat. Once filled, and during the course of operations, the liquid argon volume was constantly recirculated through the filtration system to preserve the LAr purity. This is shown schematically in Figure 4.7.

#### 4.1.2.3 LAPD Outcomes

LAPD successfully demonstrated achieving and maintaining the required LAr purity for a large neutrino detector is possible without the costly and challenging use of evacuation techniques, reaching purities upwards of 60 ppt  $O_2$  equivalent. The measured electron lifetimes over the course of a six week run is shown in Figure 4.8. Lifetimes of up to 4 ms were recorded, greater than the DUNE requirement of 3 ms although utilising a much smaller-scale cryostat. Nonetheless, the success of LAPD has great significance for future LArTPCs, including the 35 ton, and was an important stage in the FNAL LAr test program.

#### 4.1.3 LongBo

Following the successful LAPD runs, a further phase involved the introduction of a small-scale TPC detector into the liquid argon [121]. The detector is named LongBo (an upgrade from the smaller Bo test detector) and is cylindrical with 25 cm diameter and 2 m length. It was positioned vertically in the LAPD cryostat, demonstrated in Figure 4.9, and was equipped with a high voltage on the cathode to produce the drift field and three wire planes at the top of the detector for readout. External scintillator counters were placed around the outer wall

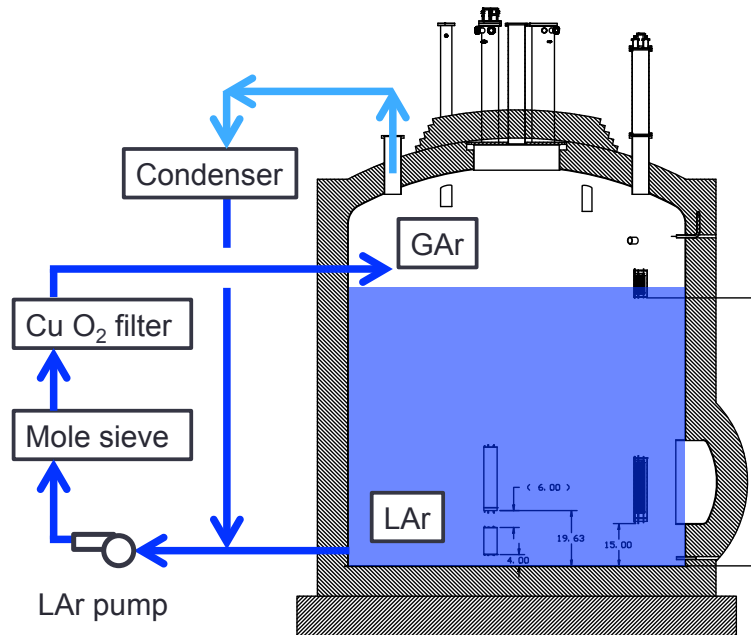


Fig. 4.7 Schematic showing the recirculation of the LAr during commissioning and operations of the Liquid Argon Purity Denomstrator [119]. Liquid is extracted from the bottom of the cryostat and pumped through the filters to remove any impurities which may have established in the medium. Following the experience of previous R&D with the MTS [112], the recondensed liquid is passed through the purification system before being reintroduced to the main volume inside the cryostat.

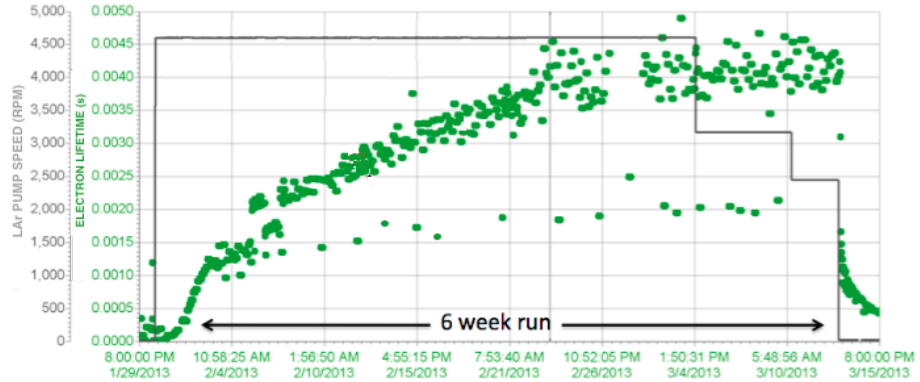


Fig. 4.8 The electron lifetime achieved in the Liquid Argon Purity Demonstrator during a six week run. Adapted from [119].

of the cryostat to provide triggers on through-going cosmic muons which may deposit charge in the detector.

LongBo was the first LArTPC experiment to utilise ‘cold readout’ electronics to amplify and shape the signal at the front end. An early version of the ASICs being developed for MicroBooNE were used to read out 16 of the 144 channels with the remaining using preamplifiers made with discrete circuitry. At the drift field of 350 V/cm, the signal/noise ratio, a useful number in quantifying the electronics, was around 30, with the channels read out by the ASICs reporting values up to 1.4 times larger.

The LAPD/LongBo experiment successfully maintained similar LAr purities than without the presence of the detector, as predicted by the results of the MTS. By using TPC data, it was also possible to make measurements of the electron lifetime from through-going muons (using Equation 7.1). A comparison between the measured values from the purity monitors and the TPC data may be found in Figure 4.10. A reasonable agreement is observed between these complimentary measurements with values between 6 ms and 14 ms reported, with 95% confidence. These promising results confirmed designing and operating a LArTPC within a non-evacuable cryostat is viable and contributed to the development of the LAr program towards the DUNE far detector, with the 35 ton experiment the next stage.

## 4.2 35 ton Experiment: Phase I

The scale of the cryostats required for the DUNE experiment are such that constructing them as flat plane vessels 1.5 km underground would be unfeasibly expensive and pose huge engineering challenges. Following the success of LAPD (discussed in Section 4.1.2), which eliminates the requisite to evacuate the cryostat prior to filling, the LBNE collaboration

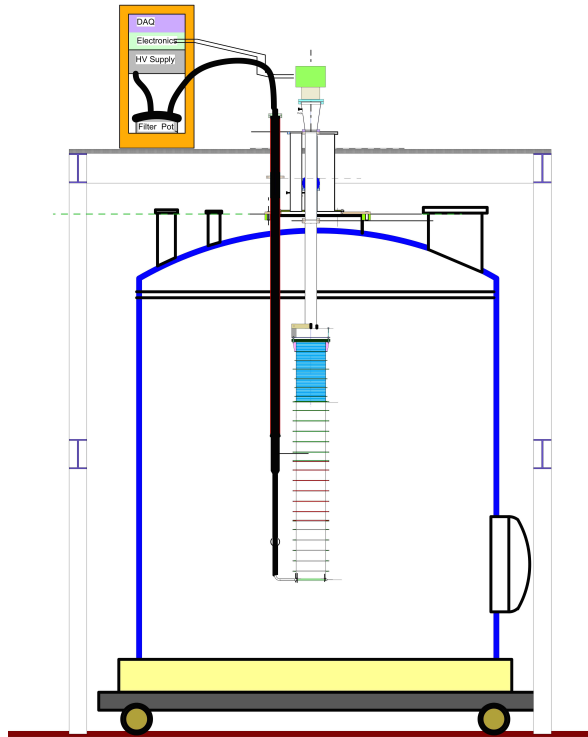


Fig. 4.9 The LongBo TPC detector shown within the Liquid Argon Purity Demonstrator Cryostat [121]. The black tube represents the high voltage feedthrough to the cathode at the bottom of the TPC.

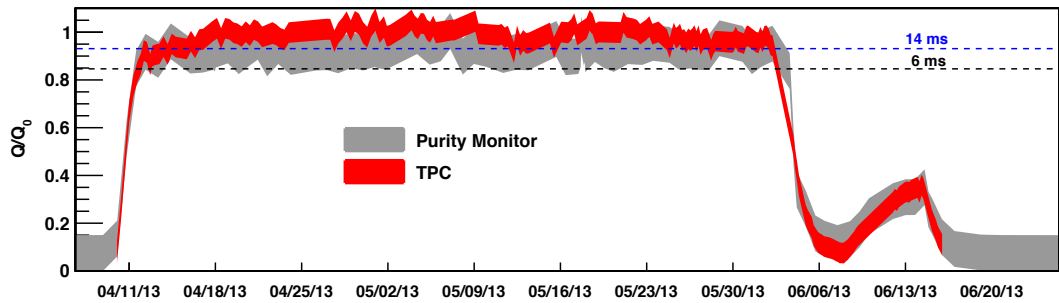


Fig. 4.10 The LAr purity within the Liquid Argon Purity Demonstrator cryostat with the LongBo TPC present, measured using both data from the detector and information from the purity monitors [121].

decided to utilise membrane cryostat technology well established in the liquified natural gas (LNG) industry. The 35 ton [122–124] was therefore employed to demonstrate the application of a membrane cryostat to a LAr experiment and was the only planned prototype for LBNE. The DUNE project has maintained this design choice and the 35 ton has since become a recognised and integral part of the collaboration, providing the first test of the technologies envisioned for the eventual far detector.

The 35 ton croystat was constructed in 2012 at PC4, a former proton facility in a decommissioned beamline, at Fermilab. It has operated in two phases: Phase I (December 2013 – February 2014) was proposed to demonstrate the membrane cryostat technology with just the cryostat and purification systems; Phase II (February 2016 – April 2016) contained a small-scale DUNE-style detector to validate the integrated system and affirm the detector design elements. The Phase I run is the subject of Section 4.2 whilst Phase II is considered in detail in Section 4.3.

The 35 ton is the first membrane cryostat used for scientific purposes and the first overall constructed in the United States. It is also the first designed to contain LAr, which is around three times denser than LNG. The initial aims of the project (Phase I) include to demonstrate the feasibility of the cryostat technology for LAr, including thermal performance and leak tightness, and to show the required LAr purity may be achieved without evacuation and maintained through the use of the filtration system developed and validated by the MTS and LAPD. This first phase will be discussed in this section; the 35 ton cryostat and filling procedures will be described in Sections 4.2.1 and 4.2.2 respectively before outcomes of the experiment are presented in Section 4.2.3.

### 4.2.1 The 35 ton Cryostat

An overview of the 35 ton cryostat is shown in Figure 4.11. It contains a concrete shell within which the membrane cryostat is constructed from 2 mm think stainless steel panels. An insulated region between these two segments reduces heat leaking. The roof consists of two plates; Plate A is flat with insulation and membrane beneath and Plate B contains all penetrations and services. Relevant properties of the 35 ton cryostat are listed in Table 4.1.

The 35 ton was constructed physically nearby the Liquid Argon Purity Demonstrator in order to utilise existing infrastructure. It is connected to the LAPD tank, which may be used to store LAr before transferring to the 35 ton, and uses the filtration setup designed and validated by the MTS and LAPD. This network is shown schematically in Figure 4.12. Unlike in LAPD, the pumps used in the 35 ton to circulate the LAr through the purification system are within the liquid but the framework operates in a similar way. An identical condenser is also employed above the cryostat to cool boiled off gaseous argon which is

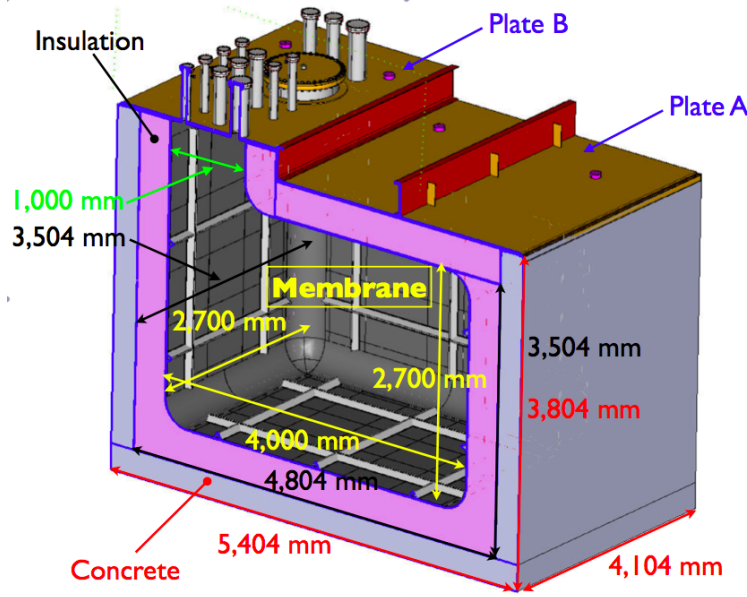


Fig. 4.11 The 35 ton cryostat [124].

Table 4.1 Details and dimensions of the 35 ton cryostat [124].

Parameter	Value
Cryostat volume	29.16 m <sup>3</sup>
LAr total mass	38.6 metric tons
Depth of LAr	2.565 m (11% total ullage)
Inner dimensions	4.0 m (length) × 2.7 m (width) × 2.7 m (height)
Insulation	0.4 m polyurethane foam
Primary membrane	2.0 mm thick corrugated stainless steel
Secondary barrier system	0.1 mm thick fiberglass
Vapor barrier	1.2 mm thick carbon steel
Steel reinforced concrete	0.3 m thick layer
LAr temperature	89 ± 1 K
Operating gas pressure	70 mBar
Design pressure	207 mBar
Heat leak	< 13 W/m <sup>2</sup>
Leak tightness	$1 \times 10^{-6}$ mBar·litre/s

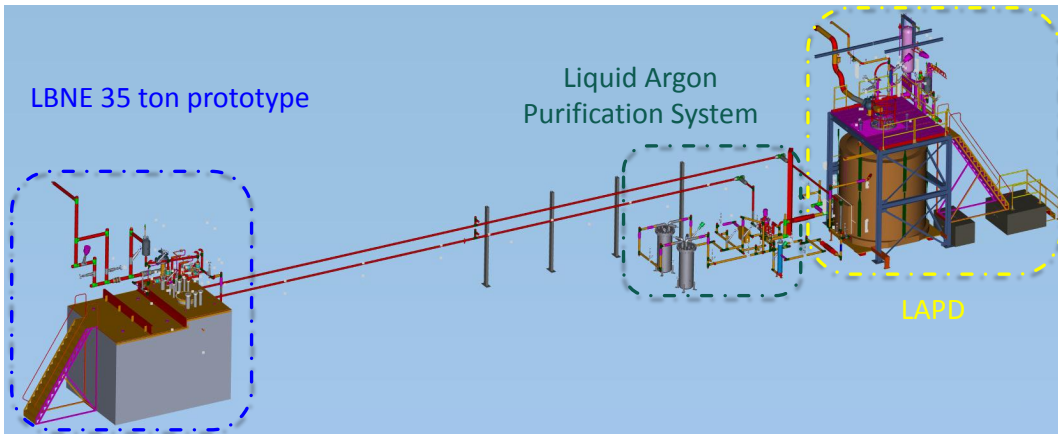


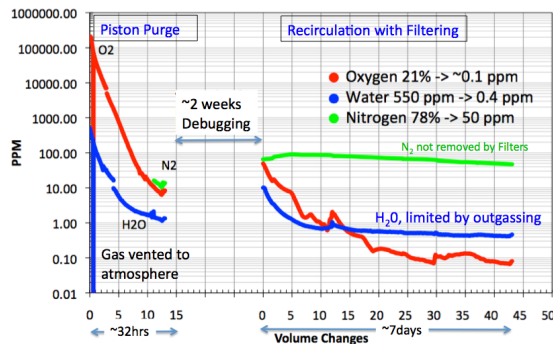
Fig. 4.12 The network linking the 35 ton cryostat, the Liquid Argon Purity Demonstrator and the purification system at PC4, Fermilab [123].

returned to the bottom of the cryostat, nearby the pumps which subsequently extract the liquid for purification.

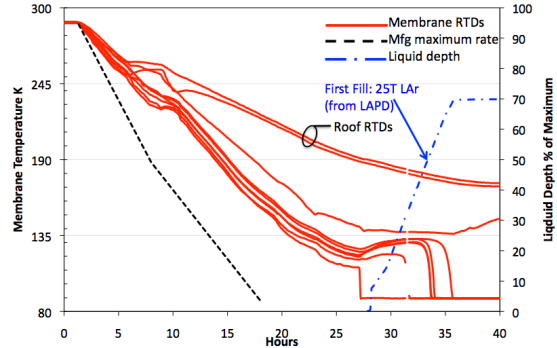
The cryogenic environment is monitored and controlled using standard detectors including temperature sensors, pressure transducers, flow meters and level sensors along with a suite of commercial gas analysers. The height of the volume is instrumented with four purity monitors, two large and two small, with an additional long monitor positioned after the filters, as with LAPD. Also as previously, the vertical temperature profile in the cryostat is monitored at 23 cm intervals with temperature detectors suspended on a chain.

### 4.2.2 Filling the 35 ton

The 35 ton cryostat is filled in a similar way to the Liquid Argon Purity Demonstrator, described in Section 4.1.2.2. Initially, a piston purge with warm gaseous argon is performed to remove atmospheric impurities before closing off the vents and redirecting argon at the top of the cryostat through the filters for purification. The impurity concentrations for this stage of filling are shown in Figure 4.13a. Before filling with liquid, the cryostat is cooled in an attempt to reduce outgassing and to create an appropriate environment in which to introduce LAr. This is achieved by injecting LAr through a spray at the top of the cryostat which generates a turbulent mixing of cold gas within the cryostat and gradually cools the walls of the vessel. Following this, LAr is transferred from LAPD into the 35 ton; this is conducted in two stages since the 35 ton is slightly larger than LAPD. The cooldown and LAr filling stages are shown in Figure 4.13b.



(a) Gas filling.



(b) Liquid filling.

Fig. 4.13 Filling the 35 ton cryostat in four stages: piston purge, gas recirculation, cooldown, liquid filling [124]. The gas filling is shown in Figure 4.13a and involves using a piston purge to fill the tank with warm gaseous argon before circulating this gas through the filtration system. Cooldown and liquid filling is demonstrated in Figure 4.13b, which shows the falling temperature of the cryostat as a result of the injection of liquid argon through the cooldown sprayers and the rising LAr level as the cryostat is filled from LAPD.

### 4.2.3 Outcomes of Phase I

The 35 ton successfully demonstrated the feasibility of membrane cryostats for use with LAr and additionally showed the required LAr purity for future multi-kton LArTPC experiments may be achieved and held in such a vessel. The lifetime over the course of the  $\sim 2$  month run, along with external changes to the system, is comprehensively summarised in Figure 4.14.

The lifetime is observed to reach and remain at the DUNE requirement for a good period of time; this is a major achievement in the context of the future of LArTPC experiments. Dips in the purity were observed when topping up the cryostat after initially filling one LAPD volume and when switching between the two pumps installed to extract the liquid for purification. In both cases, good purity is recovered after a few volume exchanges.

The same variations of lifetime on temperature were observed as previously noted in the MTS and LAPD, suggesting a genuine effect dependent on the ambient conditions. Additionally, during gas circulation a leak was found and fixed in a seal and, during cold operations, a leak developed in the argon cryo-piping as the dielectric breaks necessary to electrically isolate the cryostat from the building were not leak tight at cryogenic temperatures. All associated 35 ton experience is useful as progress continues to larger and more complicated LAr cryostats.

The success of the 35 ton was exploited by utilising the existing setup for a second run, involving a small-scale DUNE-style detector. This would be the first time a membrane

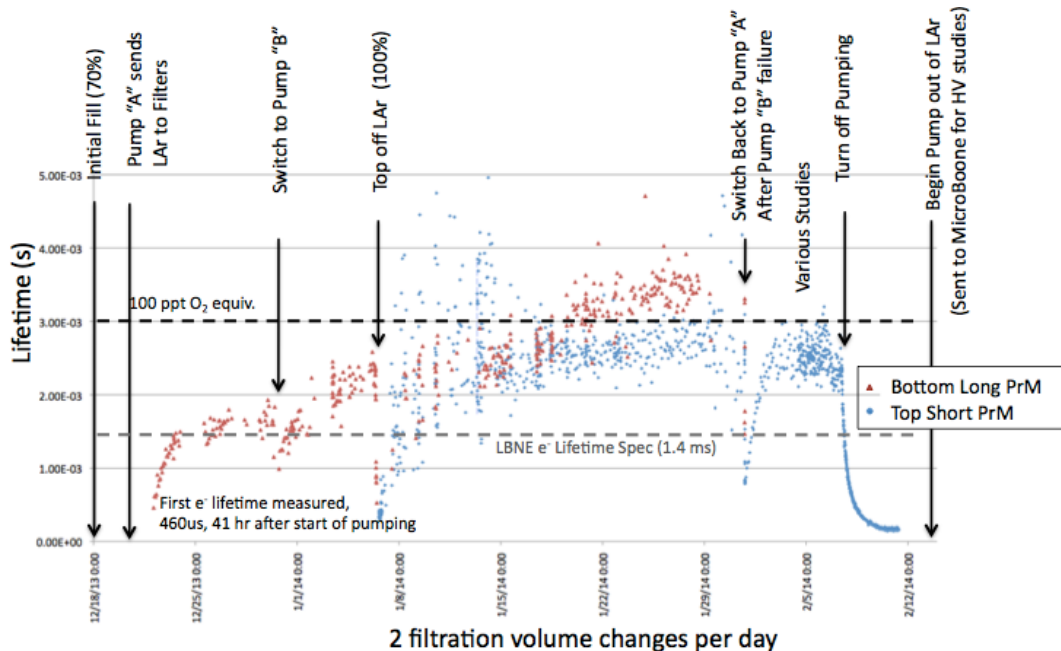


Fig. 4.14 The electron lifetime in the 35 ton cryostat measured by two purity monitors over the course of the two month Phase I run [123]. The measurements correspond to different positions in the cryostat, with the red points showing purity measurements at the bottom and blue points near the top. Major external factors affecting the observed LAr purity are shown at the top of the figure. The old LBNE requirement of 1.4 ms is noted as a dashed grey line; DUNE now requires 3 ms lifetime, equivalent to 100 ppt O<sub>2</sub> and illustrated by the black dashed line.

cryostat would facilitate a detector and is the next stage along in prototyping the DUNE far detector.

## 4.3 35 ton Experiment: Phase II

The first (and to date, only) particle detector housed within a membrane cryostat was the 35 ton Phase II. Following the positive outcomes of the 35 ton Phase I (discussed in Section 4.2), it is natural to extend operations to include a prototype DUNE detector. The initial aims of the 35 ton Phase II experiment were to develop, build and install a working TPC within the existing cryostat and infrastructure and make measurements of particle interactions induced by cosmic muons whilst demonstrating the required LAr purity is still maintained within a integrated system.

The operation of the second 35 ton phase will be discussed in detail in this section. An overview of the detector is provided in Section 4.3.1 before the data acquisition from the detector elements is discussed in Section 4.3.2. The custom camera system developed at Sheffield for detecting dielectric breakdown of the LAr is the subject of Section 4.3.3. Finally, the period of data taking is outlined in Section 4.3.4 before outcomes of the project are presented in Section 4.3.5.

### 4.3.1 The 35 ton Detector

A cutaway view of the 35 ton cryostat showing the detector installed in shown in Figure 4.15. The detector elements are designed to prototype as many features of the DUNE far detector as possible (shown in Figure 3.10). The readout is performed four APAs with wrapped induction wires and cold front end electronics (amplifiers and digitisers) which read out multiple drift regions simultaneously. Embedded within the APAs are photon detectors, representing three difference design choices, to trigger on scintillation light. The drift field is enabled by cathodes at either end of the TPC. A flange placed on Plate A facilitates a warm/cold interface through which all electrical signals and the high voltage (HV) feedthrough pass. Surrounding the walls of the cryostat are over 100 scintillation paddles (Cosmic Ray Counters, CRCs) to provide additional triggers from through-going cosmic muons.

The three main detector components, the TPC, photon detectors and external counters, are discussed in the following sections. A photograph of the partially installed detector is shown in Figure 4.16 highlighting most of the detector during construction.

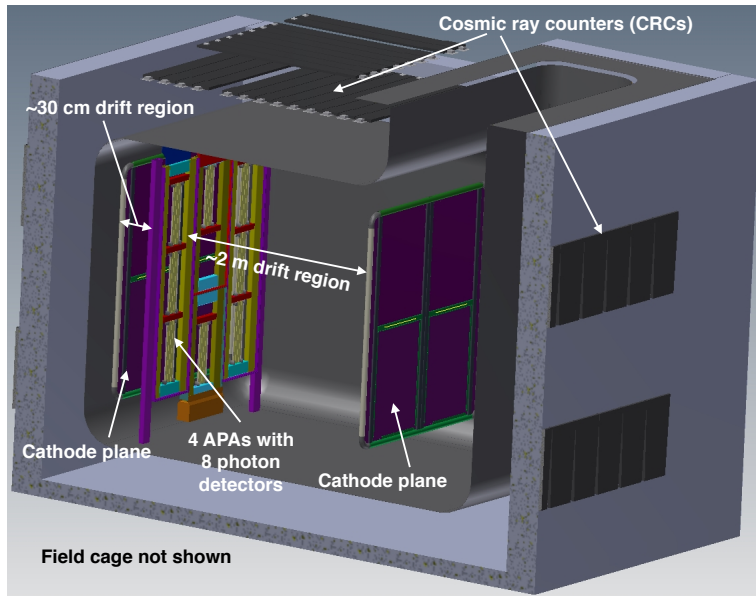


Fig. 4.15 The 35 ton detector operated during Phase II of the 35 ton program [107].

### 4.3.1.1 TPC

The 35 ton TPC is very similar to the DUNE single phase design introduced in Section 3.3.2.1. It has a module form, with multiple APAs reading out separate drift volumes, and two drift regions: the ‘long drift region’ of length 2.26 m and the ‘short drift region’, around 0.30 m long. Four APAs are used with a very similar design to that demonstrated in Figure 3.11; each contains two wrapped induction views with a grid and collection plane on each face. The main difference between the APAs tested in the 35 ton and the current DUNE far detector design is the physical dimensions of the frames and the angle the induction wires make to the vertical. There are three sizes of 35 ton APA; two tall (204 (height)  $\times$  52 (width) cm) either side of two shorter structures stacked vertically (upper APA dimensions 112 (height)  $\times$  52 (width) cm and lower APA dimensions 92 (height)  $\times$  52 (width) cm). The induction wires are wrapped at an angle of around 45°, as opposed to 37°, with slight differences between the planes to ensure the degeneracy is broken (angles of 45.7° and 44.3° are used). It was after experiences with the 35 ton that the angles in the current design were chosen, to facilitate a more straightforward disambiguation.

With four APAs and two separate drift regions, there are eight independent drift volumes (DVs), often also referred to as TPCs. These are demonstrated as part of the geometry in Figure 4.17. The coordinate system is defined in this figure; the drift direction is described by the  $x$ -coordinate and the dimension across an APA face, along which the collection planes are spaced, uses the  $z$ -coordinate (explaining the denotation of this plane as the Z plane). The



Fig. 4.16 Photograph of the partially installed 35 ton detector [125]. The four APAs, with the embedded photon detectors, are visible and the field cage is under construction. Cameras and cold cabling from the Sheffield Camera System, the subject of Section 4.3.3, may be observed in a box, prior to installation, at the bottom of the photo.

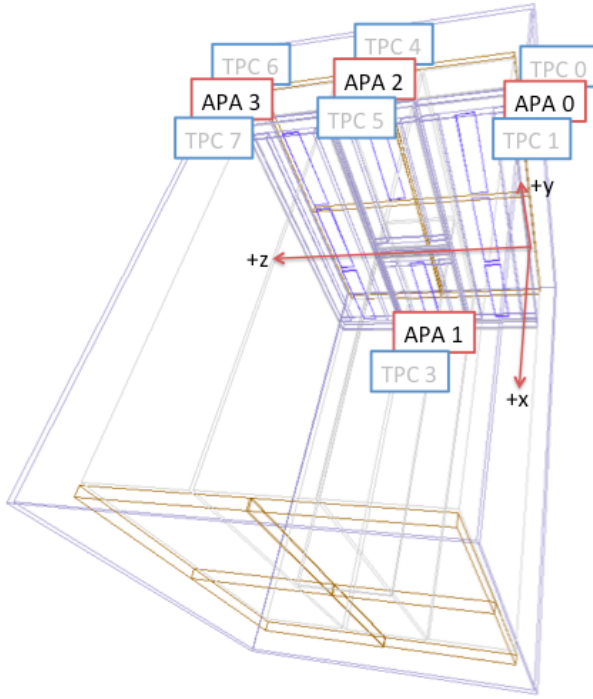


Fig. 4.17 The 35 ton TPC geometry and coordinate system [126]. The blue frames represent the APAs and the orange the CPAs. The eight separate drift volumes resulting from the modular TPC form are labelled TPC0–7.

$y$ -coodinate is parallel to the orientation of the vertical wires. The origin is at the edge of one of the long APAs and is such that  $x = 0$  is at the centre of the APA frames with positive  $x$  pointing into the long drift region,  $y = 0$  is half way between the two short centre APAs and  $z = 0$  is at the right hand side of the APAs when looking from the long drift region with positive  $z$  directed across the faces of the APAs.

The cathode and HV feedthroughs are designed to facilitate a voltage of 120 kV, providing the nominal field of 500 V/cm. A field cage constructed using FR4 printed circuit board surrounds the open sides of the TPC to set up the necessary electric field. This was the old LBNE design and has since evolved in the current DUNE outlook; it still enabled a study of the required field within a LArTPC however.

The TPC readout is similar to the DUNE design, with cold preamplifiers, signal shaping and digitisation implemented in ASICs mounted on front end boards at the ends of the APAs. This is the first time a fully cold signal readout has been implemented in a LArTPC experiment and will be discussed in more detail in Section 4.3.2.1.

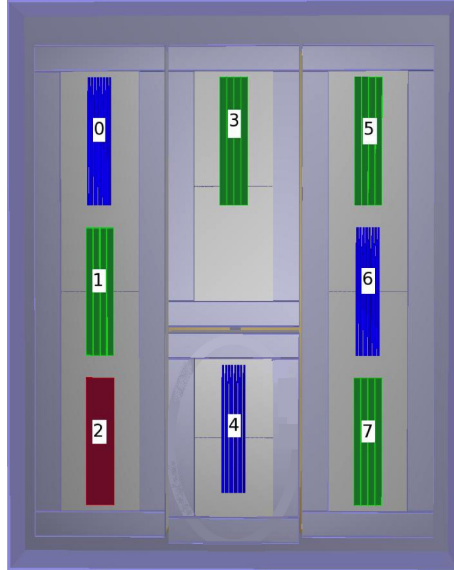


Fig. 4.18 Photon detector units as implemented within the 35 ton APAs [127]. The green detectors are the most similar to the current DUNE design and consist of a plastic bar with wavelength shifter (WLS); the blue and red detectors utilise designs of bundled fibres and plates embedded with WLS fibres respectively.

#### 4.3.1.2 Photon Detectors

Three design of photon detector were utilised in the 35 ton, none of which are current far detector considerations. There were implemented within APAs in between the wire planes as eight separate units, demonstrated in Figure 4.18 [127].

All detectors were read out by SiPMs and processed using custom built ‘SiPM Signal Processors’ (SSPs), discussed further in Section 4.3.2.1. It was following experiences from the 35 ton that the current DUNE far detector design evolved (shown in Figure 3.12). In this plan, the detectors are orthogonal to the 35 ton versions and are inserted after the wire wrapping.

#### 4.3.1.3 External Counters

In order to provide an additional external trigger system, the 35 ton detector is instrumented with muon counters. Most are located on the outer walls of the cryostat, around all four sides and on top of Plate B on the roof. There are additional counters in the ceiling of the building directly above the 35 ton cryostat. The positioning all all scintillator paddles is shown in Figure 4.19. There are two separate triggers provided by the counters: the ‘telescope trigger’ caused by coincident hits recorded by the counters in the ceiling and those on the cryostat roof and the ‘horizontal trigger’ caused by coincident counter hits on opposite walls of the

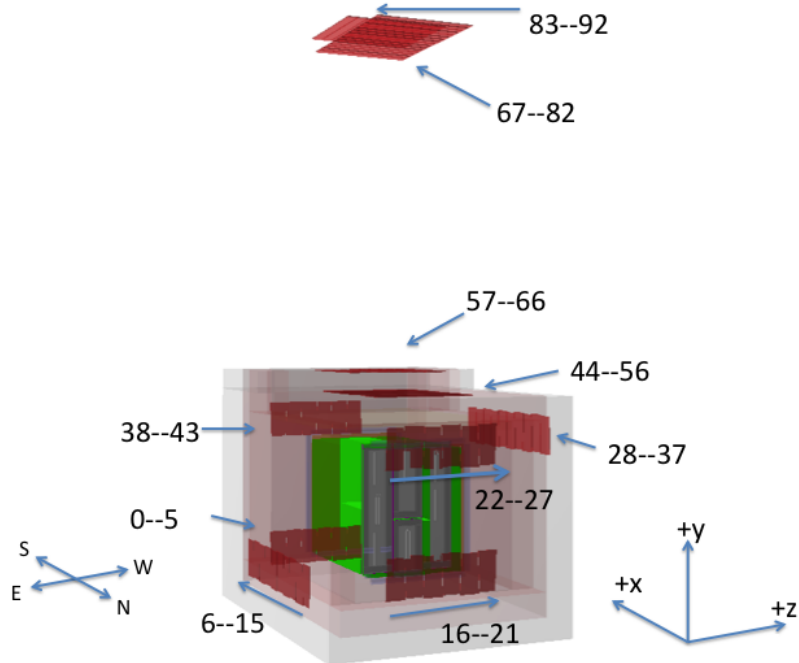


Fig. 4.19 The location of the external counters positioned around the outer walls and in the ceiling above the 35 ton cryostat [128].

cryostat (further subcategorised into ‘EW’ and ‘NS’ triggers). The trigger rate for telescope muons is on the order of 60 Hz whilst horizontal muons trigger at a rate of around 2-3 Hz.

### 4.3.2 Data Acquisition

#### 4.3.2.1 RCEs, SSPs, PTB

During the testing of components in the warm during summer 2015, issues were identified with the TPC electronics

#### 4.3.2.2 35 ton DAQ

### 4.3.3 The Sheffield Camera System

There are many motivations for developing a camera system which operates at cryogenic temperatures as interest in experiments utilising LAr and LXe (as many dark matter experiments, such as Lux-Zeplin [129], are considering) progresses. These include visual monitoring of the cryostat after sealing, including observing the cooldown and filling with cryogenic liquids, and to monitor HV discharge problems. This latter issue has become cause for concern as LArTPC experiments with very large voltages are being developed; for example, DUNE

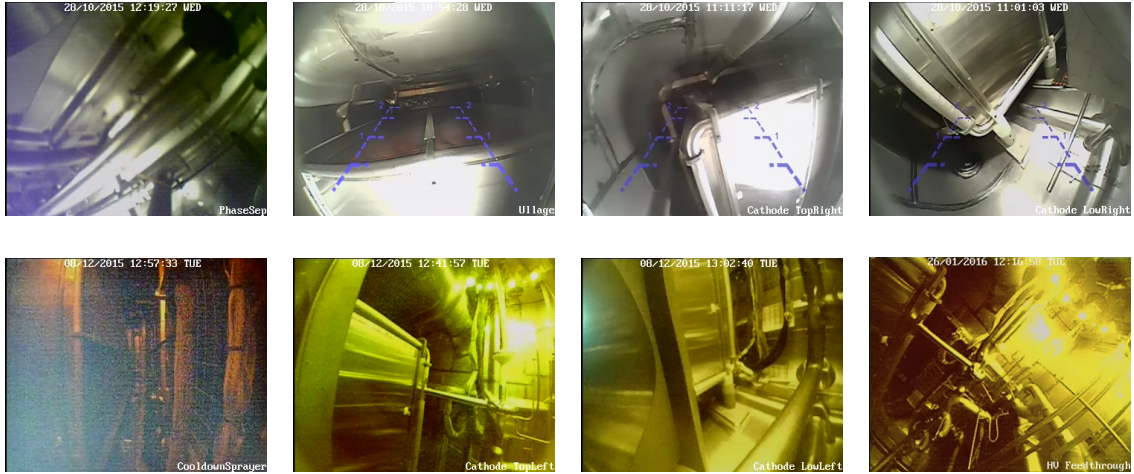


Fig. 4.20 The calibration images for the 8 cameras in the system. Upper (left to right): phase separator, ullage, cathode top right, cathode bottom right. Lower (left to right) cooldown sprayers, cathode top left, cathode bottom left and high voltage feedthrough. The upper images were taken with a halogen light illuminating the cryostat, prior to it being sealed up. The lower images were taken with the LED ring light on, with the cryostat sealed up. All images are left-right inverted due to software. Taken from [131].

will require a cathode HV of  $-190$  kV. Understanding the dielectric properties of LAr is therefore of paramount importance, with recent research suggesting breakdowns occurring at only  $40$  kV/cm [130]. An additional aim of the 35 ton Phase II experiment was to study the effects of HV and to search for evidence of HV breakdown of the LAr which may be used to influence the design of future LArTPC experiments in order to mitigate against these effects. This is the primary motivation of the camera system deployed in the 35 ton cryostat [131], designed at the University of Sheffield and described in this section.

The 35 ton was instrumented with eight cameras; six to monitor high-field locations within the cryostat and for detecting visual sparks from HV breakdowns, and two for diagnosis of different cryogenic systems including the cooldown sprayer and the phase separator. The fields of view of each of the cameras are demonstrated in the calibration images shown in Figure 4.20.

#### 4.3.3.1 The Camera System

Previous cameras designed to study cryogenic liquids have either been placed outside the volume or been maintained in a heated vessel for protection from the cold surroundings. A system which operates directly in cryogenic temperatures is desirable when applying the technology to larger-scale cryostats and for possible use in the detection of secondary scintillation light. Achieving this without an actively heated region in the cryostat is also

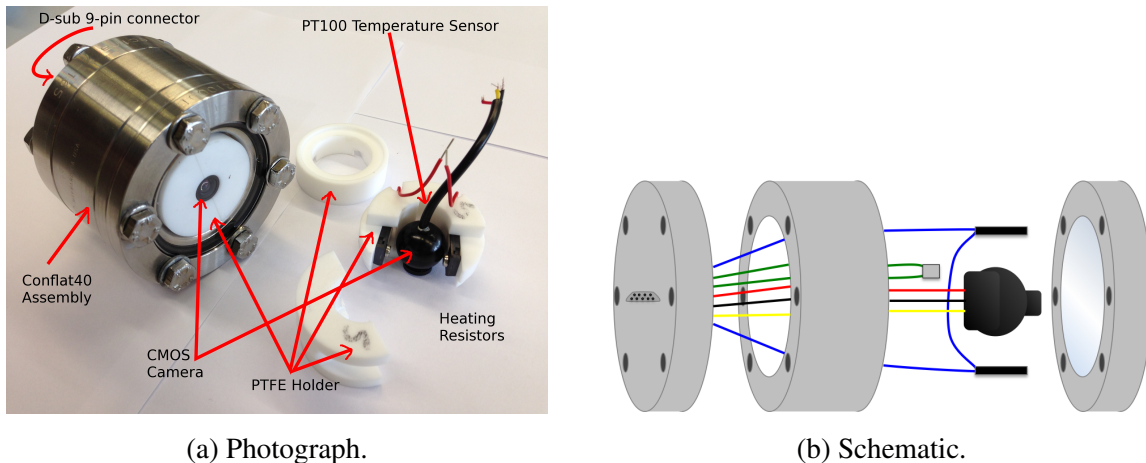


Fig. 4.21 An example camera module developed for the 35 ton Sheffield camera system, taken from [131]. Figure 4.21a shows a sealed camera module and the components of such a module. Figure 4.21b demonstrates schematically the composition of a camera module: from left to right a CF40 flange with 9-pin D-sub feedthrough, double sided CF40 flange, PT100 sensor (green wires), camera (red, black and yellow wires), two heating resistors (blue wires) on either side of the camera connected in series, optical viewport on CF40 flange.

advantageous to avoid boiling and disturbing the LAr in close proximity. The camera system developed utilised Complementary Metal-Oxide Semiconductor (CMOS) cameras contained within a module alongside a temperature sensor and small resistive heater. This is demonstrated in Figure 4.21.

The cameras are commercially sold as car-reversing cameras and are rated by the manufacturer down to  $-40^{\circ}\text{C}$  (233 K). A wide range of cameras were tested and those which consistently performed well in tests whilst at cryogenic temperatures (submerged in liquid nitrogen) were selected. Around half of these were found to reliably endure power cycling when cold (the inconsistency arising from operating the cameras outside of the recommendations) and it was these which were included in the modules used in the 35 ton. The heating elements were included as a failsafe mechanism in case the cameras developed a requirement of warmer local temperatures to turn on after sustained periods in the cold.

Each camera contains  $712 \times 486$  pixels and has a roller shutter rate of 50 frames per second. Their resolution at 10 mm was found to be  $(2.0 \pm 0.5)$  mm at room temperature and  $(1.5 \pm 0.5)$  mm at 77 K, with the improvement at lower temperatures due to a higher refractive index of LN<sub>2</sub> resulting in the light becoming less diffuse. The minimum measurable light pulse, in both the warm and the cold, was observed to be 20 ns. One notable change when operating the cameras at cryogenic temperatures was the chrominance output of the video



Fig. 4.22 Two camera modules mounted on cryo piping in the 35 ton cryostat. Taken from [131].

signal. The usual colour signal is observed as monochromatic when in the cold, possibly due to partial failures on the on-board encoding electronics.

Before installation, the response of the cameras to sparks was characterised by applying a HV across a printed circuit board (PCB) in LAr until breakdown was observed. The discharge was between 40 and 60 ms and the cameras showed localised sparks persisting over multiple frames of exposure. The trigger system, which relies on a percentage change in the number of different pixels between successive frames, was also able to successfully detect and automatically record on occurrence of the sparks.

#### 4.3.3.2 Operation and Outcomes of 35 ton Camera System

The camera modules were mounted on the existing piping from the cryogenic system within the 35 ton. An example is shown in the photograph in Figure 4.22. Data acquisition, operation and control was performed using a rack-based system containing a power supply, a temperature sensor reader, DAQ and computer control system. Full details of the entire arrangement and all the interconnects are available in Figure 4.23.

The cameras were characterised in room temperature following installation and the software trigger tested on the Xe flash light from the purity monitors (described in Section 4.1.1.2). The system ran continuously throughout the 10 weeks of the 35 ton Phase II cooldown. It was heavily utilised during cooldown and filling to monitor the inside of the

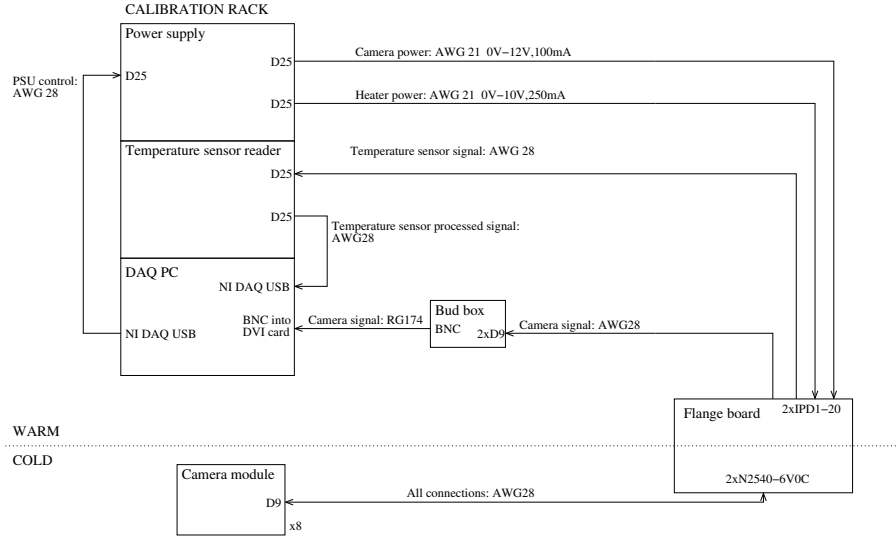


Fig. 4.23 Full system block diagram for the camera modules in the DUNE 35 ton prototype. Taken from [131].

cryostat and observe the rising liquid level (an excellent video of the LAr when level with one camera module is available at Reference [132]). The entire system was power cycled successfully three times during TPC debugging and following the FNAL site wide power outage on 4rd March 2016. The downtime ranged from 30 minutes to 9 days, with the cameras turned on without assistance each time.

The picture quality was observed to degrade noticeably over time, demonstrated in Figure 4.24, with significant variation between different camera modules. When in darkness, a greater number of saturated or noisy pixels is observed across the cameras and when illuminated by the LED ring, the noise increase is noticeable with a decreased colour depth. This is likely due to signal transmission length, power cycling and increased prologue in the cold.

Two suspected HV breakdowns occurred during normal operations at 60 kV but the system was unoperational as a result of the power outage during both. Following the end of running, when testing the HV at 135 kV, four breakdowns occurred with three detected and triggered on by the camera system. However, the location of the spark could not be determined clearly from the recorded video. This could be due to either the spark occurring outside the cryostat or the field of view of the cameras, an insufficient intensity or duration of the flash or the degradation in picture quality being such that the efficiency and sensitivity of the triggering system were compromised.

The camera system was shown to be successful and a hugely useful aid in 35 ton operations. Despite not showing HV breakdowns clearly, the modules remained operational

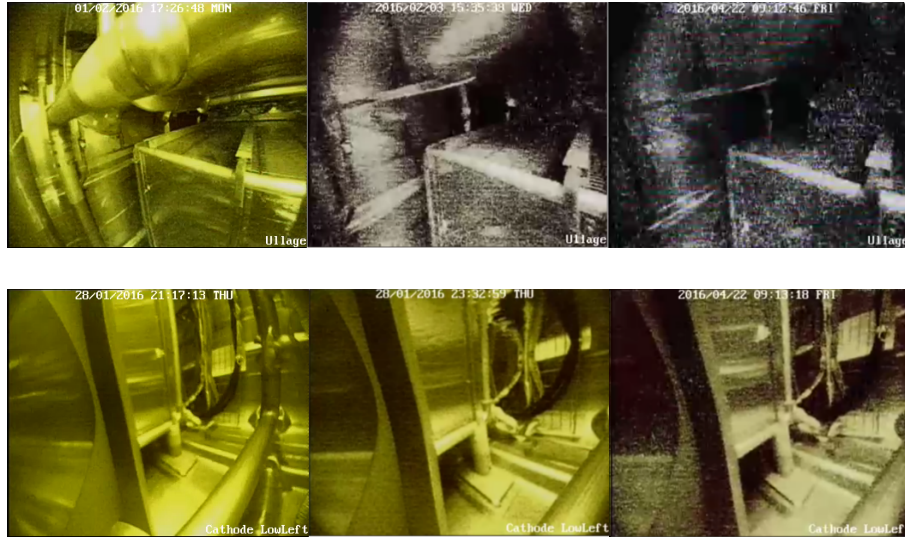


Fig. 4.24 The variation in picture quality degradation is illustrated by the changes in Camera 1 (upper) and Camera 4 (lower) over time. Left: prior to cooldown, centre: immediately post-cooldown, right: after 10 weeks submerged in LAr. The field of view changes due to the change in refractive index. Note that these are full colour images with no post-processing. Taken from [131].

during the 35 ton Phase II run and were valuable for monitoring purposes. They were shown to trigger successfully on a test bench so it seems reasonable to conclude their inability to do so within the LArTPC was solely due to the degradation in picture quality, which must be improved if such a system were to be used in future LAr experiments.

#### 4.3.4 Phase II Run

Following a long period of testing the detector components at FNAL, installation of the TPC and field cage was carried out in October 2015. This was followed by the final parts of the system, such as the long drift region cathode, the purity monitors, HV feedthrough and cameras, in November 2015. Following the Fermilab readiness clearance, operations began in December 2015. This involved piston purging both LAPD and the 35 ton, filling LAPD with LAr delivered from the suppliers, cooling down the 35 ton cryostat and finally transferring the liquid argon from LAPD into the 35 ton. This was completed by the end of January 2016.

**NOTE:** I've not added any plots at all from the cooling/filling/piston purge/purity etc etc from the filling stage; it's basically the same as Run I. I can do if we think it'll be useful though (they are a bit nicer than the Run I ones!)

The 35 ton Phase II run officially started on 11th February 2016 upon the final liquid transfer into the cryostat and the starting of the pumps and recirculation of the LAr through the filtration system. A week later, the HV on the cathode was ramped up to half nominal value: 60 kV, providing a drift field of 250 V/cm. The intention was to ensure a sufficient amount of collected data was on disk before proceeding with increasing the HV up to the design voltage of 120 kV (500 V/cm) and even up to the maximum of 135 V/cm.

The start of the run was dedicated to many noise tests; it was immediately clear the noise on the TPC channels was much larger than anticipated even after the testing from the previous summer. These tests involved studying each of the FEMBs separately and considering effects from other non-TPC detector elements by removing power from all systems in the cryostat before reintroducing components iteratively. An additional ‘high noise state’ was also identified which corresponded to a very high oscillatory noise level instantaneously appearing on all channel simultaneously and remaining for up to hours at a time. The noise problems in the 35 ton Phase II will be discussed in more detail in Section 4.3.5.

This time was also important as the stability of the DAQ was improved. Near the beginning of data taking, it was uncommon for the DAQ to run for more than a few minutes with even a small subsection of components (RCEs, SSPs, PTB), with issues such as data throughput, disk writing speed and hardware interface issues contributing to a very unstable system. In the months of installation and commissioning, the DAQ was the subject of much attention and progress on improving the framework progressed in parallel with the final installation, LAr filling and noise hunting.

Following the completion of the designated noise runs and the stabilising of the DAQ, the focus was on collecting as much data as possible before raising the HV, with the plan to run for at least week at 90 kV and 120 kV respectively. However, the run was unfortunately cut short in the early hours of the morning of 19th March 2016 when a tube, part of the system which was introducing GAr from LAPD to the 35 ton purification network in order to maintain the LAr level, sheared and facilitated the introduction of air directly into the filters. Within a few minutes, faster than it would have been possible to respond even if this incident had not occurred at 3 a.m., the filters were saturated and the entire volume of LAr in the 35 ton was poisoned. The offending pipe break is shown in Figure 4.25. This incident effectively concluded the data collection prematurely and meant the design HV could not be tested in good quality LAr and no data could be taken at nominal drift field.

The run is summarised in Figure 4.26, showing the LAr purity as a function of time and notable incidents. The bulk of collected data was either side of a site-wide FNAL power outage on 4th March 2016, after which it took a few days to recover the LAr purity. After recuperating from this incident, an issue with the LN<sub>2</sub> values resulted in a cooling failure and



Fig. 4.25 The broken pipe, originally part of the framework introducing gaseous argon from LAPD into the 35 ton to maintain LAr levels, which resulted in the poisoning of the whole LAr volume by allowing the introduction of air into the system.

the boiling off of a large portion of the LAr in the cryostat. The pipe break occurred shortly after rectifying this issue. The high frequency of these complications within such a short space of time motivated the description of this period of running as the ‘Bad News Period’ on the figure.

Most of the data taken were triggered using the horizontal muon trigger. In the last week of running, the telescope trigger was deployed, with a large prescaling due to the high rate of cosmic muons, and the photon detectors were also used to trigger data taking. Both systems appeared to work as intended but thorough testing proved impossible due to the temporal proximity to the unforeseen termination of run. Throughout data taking, the DAQ recorded data to disk at a rate of 1 Hz. Also due to the premature run end, tests of data taking using zero suppression were unable to be performed.

Overall, the run provided 22 days of high quality (good LAr purity, high stable voltage, stable DAQ) data, albeit with much higher noise than anticipated. An example electromagnetic shower observed in the data with strong signals in all planes is depicted in Figure 4.27. The noise problems have resulted in limitations to the analyses possible with the 35 ton data and focus has shifted to studies utilising datasets unique to the 35 ton. Some such analyses are the subject of Chapter 7.

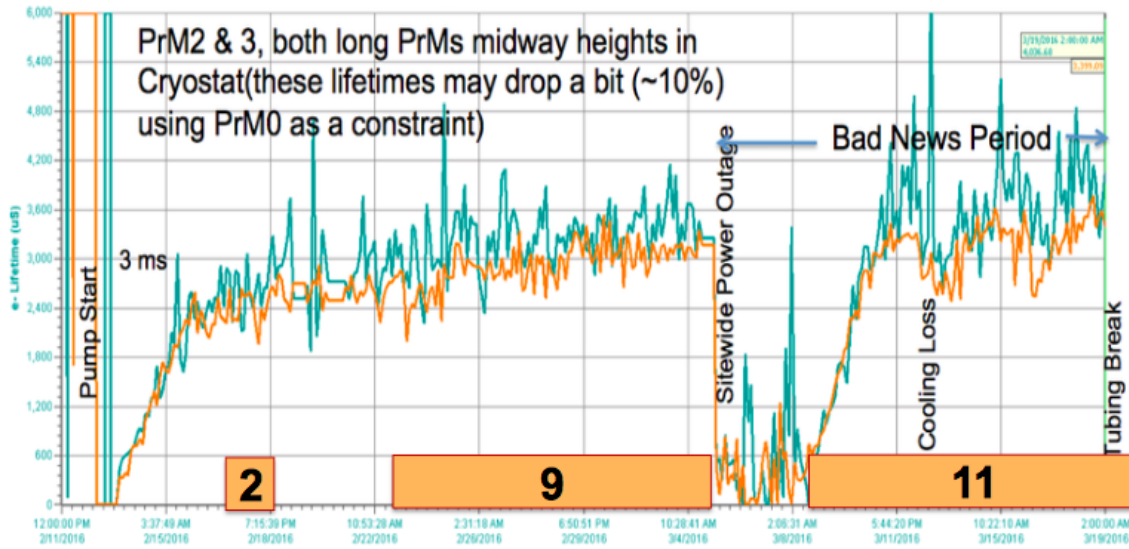


Fig. 4.26 The data taking period of the 35 ton Phase II experiment. The electron lifetime measured by the two long PrMs in the cryostat is shown as a function of time, with the horizontal axis covering the period 11th February – 19th March 2016. The numbers within the orange boxes represent the amount of data taken with the drift field of 250 V/cm present, in days. The major incidents which affected the LAr purity are shown on the figure.

### 4.3.5 Outcomes of Phase II

The 35 ton Phase II collaboration successfully design, constructed, installed and ran a small-scale DUNE-style LArTPC and collected data whilst maintaining a good LAr purity, with electron lifetimes consistently reported above the DUNE requirement of 3 ms. This is the first time a detector has been operated within a membrane cryostat and the integrated system has been strongly validated. The complete process has been instructive and a great many lessons have been learned alongside the successes of the project.

This section will review all these outcomes and discuss how the experience will influence the DUNE program as it progresses towards the first far detector module. In general, the experiment was a success with the majority of subsystems achieving or superceeding expectations. Following the 35 ton Phase II experience, there is no reason for reservation over ProtoDUNE as rapid development continues to be made.

#### 4.3.5.1 Cryostat and TPC

The cryostat and most TPC components behaved as expected and resulted in no unexpected functionality. When filled with GAr, before the introduction of LAr, the cryostat was leak tested. When this was performed in Phase I a few issues were identified and had to be addressed; there were no complications during Phase II commissioning however. The pumps

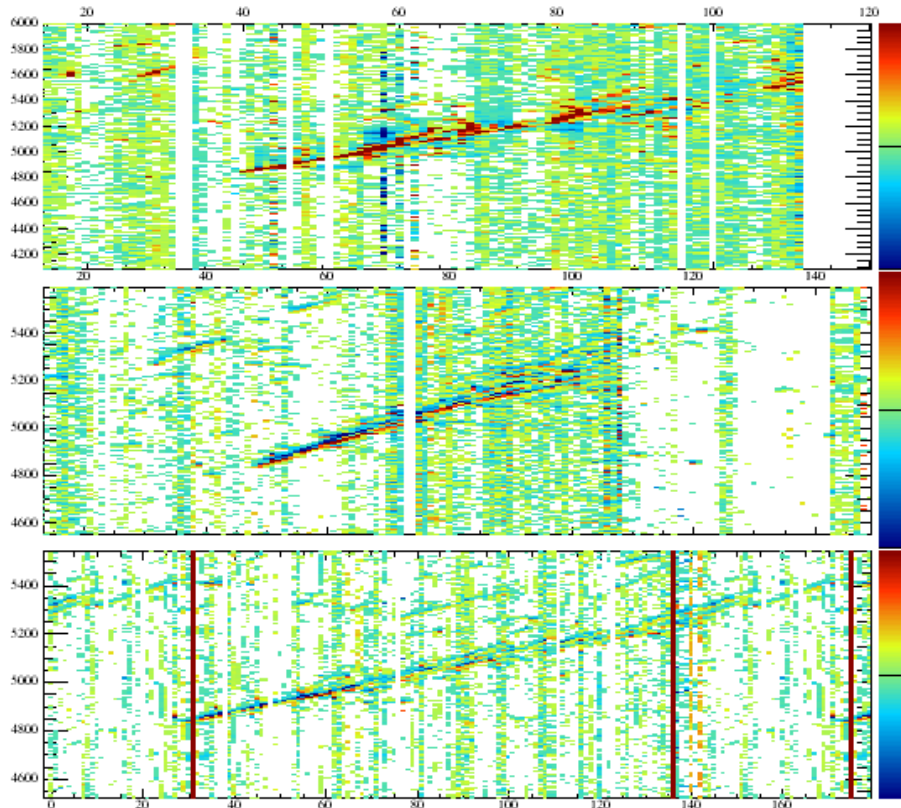


Fig. 4.27 Event display depicting the charge deposited by an electromagnetic shower during the 35 ton Phase II run. The three views are, from the top down, the collection plane and the V and U induction planes. Each shows the wire number on the horizontal axis and time, measured in units of ‘tick’ (1 tick  $\equiv$  500 ns) on the vertical axis. Charge is represented by the colour scale on the z-axis. The shower is clearly visible in all three planes and demonstrates the functionality of the 35 ton detector.

were not tested between phases and required a huge current to break them in with the cryostat already filled with LAr; this demonstrates how vital it is to assess all detector components before commissioning. Other than the failing in the cooling system, all cryogenics performed excellently. Since this incident occurred not long after the power outage, the alarm system had not been correctly brought back online, resulting in an avoidably large loss of LAr. These are two of many examples of lessons learned from the 35 ton.

The HV and drift field presented no issues during the course of the run. No confirmed breakdowns were observed at 60 kV but testing in clean LAr at 120 kV was not possible. Although a voltage of 135 kV was attained and held for multiple days in contaminated argon, the impurities are presumed to alter the dielectric properties of the material and therefore complete validation remains unproven.

Results from the purity monitors and temperature sensors suggest a stratification along the height of the LAr volume within the cryostat, similar to observations made during the Phase I run. The cause of this is likely due to returning LAr from the purification system being cooled below the ‘bulk temperature’ by the phase separator and reentering near the bottom of the cryostat, resulting in reduced convection and poor mixing. Resolutions, such as returning warmer LAr to the main volume, are being considered for future LArTPCs in an attempt to mitigate these effects and ensure a good, isotropic purity.

The TPC electronics were the largest source of shortfalls in the experiment which have significantly compromised the utility of the data. Along with the stuck code in the digitiser, there were multiple problems with coherent and incoherent noise, discussed further in Section 4.3.5.4.

#### 4.3.5.2 Triggering Systems: Photon Detectors and Muon Counters

The photon detector system and external muon counters also achieved expectations. Although the counters are unnecessary for the far detector, they proved critical to the success of the 35 ton. The vast majority of data was recorded whilst triggering on throughgoing muons and, as will be discussed further in Chapter 7, all worthwhile analyses rely heavily on counter information.

The photon detection system (PDS) was shown to successfully record data in both externally triggered (when using the muon counters) and self-triggered modes, where the PDS sends a trigger to the PTB upon receiving a sufficient level of scintillation light. The timing resolution of the detectors was shown to be better than 100 ns with respect to the counter timing, as shown in Figure 4.28, with signals as low as a single p.e. detected. The attenuation length in LAr may be determined by considering the signal size of scintillation flashes, using counter trigger information to determine how far from the detectors the

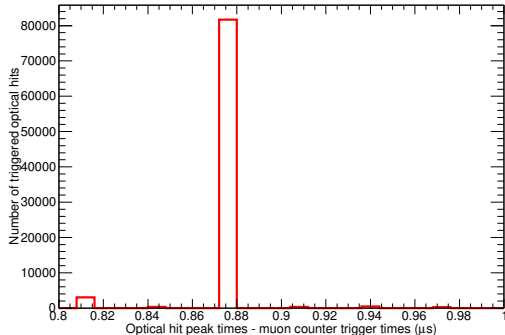


Fig. 4.28 Difference between optical hit peak times and muon counter trigger times for photon detector 3 in the 35 ton photon detection system. The binning reflects the digitization time of the photon detector electronics. Taken from [127].

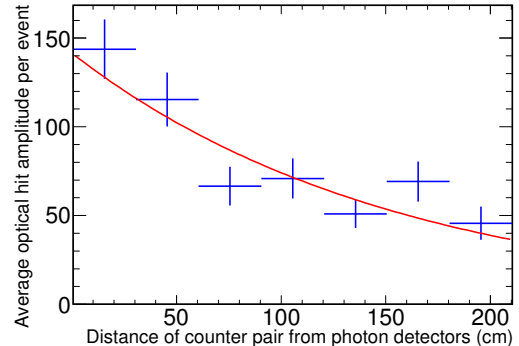


Fig. 4.29 Average Optical Hit Amplitude per Event vs. Counter Pair Positions for the 35 ton photon detection system. Error bars are statistical errors on mean hit amplitudes per bin. Taken from [127].

interaction occurred. This is demonstrated in Figure 4.29 and yields a measurement of  $155 \pm 28$  cm.

Given the noise problems in the TPC data, it was not possible to do joint analyses using the photon detectors as planned. The system performed well however and validated the concept of using WLS bars with SiPM readout as opposed to PMTs for the DUNE far detector design.

#### 4.3.5.3 DAQ and Computing

The DAQ was remarkably consistent throughout data taking following the stabilisation period. All components could be operated simultaneously with data written to disk at a steady rate, successfully demonstrating continuous readout of the detector systems. In total,  $\sim 500$ k cosmics were recorded during the 35 ton Phase II data taking, with an impressive capacity on disk of  $\sim 30$  TB.

It proved imperative to monitor the data during running as detector issues spontaneously arose on a regular basis. The large volume of data was an additional issue and finding an optimum output file size, balancing number of data files on disk with size of each file and potential for data loss upon a DAQ crash, occupied a sizeable amount of commissioning time. Additionally, a potentially disastrous failure in the alarm system for one of the computing racks resulting in serious overheating and the loss of all the machines which were running most of the online processes.

Data from the cold electronics were shown to be processed by the RCEs at a rate of 1 Gb/s but a bottle-neck in the framework restricted disk writing to 60 MB/s, resulting in an

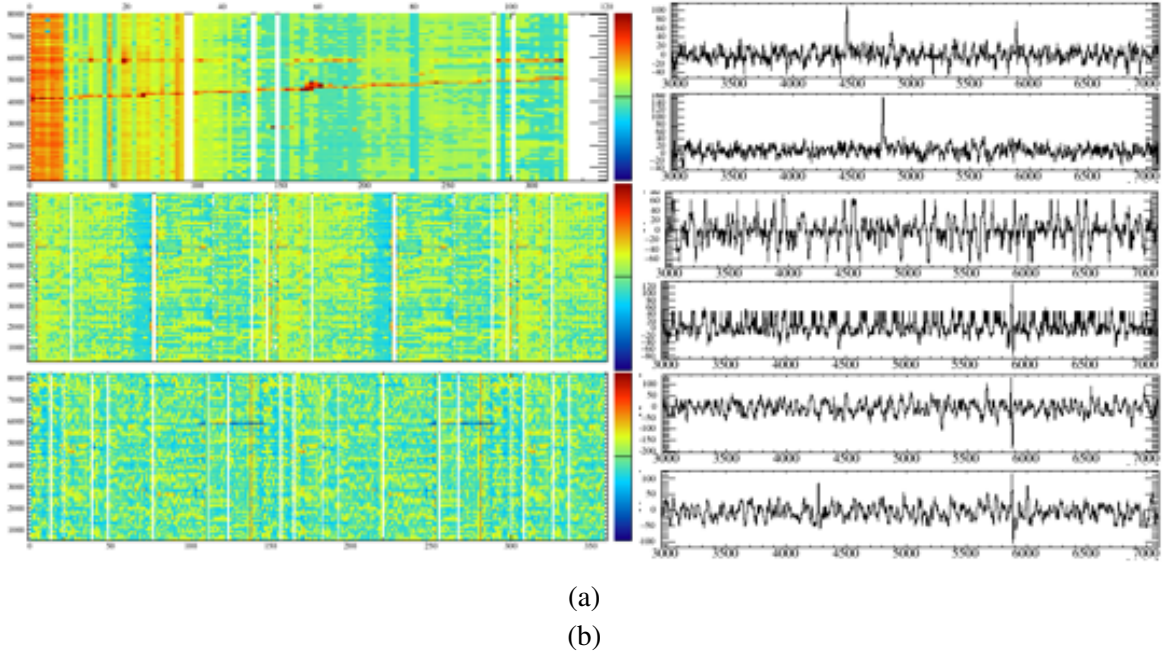


Fig. 4.30

enforced reduced data flow through the system. An event rate of 1 Hz was utilised during the run, much smaller than the design rate of 200 Hz. This could have been improved by employing zero suppression in the TPC data but this was unable to be tested as planned in the 35 ton. The event rate requires improvement before the far detector DAQ but work is underway and the experience with the 35 ton will be taken forward with most of the existing framework under development for use in ProtoDUNE.

#### 4.3.5.4 Noise Issues

An example muon track observed in the 35 ton data, along with typical waveforms recorded on the anode wires, is shown alongside an analogous muon track and detector response from simulation in Figure 4.30. It is clear...

There were multiple sources of noise in the 35 ton detector with distinct ‘modes’: the ‘normal noise state’ (which still contains numerous issues) and the ‘high noise state’ [133]. The frequency bands of noise in each state is demonstrated in Figure 4.31.

The normal noise state is characterised by 11 kHz and 100 kHz bands. The phase of the 11 kHz noise appears to alter every 64 channels, corresponding to the blocks of channels read out by ASICs sharing a common voltage regulator (four 16 channel ASICs). The correlation between the waveforms observed on the channels maintained by the same regulator is evident in the plot shown Figure 4.32. This was shown to be removed following

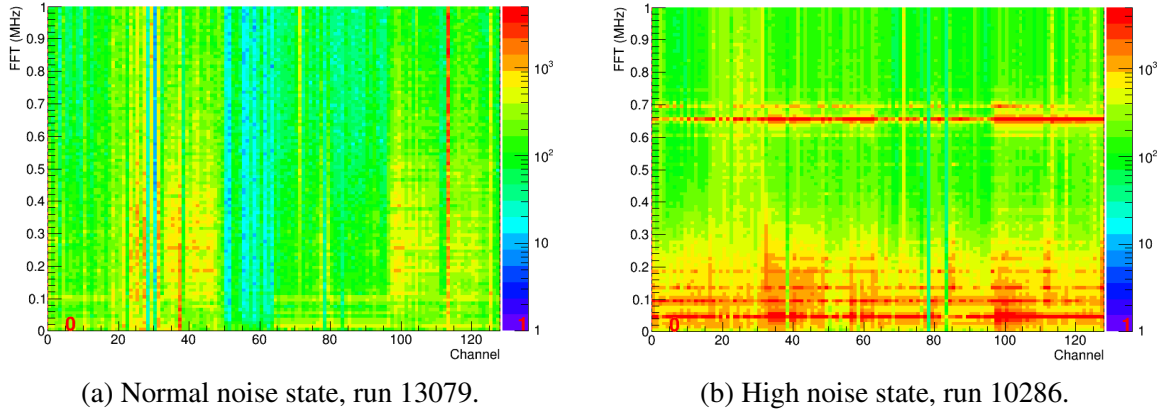


Fig. 4.31 FFT of ADC values for RCE00 for two different noise states. During the normal noise state, the noise band at 11 kHz (faintly visible at 0.011 MHz in Figure 4.31a) is present across all channels in the detector and a lot of channels also see 100 kHz frequency noise. The high noise state manifests across all channels in the detector as multiple frequency bands and render any collected data useless when present.

the run by the addition of a  $1\ \Omega$  resistor in series, effectively forming a low pass filter, and can be removed crudely in software using a coherent noise subtractor. A similar phase shift in the 100 kHz noise is observed at the boundaries between FEMBs, which are each maintained separately by the low voltage power supply. Again following the completion of the run, close inspection of the cabling found a short between the supply return line for the FE ASICs and the chassis ground for the supply. Correcting this removed all noise sources and, along with the correlated component from the voltage regulators, explained all prominent noise frequencies in the normal mode.

The high noise state was entirely unanticipated but was characterised by several features: a very high noise level is observed without saturating the ASICs; multiple frequency bands, most under 300 kHz, are observed simultaneously across all channels in the detector; these frequency bands are consistent for the duration of the high noise state but change each time the state is entered; these frequencies are also observed on a spectrum analyser connected to an APA grid plane; the current draw of the ASICs is observed to drop when in the high noise state. Furthermore, the high noise state was not observed when the cryostat was at room temperature and so could not be investigated subsequent to the end of the run. It has been understood as a collective oscillation of all detector components which is spontaneously entered, roughly every few hours, during running. Often, after a time period on the order of an hour, the system may egress from the state; it was also noted that power cycling the front end ASICs may also return the detector to the normal noise state. The noise investigations after data taking were unable to definitively identify the conditions of the abnormality but have

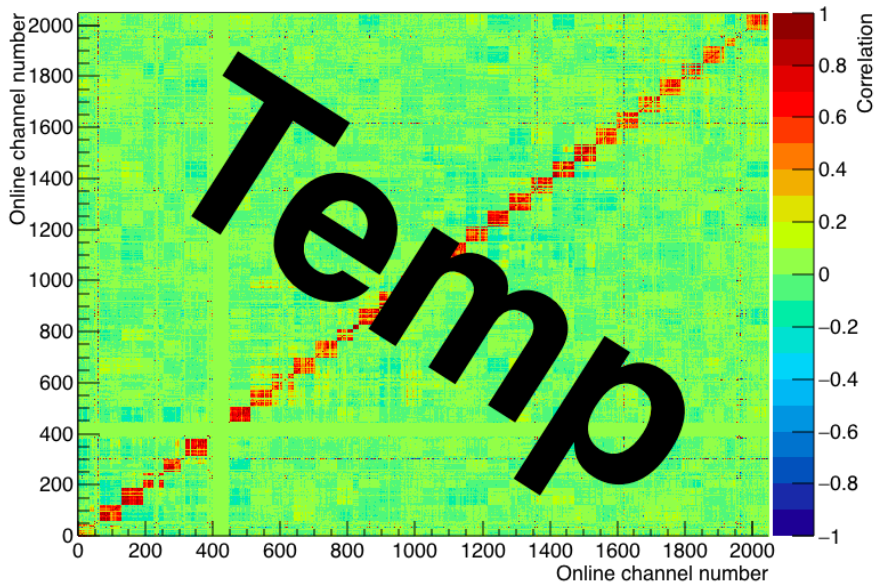


Fig. 4.32

offered suggestions as to the likely causes. The frequency of the oscillations, and the inability to induce the state in the warm system, argues strongly against external influences. The source cannot be the anode wires as this would saturate the front end electronics and, given the necessary power required to sustain the oscillations on the grid plane, the only candidate is the low voltage power supply. The difference between the 35 ton and MicroBooNE, which uses the same supplies has not observed similar problems, is the length of cabling used in the 35 ton is around 10 times greater. This may turn the negative feedback in a remote sense system into a positive feedback loop, causing the circuit to search for the correct voltage settings by overshooting and subsequently undershooting (i.e. oscillating) due to the round trip cable delay being longer than the circuit response time. The strong frequency bands at 650 kHz, which are always present across all channels whenever the high noise state is entered, unlike the other frequencies, is likely due to the oscillating cable acting as a cable resonator. During the run, it was observed that APA1 (the short, bottom centre, APA) was most prone to these issues and was actually left unpowered during much of the data taking. This may be explained by considering the most likely coupling is to the FE electronics for this APA (the only one where these are at the bottom) to the grid plane, which then couples to the cathode on the short drift side and from there is transferred to the other APAs in the detector. The decreased capacitance of the cable in air than when submerged in LAr explains why this state could not be induced following the end of operations.

Finally, it is observed that the minimum noise in the detector is higher than in MicroBooNE. Although the induction wires are much longer, there is still an increase greater than could be accounted for by the larger capacitance of the wires. The noise experts suggest there may be a common mode noise on the supply line which may intensify the overall noise levels without inducing the high noise state; this would enter via the cathode, then the grid planes and then the induction wires and would explain why this plane sees more noise than the collection view.

The noise issues encountered in the 35 ton, though unexpected, have been critical to understanding the issues which may be present in large scale LArTPCs and would be seriously detrimental to the DUNE project if encountered in the far detector. Every effort has been made to understand the issues with the 35 ton and ensure the eventual success of the experiment.

## 4.4 Summary

The 35 ton experience, while unable to deliver the high quality data anticipated for the purpose of physics analyses, was invaluable to the DUNE strategy.



# **Chapter 7**

## **Analysis of 35 ton Data**

Could this chapter be a little more specifically titled?

The 35 ton run (see Section 4.3) provided 22 days of good quality (high purity, stable field (250 V/cm), stable DAQ), analysable data. Due to the issues encountered, high quality physics analyses proved very challenging and instead studies, particularly those presented here, focused on trying to understand the detector and characterise previously untested responses. In this respect, the 35 ton proves to be a vital experiment in informing the next generation of prototypes and even the final DUNE far detector design. It also boasts datasets which no planned experiment will before the full DUNE modules; it is therefore essential as much information as possible is extracted from the 35 ton analyses.

Before analyses are presented, techniques developed to enhance the quality of the data, and the data selection, will be discussed in Section 7.1. A short section demonstrating how LAr purity may be determined from data is contained in Section 7.2 before the main analyses, concerning tracks passing across APA gaps and through the APA frames, are presented in Section 7.3 and Section 7.4 respectively. Finally, a brief investigation into the performance of basic shower and calorimetric reconstruction on the 35 ton data is discussed in Section 7.5. A summary is provided in Section 7.6.

### **7.1 Preparing 35 ton Data for Analysis**

To ensure analyses are as accurate as possible, careful pre-selection and preprocessing of the data is performed. Methods for producing the analysable sample are discussed in the section.

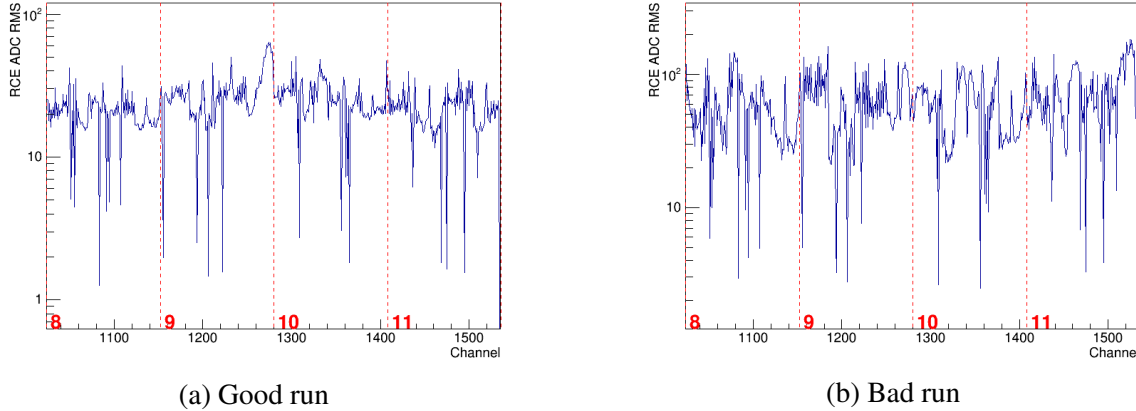


Fig. 7.1 Comparison between noise levels for ‘good’ and ‘bad’ 35 ton runs. The channels shown are on APA2 (online convention, APA0 offline) and are read out by RCEs 8 through 11 (labelled). The increase in read out charge RMS is evident in the case of the noisy run. These plots are from runs 15797 (Fig 7.1a) and 15790 (Figure 7.1b) and were taken only 50 minutes apart.

### 7.1.1 Selecting the Data

The level of noise present in the TPC data varied hugely between runs – this is evident from analysing the RMS of the charge read out on a particular channel. Figure 7.1 shows a comparison of this metric for ‘good’ and ‘bad’ runs.

Runs which exhibited the lowest noise were selected for analysis. In all there were 1269 runs used representing some data taken before the FNAL site wide power outage (3rd March 2016) with most the week after stabilising the experiment again (9th March – 17th March). A selection of bad channels, classified as either ‘dead’ (electrically) or ‘bad’ (exhibit sufficiently more than average noise), represent 8% of the total number of channels.

Due to the continuous nature of data taking, there is a non-trivial correlation between a ‘DAQ event’, a collection of fragments read out by the DAQ, and a ‘physics event’, an event in which particle interactions occurred. The external triggers used in the 35 ton, namely the external muon scintillators and the photon detectors, are used to define the event time. Given the trigger rate at which most data was taken ( $\sim 1$  Hz), a typical run comprising a few thousand events will only contain  $\mathcal{O}(10)$  triggered events. Furthermore, given the data format, these events often straddle multiple DAQ events (refer to Figure 6.5 for a demonstration of this). A splitter/stitcher module is employed to search for triggers within runs and construct physics events containing the useful information for analysis. This produces a file with just this relevant information, which are then used for analysis.

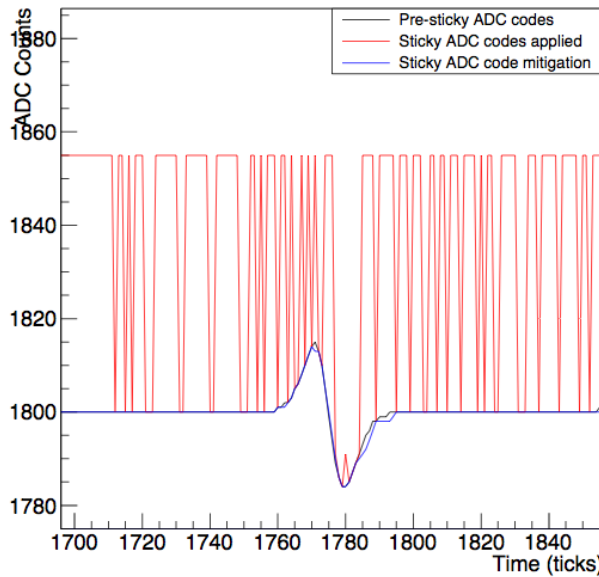


Fig. 7.2 Simulated demonstration of the method used to correct for stuck codes in the 35 ton data. On a given channel, ADCs exhibiting the consequences of this problem are corrected by interpolating charge at neighbouring time units. This is tested by simulating a waveform and adding the observed stuck code effect; the efficacy of the method at correcting the afflicted bits can then be evaluated.

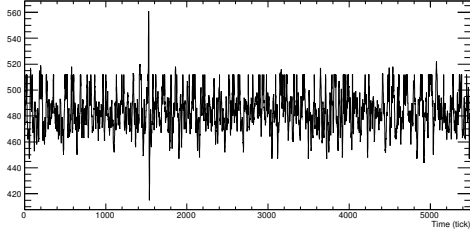
### 7.1.2 Improving Data Quality

Two issues present in the raw data, namely the presence of correlated noise and the stuck bits in the digitiser, are dealt with as an initial step of the reconstruction. First, an algorithm attempting to correct for the stuck bits analyses waveforms on a wire and identifies problematic ADCs; interpolating between charges read out at neighbouring times is successful at reconstructing the initial waveform in most cases. Figure 7.2 demonstrates this interpolation method on simulated data. The effect of applying this algorithm on a full waveform, to correct for all the stuck bits, is apparent in Figure 7.3.

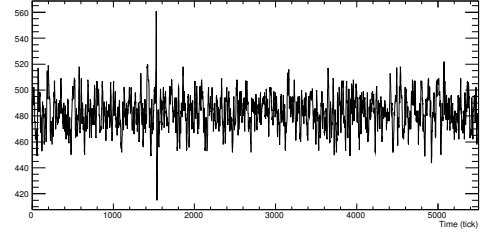
Following this process, a coherent noise removal stage is applied. This simply looks at the average noise across channels sharing a front-end voltage regulator and removes this component from the readout ADC for each channel. The effect of this correction is seen in Figure 7.4.

### 7.1.3 Reconstructing Muon Tracks

All analyses discussed below only make use of information recorded on the collection planes. Since the induction wires are longer (a necessity for wrapping), a larger capacitance results in higher noise levels, complicating the reconstruction. In general, after applying the

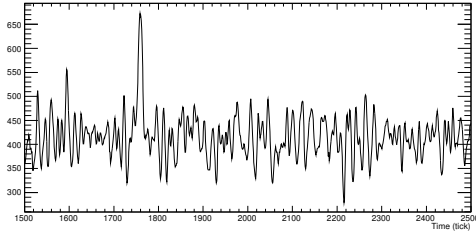


(a) Raw waveform before correcting for stuck bits.

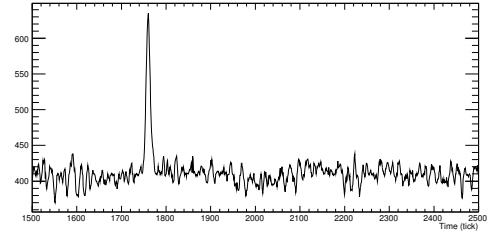


(b) After applying stuck bit mitigation.

Fig. 7.3 The effect of applying stuck bit mitigation to a waveform as seen in raw data. This particular waveform is from run 15660, channel 722 (induction channel).



(a) Waveform before removing coherent noise.



(b) After removing coherent noise.

Fig. 7.4 The effect of removing coherent noise from all channels on a voltage regulator. This waveform is from run 15660, channel 2010 (collection channel). The signal is noticeably larger following this process, considerably improving reconstruction performance.

refinements outlined in Section 7.1.2, the signals on the collection channels are prominent enough for competent analyses. The methods used to select tracks are described in this section and applied during the subsequent studies.

Using only the collection plane presents challenges, the most obvious being the impossibility of full 3D reconstruction. A hit on a collection wire at a given time gives well-defined  $x$  and  $z$  coordinates but cannot give any information in the  $y$ -direction. ‘Quasi-3D’ reconstruction is achieved by making use of the external counters. Through-going muons are triggered by the coincidence of hits in two opposite counters; this information can be used to give a crude handle on the  $y$  position of hits.

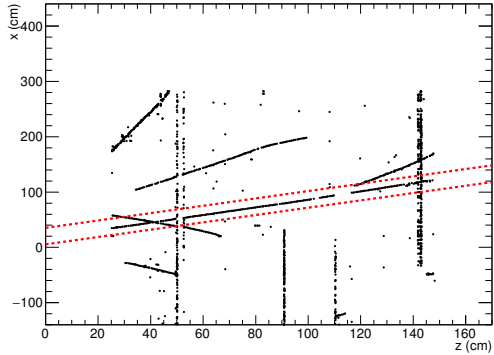
Figure 7.5 outlines the stages of selecting hits originating from the particle track which caused the trigger. Figure 7.5a shows all hits from an example event containing a through-going muon. The first stage of track selection involves taking those hits which lie in the ‘counter shadow’, the narrow section of collection plane area physically inbetween the opposing counters through which the triggering particle passed. The hits which remain are shown in Figure 7.5b. The track hits are visible along with further, unrelated hits. These are removed by requiring that only hits on wires with single occupancy be kept, and then applying a linear fit and removing all hits with residual  $> 2$  cm. The final output after these stages is shown in Figure 7.5c.

The result of this track selection, as evident from Figure 7.5c, is a well-formed, high quality track with which it is possible to perform analyses. These will be the focus of the remainder of this chapter.

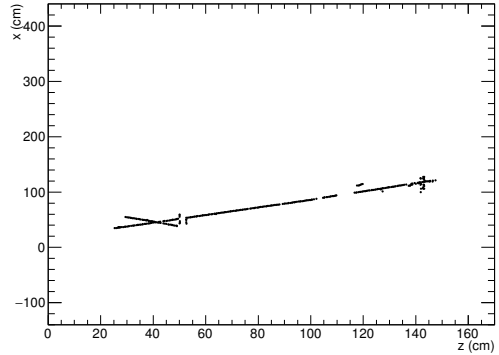
#### 7.1.4 Preparing Simulated Data

Comparisons with simulated data are often essential in understanding various phenomena in the data. Throughout the analyses presented in this chapter, simulations were used to aid investigations and therefore it is important to ensure the Monte Carlo is as similar to the real data as possible.

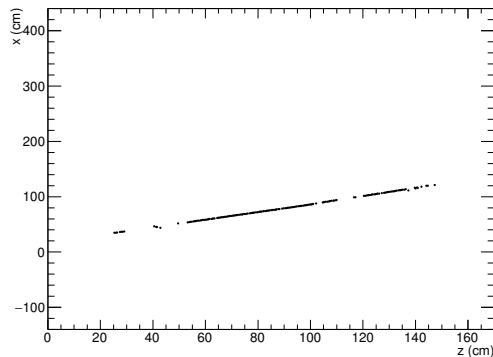
The standard LArSoft simulation tools were used as described in Section 5.1, employing the CRY cosmic ray generator. The data passing through the detector was filtered on counter coincidences, exactly as the raw data is triggered. The simulated data was then processed in the same way as the real data and reconstructed using the methods described in Section 7.1.3.



(a) All hits before any track selection. The red lines represent the boundary defined by the edges of the two counters causing the trigger.



(b) Hits in the counter shadow.



(c) Hits on single wire occupancy and with residual  $< 2$  cm.

Fig. 7.5 Demonstration of the successive stages applied to hits on collection wires in order to select hits from the through-going track associated with the particle which caused the trigger. The hits left after all stages are taken forward into the analyses.

## 7.2 LAr Purity from Crossing Muons

The purity of the liquid argon is directly related to the concentration of electronegative impurities present in the medium which may capture drift electrons before they reach the anode planes. This gives rise to the concept of ‘electron lifetime’,  $\tau$ , which affects the charge  $Q_{\text{collected}}$  collected by the readout wires;

$$Q_{\text{collected}} = (Q_{\text{ionised}} - Q_{\text{recombination}})e^{-t/\tau}, \quad (7.1)$$

where  $Q_{\text{ionised}}$  is the ionised charge,  $Q_{\text{recombination}}$  is the charge lost due to initial recombination with the position ion and  $t$  is the drift time of the charge packet.

It is possible to make a rough measurement of the electron lifetime directly from crossing muon tracks and two complimentary methods are reported here – using hits from single tracks which make a large angle to the APA frames and using multiple tracks parallel to the APAs binned into discrete drift distances. These are described in Sections 7.2.1 and ?? respectively. The analysis here serves mainly to demonstrate how these measurements are made and to produce preliminary results; a rigorous assessment is a in-depth study in itself and is not attempted in this thesis.

### 7.2.1 Single Track LAr Purity Measurements

## 7.3 APA Gap-Crossing Muons

One of the primary motivations for the design of the 35 ton TPC was to test its modular form, where a single drift region is read out by multiple anode assemblies. Particles passing through the detector will inevitably leave deposits in multiple TPCs and will pass uninstrumented regions of the detector, such as gaps in between neighbouring APAs. Many APA gap-crossing tracks are evident from the event display in Figure 7.6 and an example such track is demonstrated schematically in Figure 7.7. It is essential the implications of this design choice are understood before constructing the far detector modules, each of which will contain 150 APAs.

The 35 ton dataset consisting of muons which pass across the face of APAs and therefore deposit charge in consecutive TPCs is discussed in this present section. An analysis of these tracks to calculate the size of the gaps is presented in Section 7.3.1 and a study of the charge deposited by such tracks is the subject of Section 7.3.2.

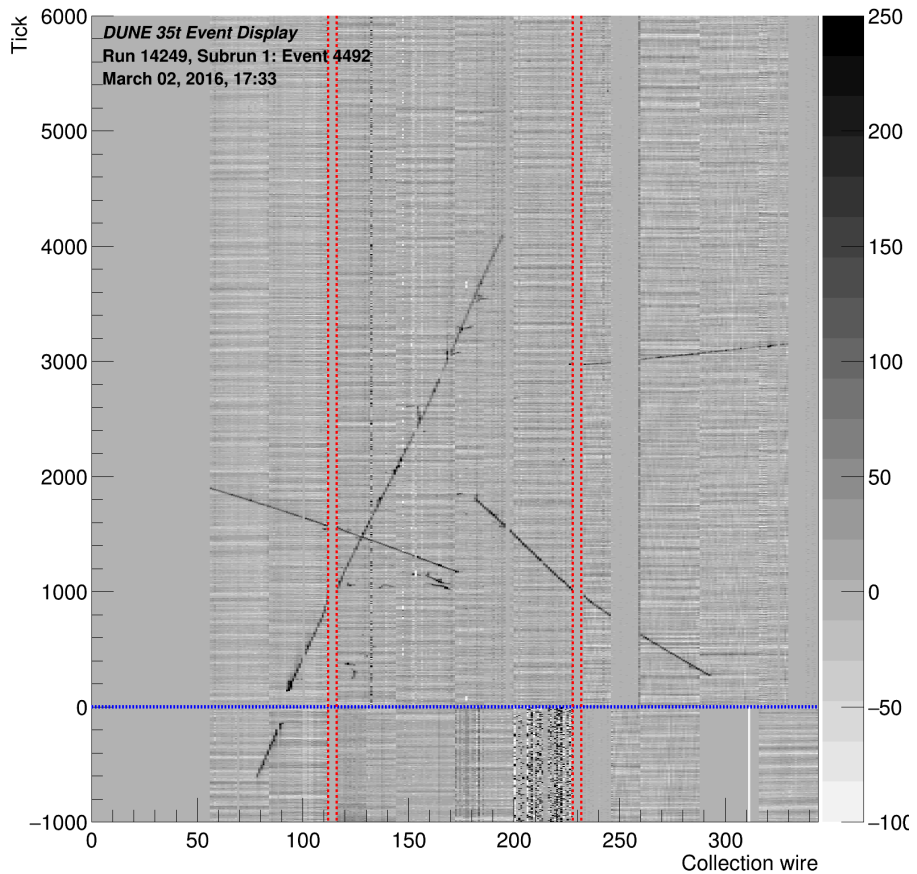


Fig. 7.6 Event display showing tracks passing across APA gaps and also through the APAs. A study of the tracks which pass across gaps between the APAs (the red lines) is the subject of Section 7.3. There is a visible offset apparent as the track crosses through the APAs (the blue line); correcting for  $T_0$  would eliminate this and yield a single accurately connected track. This is discussed further in Section 7.4.

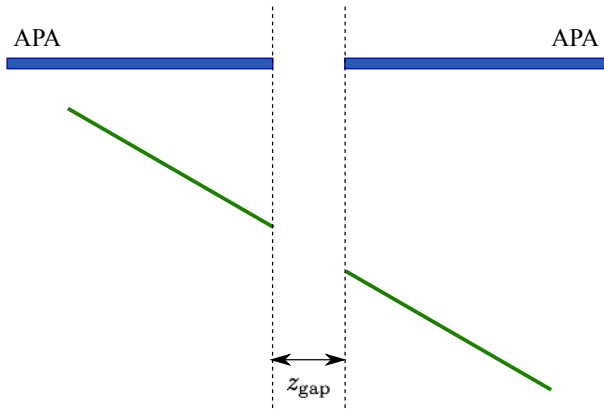


Fig. 7.7 Schematic showing an example APA gap-crossing track as viewed looking down from the top of the detector. The vertical direction represents the drift direction ( $x$ ); the horizontal direction represents the  $z$ -direction. In general, these tracks make an angle with respect to the face of the APAs, as shown in the figure. As the gap in between the APAs is uninstrumented, no charge is deposited in this region.

### 7.3.1 APA-Gap Offset Determination

It is possible to use these gap-crossing tracks to make measurements of the gaps between each of the APAs. This involves aligning the track segments from neighbouring TPCs, demonstrated in Figure 7.8. The value of the  $z$ -offset,  $\Delta z$ , is determined by considering a range of offset hypotheses, performing a linear fit and finding the offset which minimises the residual least squares

$$L = \sum_i^{nhits} (o_i - e_i)^2, \quad (7.2)$$

where  $o_i - e_i$  is the distance from hit  $i$  to the best fit line.

There are eight gaps which can be measured from the data, demonstrated in Figure 7.9. Due to very low statistics, it was found measurements of the gaps on the short drift volume side of the APAs were not possible using the 35 ton data. Analysis of the gaps using tracks passing through the long drift volume, hereafter named TPC1/TPC3, TPC1/TPC5, TPC3/TPC7 and TPC5/TPC7, was therefore the focus of this study.

A number of cuts were applied to ensure only high quality tracks were included for analysis:

- Only hits greater than 1 cm and less than 15 cm away from the gap were included in the track segments. The purpose of this cut is to limit the effect of multiple scatterings and the poorly understood region closest to the gap, where charge deposited in the uninstrumented region may later be collected.

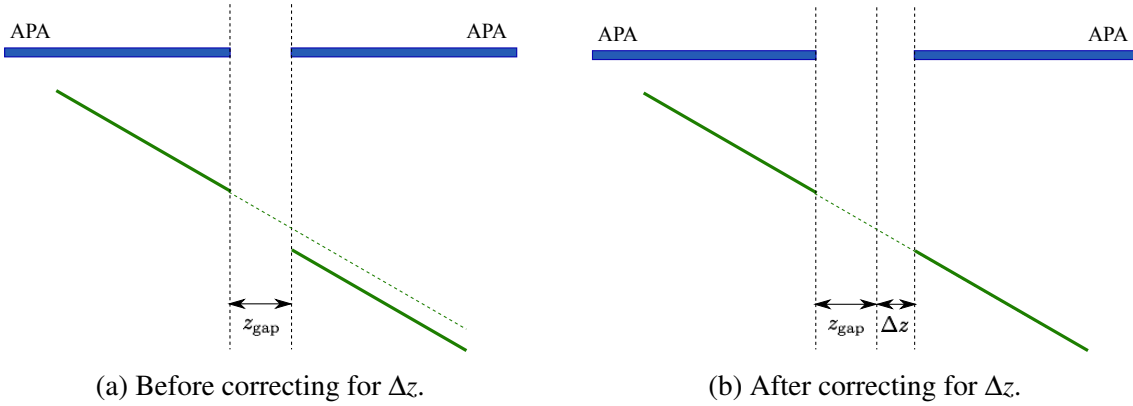


Fig. 7.8 Schematic showing an example track crossing two drift regions offset by an unknown quantity  $\Delta z$ . The effect of this is evident from the track deposits (Figure 7.8a) and can be corrected by ensuring the segments are aligned between the TPCs (Figure 7.8b).

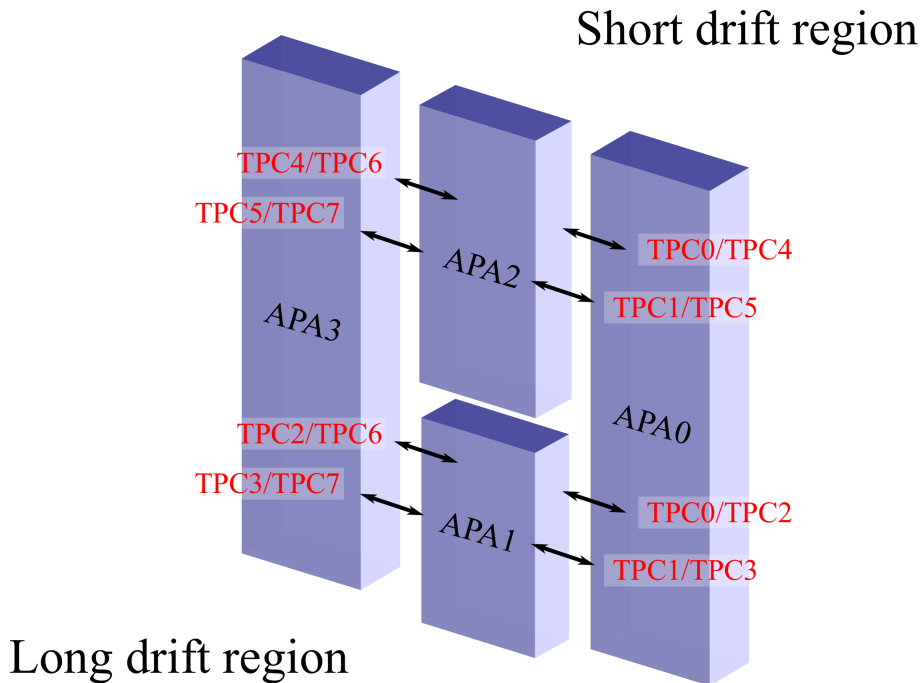


Fig. 7.9 Illustration of the eight gaps between the four APA frames.

- Each track segment must contain at least ten hits to allow an accurate measure of the gradient.
- The angle between the track segments either side of the gap must be less than  $2^\circ$  to remove any poorly reconstructed tracks, or segments originating from different particle tracks.
- The angle the track makes with respect to the APA face must be large enough that the gap offset effect can be measured to an acceptable accuracy. It is common in the 35 ton to refer to a ‘counter gradient’, the offset between the two counters forming the through-going particle trigger in the drift direction, in units of counter length (refer to Figure ??). The tracks must have a counter gradient of at least three.

### 7.3.1.1 Measuring the APA Gaps

The gap which may expect the largest number of crossers is TPC5/TPC7 and so the method will be demonstrated using data from this channel. The  $z$ -offset determined using the method and cuts described above is shown in Figure 7.10. An unexpected feature is evident from this distribution; there is not a single peak but two, seemingly related to the angle which the through-going particle makes with respect to the APAs.

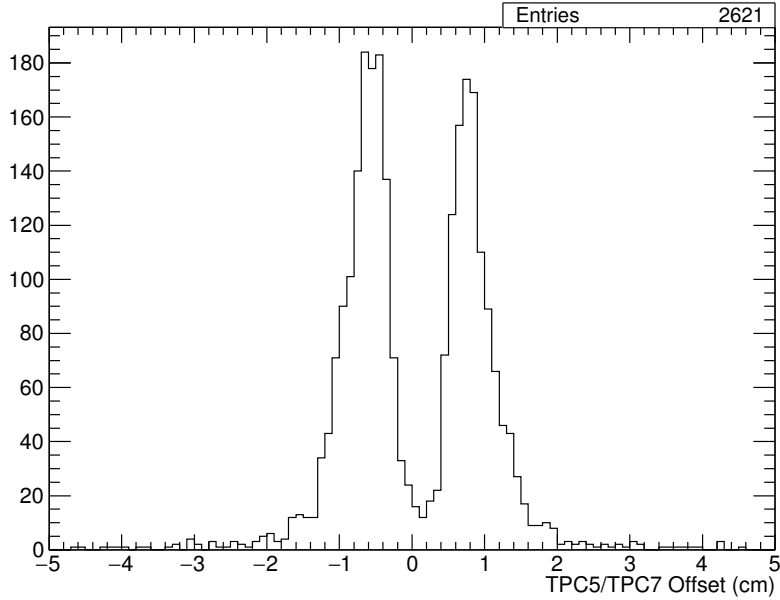
One explanation for this observed double-peak effect involves considering the possibility of additional offsets from the assumed positions of the APAs. This is demonstrated in Figure 7.11. It appears an offset in the  $x$ -position of the APAs could result in the problems encountered in the data. In order to test this, these offsets were artificially introduced into the simulation; the findings are presented in Figure 7.13. It appears the distribution of  $\Delta z$  measured from the data is consistent with APAs with offsets from expectation in both  $x$  and  $z$ . Moreover, it may be possible to measure both offsets from the same data set.

It is clear from Figure 7.13 that the  $z$ -offset may be determined as the minimum between the angular-separated distributions. This can be justified by geometrical considerations, explained in Figure 7.14. In this case, this may be achieved by fitting a function of the form

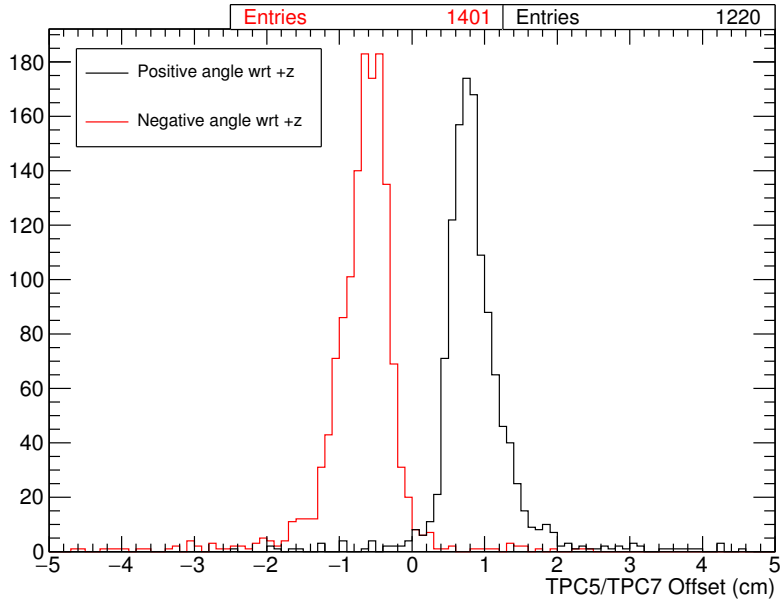
$$f(x) = a(x - b)^2 + c \quad (7.3)$$

and extracting parameter  $b$  as the true value of  $\Delta z$ . This is shown in Figure 7.15.

Using this measured value of  $\Delta z$ , the offsets can be analysed again, this time measuring the  $x$ -offset by correcting for the  $z$ -offset. The measured  $x$ -offset distribution is shown in Figure 7.16. With this value of  $\Delta x$ , the  $z$ -offset can be evaluated once more to ensure the distribution contains a single peak, as initially expected. This is confirmed in Figure 7.17.



(a) Full distribution.



(b) Separated by the angle the track makes to the APAs.

Fig. 7.10 The  $z$ -offset for the TPC5/TPC7 gap measured in the 35 ton data. A very noticeable double-peak structure is evident in Figure 7.10a; this bias appears to be related to the sign of the angle the particle track makes to the APA planes.

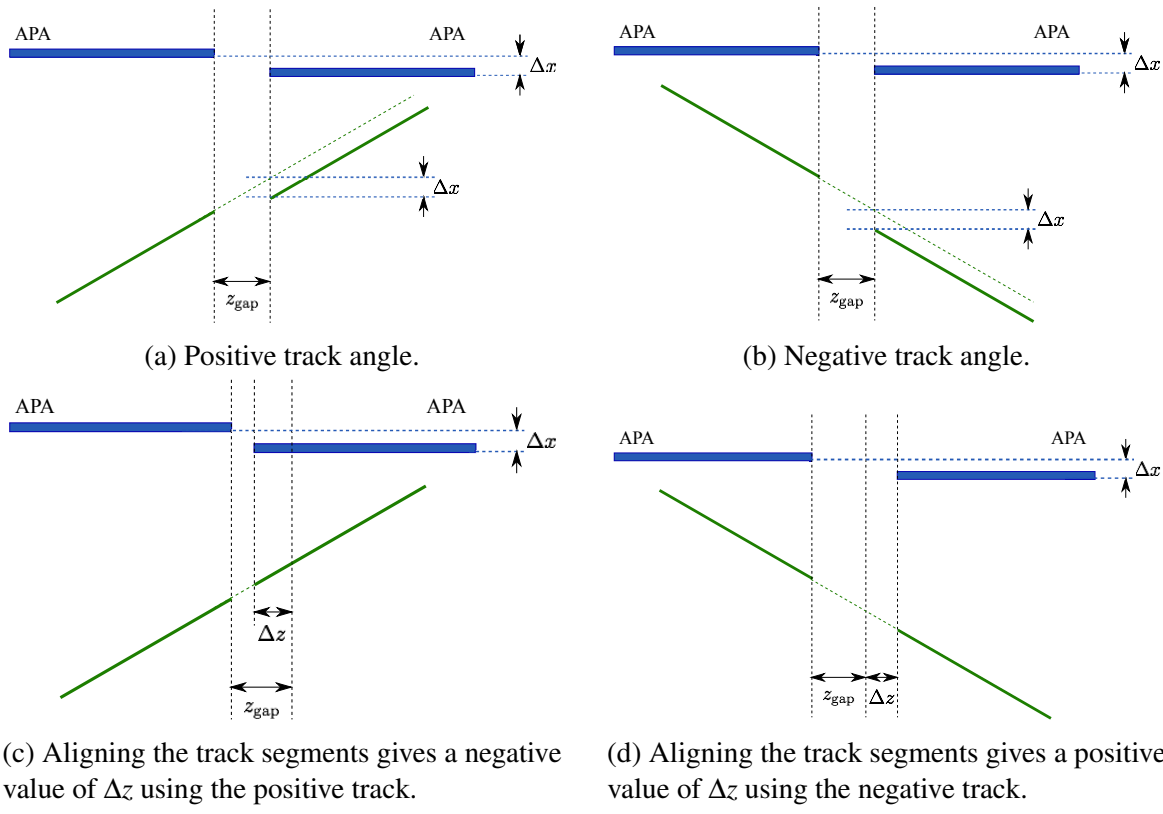


Fig. 7.11 Demonstration of how an  $x$ -offset in the positions of the APAs can explain the degeneracy evident in the  $z$ -offset measured using the 35 ton data (Figure 7.10). In the left-hand plots, Figures 7.11a and 7.11c, the through-going particle makes a positive angle to the face of the APAs and in the right-hand plots, Figures 7.11b and 7.11d, the particle is travelling with a negative gradient. In both cases, the offset of the APAs in the  $x$ -direction is the same. It is clear from Figures 7.11c and 7.11d how the sign of the measured  $\Delta z$  is dependent on the angle of the track.

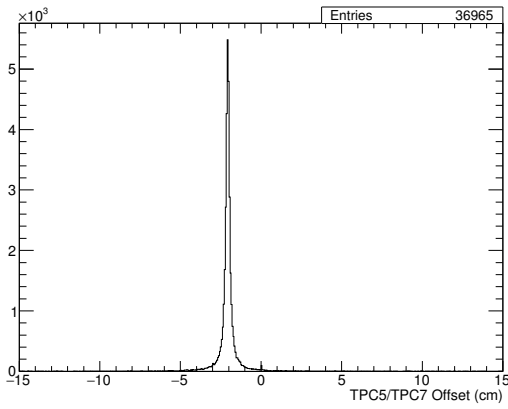
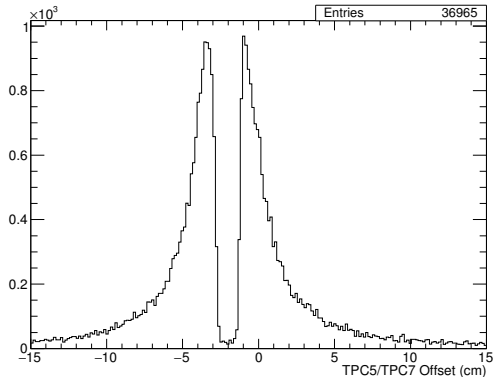
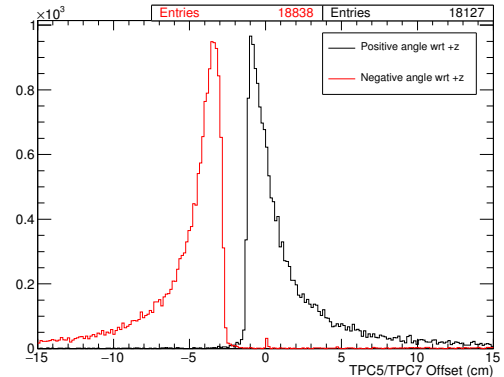
(a)  $z\text{-offset} = 2 \text{ cm}$ ,  $x\text{-offset} = 0 \text{ cm}$ .(b)  $z\text{-offset} = 2 \text{ cm}$ ,  $x\text{-offset} = 0.5 \text{ cm}$ .(c)  $z\text{-offset} = 2 \text{ cm}$ ,  $x\text{-offset} = 0.5 \text{ cm}$ .

Fig. 7.12 Studies of the effects of offsets in the positions of the APAs in simulation. Artificial  $z$ - and  $x$ - offsets are introduced and their impact observed in the measurements of  $\Delta z$ . Figure 7.13a shows the effect of an offset in the  $z$ -direction; as expected, there is a single peak measuring the inputted value. Figures 7.13b and 7.13c show the consequence of offsets in both the  $x$ - and  $z$ -directions. This appears to show exactly what is seen in the 35 ton data (Figure 7.10).

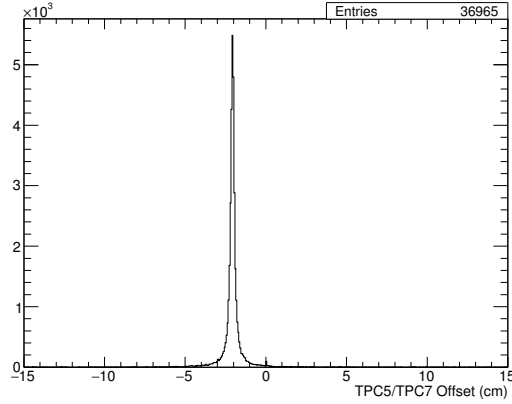
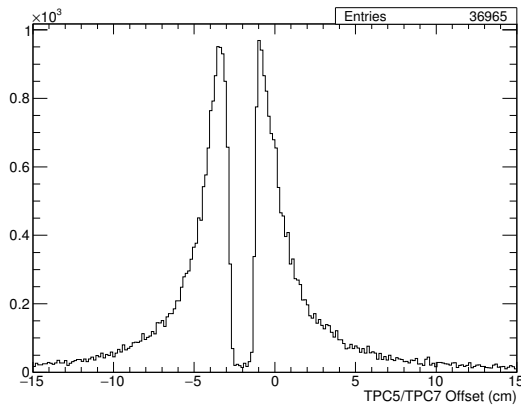
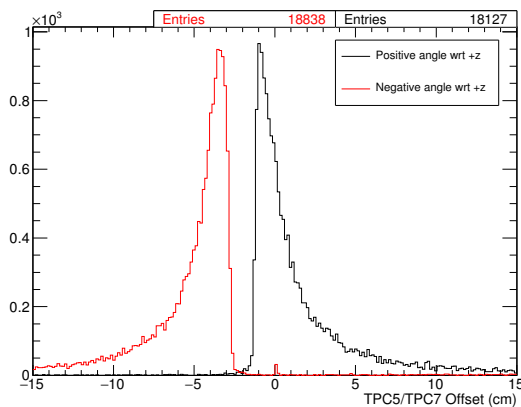
(a)  $z\text{-offset} = 2 \text{ cm}$ ,  $x\text{-offset} = 0 \text{ cm}$ .(b)  $z\text{-offset} = 2 \text{ cm}$ ,  $x\text{-offset} = 0.5 \text{ cm}$ .(c)  $z\text{-offset} = 2 \text{ cm}$ ,  $x\text{-offset} = 0.5 \text{ cm}$ .

Fig. 7.13 Same as previous page – which is better? I prefer the layout of the previous page but I like this one because you can see the 2cm offset in line with each other down the page! Studies of the effects of offsets in the positions of the APAs in simulation. Artificial  $z$ - and  $x$ - offsets are introduced and their impact observed in the measurements of  $\Delta z$ . Figure 7.13a shows the effect of an offset in the  $z$ -direction; as expected, there is a single peak measuring the inputted value. Figures 7.13b and 7.13c show the consequence of offsets in both the  $x$ - and  $z$ -directions. This appears to show exactly what is seen in the 35 ton data (Figure 7.10).

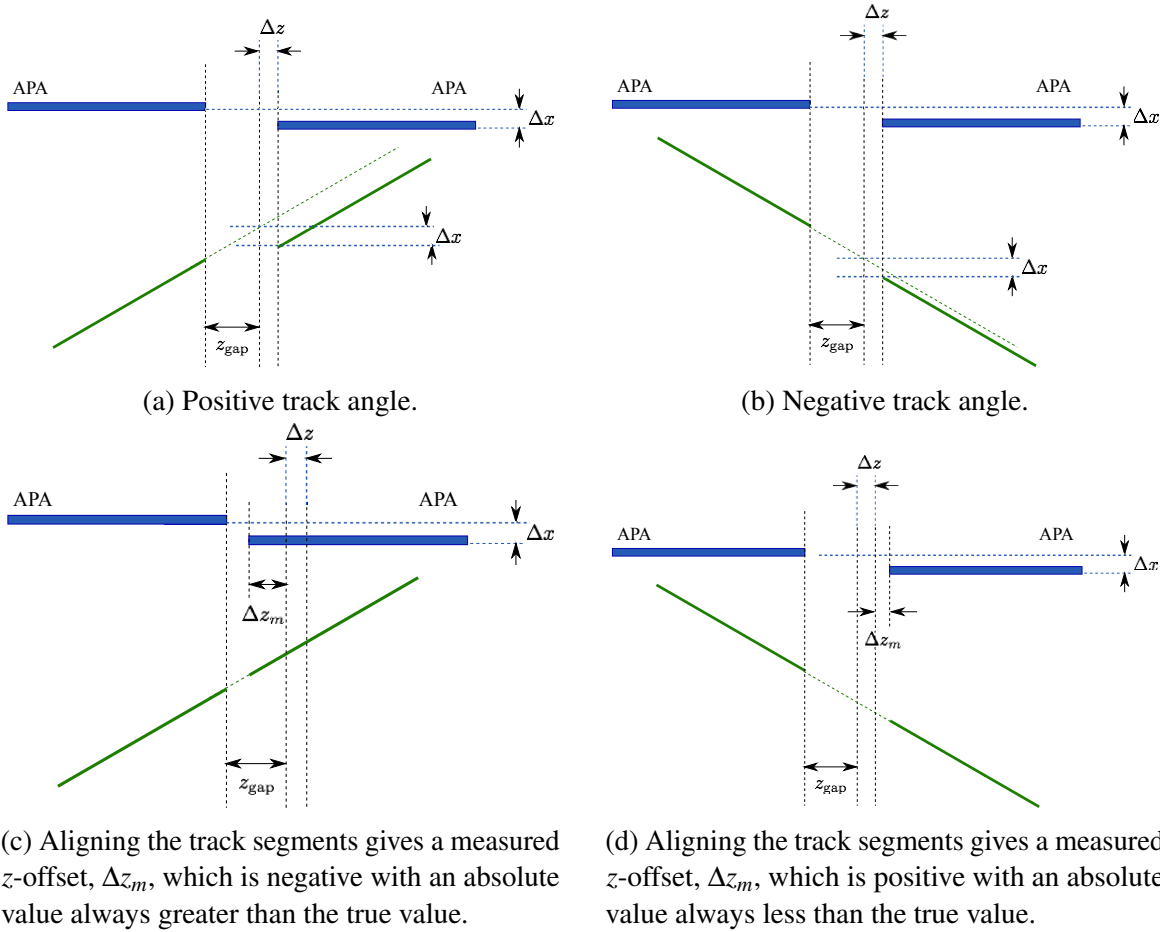


Fig. 7.14 Demonstration of the effects of offsets in both the  $x$ - and  $z$ -directions in the determination of  $\Delta z$  between TPC5 and TPC7. With an  $x$ -offset present, it is impossible for the true value of  $\Delta z$  to be measured – this is evident from Figure 7.13. It is clear from these geometrical considerations how the measured offset  $\Delta z_m$  will populate distributions either side of the true value; the true value  $\Delta z$  is given by the minimum between the two distributions.

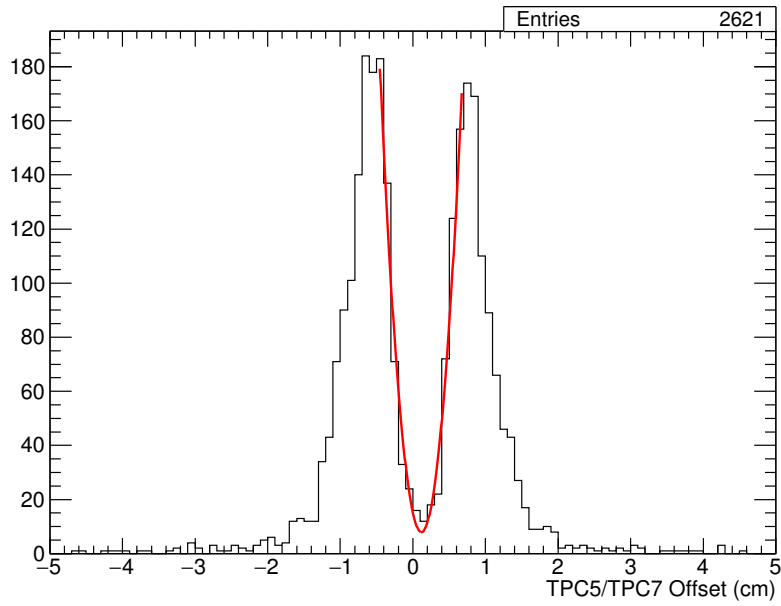


Fig. 7.15 Extraction of the true value of  $\Delta z$  from the full distribution of measured  $z$ -offsets. A measured value of  $0.117 \pm 0.007$  cm is found.

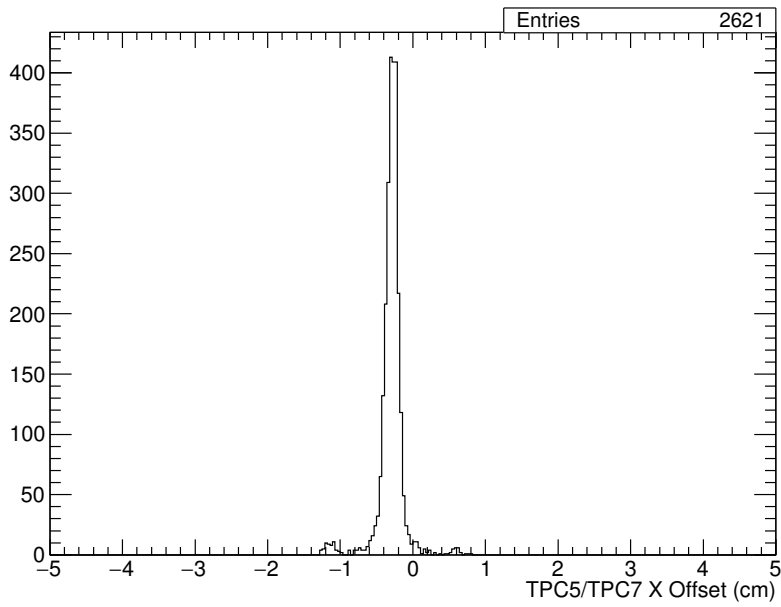


Fig. 7.16 Measurement of the  $x$ -offset between TPC5 and TPC7 after applying the  $z$ -gap corrected determined using the method described in the text and Figure 7.15. A measurement of  $-0.286 \pm 0.002$  cm is determined.

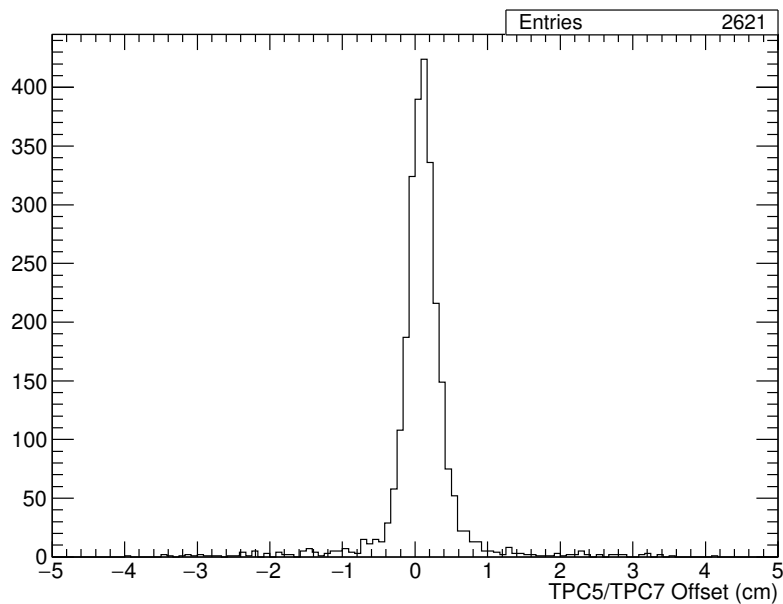


Fig. 7.17 Measurement of the  $z$ -offset between TPC5 and TPC7 after applying the  $x$ -offset determined from Figure 7.16. As initially anticipated, there is a single peak distributed around the true value of the offset. This validates the method used and confirms the initial presence of an  $x$ -offset between the neighbouring APAs. The final measurement of  $\Delta z$  is  $0.103 \pm 0.004$  cm which agrees reasonably with the value measured previously ( $0.117 \pm 0.007$  cm from Figure 7.15).

### 7.3.1.2 Measurements of the APA Offsets

The offsets apparent from the data for all of the gaps accessible using TPC tracks in the long drift volume were determined as described in Section 7.3.1.1. Appendix ## contains all relevant figures (does an appendix seem a good idea here? I don't think we need the same figures as the previous section for each of the gaps here, but might be nice to have them somewhere?). Table 7.1 contains all the measurements and the new gaps, taking these offsets into account, are presented in Table 7.2.

NOTE: this discussion is exactly the same as what I put in the paper... is this a problem?  
It seems silly rephrasing everything but I understand it may be necessary.

The determined errors are statistical only; the effects of systematic uncertainties were not considered and assumed to be negligible in comparison. Given the method used to determine these offsets, which involved multiple fits in differing parameter spaces, one may expect correlations between the uncertainties in the offsets measured in  $x$  and  $z$ . The implications of this correlation was considered by varying the value of each parameter across the range of its  $1\sigma$  error and evaluating the effect of this on subsequent measurements. It was found this is negligible in the context of the determined uncertainties and would not justify thorough evaluation.

There appears to be some consistency in the measurements of the  $x$ -offsets by considering differences in this value between TPC1 and TPC7. Despite the fact they do not neighbour each other, this is possible by considering the successive offsets measured between TPC1/TPC3 and TPC3/TPC7, and TPC1/TPC5 and TPC5/TPC7. An exceptional agreement is seen between the two values. There also seems to be slight evidence of a rotation between TPC1 and TPC7 when considering the associated  $z$ -offsets; the offset at the top of the APA (when measured via TPC5) is greater than at the bottom (when measured via TPC3). However, this can certainly be explained in the context of the limitations of the method and statistical fluctuations and would require more data and a more robust approach to justify these claims. Such analysis is not possible with the 35 ton data.

The method demonstrated here will have direct implications for similar studies using the full DUNE far detector. All the gaps between the APAs, both in the drift and  $z$  directions, will need to be understood for accurate reconstruction and are essential in order to make the precise physics measurements DUNE wishes to. For example, accurate calorimetric reconstruction is imperative in order to perform particle identification and shower energy determination and is directly related to the drift time of the ionisation electrons; any offsets in APA positions will lead to systematic uncertainties in this information.

Table 7.1 Measurements of all the APA offsets determined from the 35 ton TPC data. The method followed is described in Section 7.3.1.1. The first row represents the initial measurements of the  $z$ -offset from the two-peak distribution, with the following two lines detailing the measured offsets that follow from these results.

	TPC1/TPC3	TPC1/TPC5	TPC3/TPC7	TPC5/TPC7
Initial $z$ -offset (cm)	$-0.64 \pm 0.04$	$0.15 \pm 0.01$	$0.58 \pm 0.06$	$0.117 \pm 0.007$
$x$ -offset (cm)	$-0.377 \pm 0.006$	$-0.252 \pm 0.002$	$-0.16 \pm 0.01$	$-0.286 \pm 0.002$
$z$ -offset (cm)	$-0.63 \pm 0.02$	$0.131 \pm 0.007$	$0.55 \pm 0.03$	$0.103 \pm 0.004$

Table 7.2 The corrected gaps between the APAs, in  $x$  and  $z$ , based on the offsets measured (Table 7.1).

	Assumed (cm)	Offset (cm)	Corrected (cm)
TPC1/TPC3 $x$ -gap	0	$-0.377 \pm 0.006$	$-0.377 \pm 0.006$
TPC1/TPC5 $x$ -gap	0	$-0.252 \pm 0.002$	$-0.252 \pm 0.002$
TPC3/TPC7 $x$ -gap	0	$-0.16 \pm 0.01$	$-0.16 \pm 0.01$
TPC5/TPC7 $x$ -gap	0	$-0.286 \pm 0.002$	$-0.286 \pm 0.002$
TPC1/(3)/TPC7 $x$ -gap	0	$-0.538 \pm 0.003$	$-0.538 \pm 0.003$
TPC1/(5)/TPC7 $x$ -gap	0	$-0.537 \pm 0.010$	$-0.537 \pm 0.010$
TPC1/TPC3 $z$ -gap	2.53	$-0.63 \pm 0.02$	$1.90 \pm 0.02$
TPC1/TPC5 $z$ -gap	2.08	$0.131 \pm 0.007$	$2.211 \pm 0.007$
TPC3/TPC7 $z$ -gap	1.63	$0.55 \pm 0.03$	$2.18 \pm 0.03$
TPC5/TPC7 $z$ -gap	2.08	$0.103 \pm 0.004$	$2.183 \pm 0.004$
TPC1/(3)/TPC7 $z$ -gap	4.16	$-0.08 \pm 0.04$	$4.08 \pm 0.04$
TPC1/(5)/TPC7 $z$ -gap	4.16	$0.23 \pm 0.01$	$4.39 \pm 0.01$

### 7.3.2 Charge Deposited by APA Gap-Crossing Muons

The charge deposited by gap-crossing particles cannot be collected in the dead regions between the APA frames. It is interesting to consider where the charge is read out in order to further understand the implications of a modular TPC design.

Figures 7.18 and 7.19 demonstrate the properties of hits as a function of distance from the nearest TPC edge. It appears more hits are found as charge is collected near a gap but the charge of these hits do not differ significantly. This may be interpreted as hits arriving at a slightly later time near the APA gaps after drifting towards the nearest wire to the gap from a more gap-centred position. One may expect to observe this in the data as a smearing in the tick direction where charge is deposited over more time, leading to a small gradient change. Although not as noticeable as anticipated, this effect is observable in the event display shown in Figure 7.20.

## 7.4 APA-Crossing Muons

The 35 ton is the only proposed experiment before the full DUNE far detector modules that have fully implemented anode planes within the cryostat reading out data from multiple drift regions simultaneously (ProtoDUNE will have wrapped wire APAs but will only read out one drift region each and SBND has the CPAs in the centre of the cryostat with the APAs at the edges). Referring to Figure 3.10, this is a design consideration that features prominently in the eventual detector so any implications in the data must be well understood. Analysis of tracks which pass through the APAs and deposit charge in both drift regions is the subject of this section.

In Section 7.4.1, a method to determine the absolute event time,  $T_0$ , from APA-crossing tracks is presented and in Section 7.4.2 the charge deposited by these tracks, particularly when crossing through the planes, is studied. Comparisons between the two drift regions, made possible by comparing tracks left by the same particle, are contained in Section 7.4.3.

### 7.4.1 $T_0$ Determination from APA Crossing Tracks

Given the nature of a TPC detector, an ‘event time’ ( $T_0$ ) must be known in order to set an absolute timescale, and therefore absolute position, on all interactions within the detector. An accurate  $T_0$  is essential for calorimetric reconstruction: in order to understand how much charge a hit had when it was created, a lifetime correction dependent on the total drift time must be applied. An incorrect  $T_0$  would lead to a systematic under- or over-estimation of

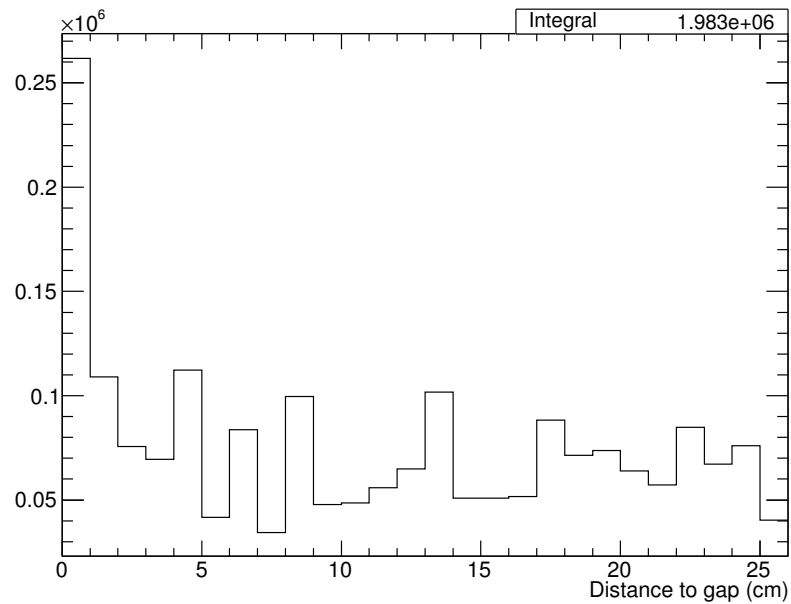


Fig. 7.18 Number of reconstructed hits at different distances from nearest APA gap.

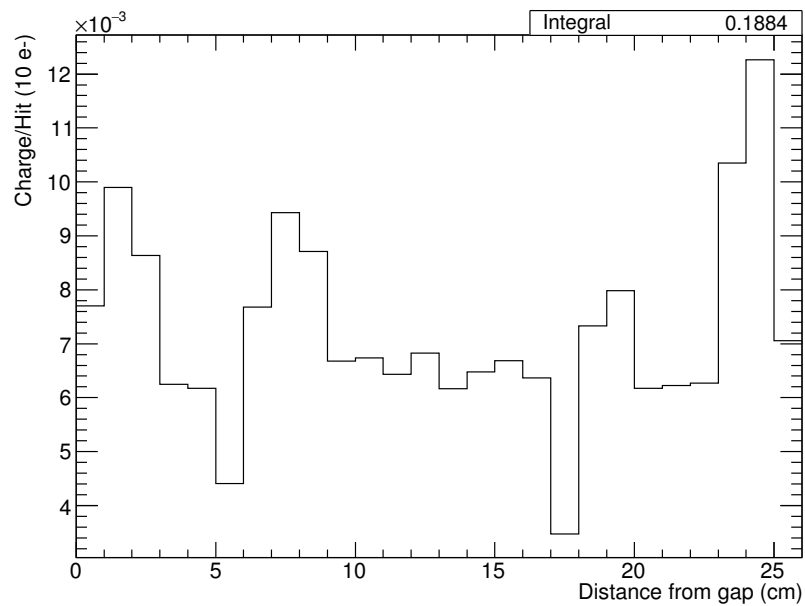


Fig. 7.19 The average charge of hits as a function of distance to nearest APA gap.

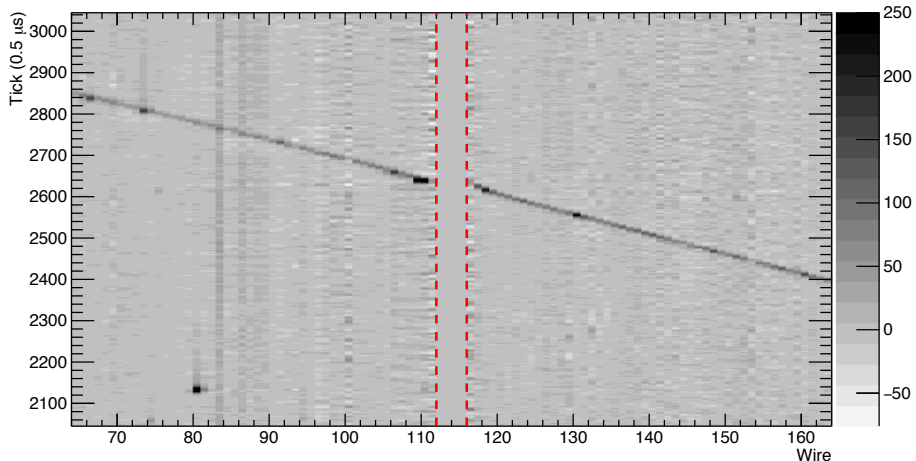


Fig. 7.20 Event display of an APA gap-crossing track, focussed on the gap region. Charge arriving at the centre of a gap deflects toward the nearest wire and is collected at a slightly later time. This results in more charge being deposited on wires nearest the gap, with a larger spread in time. This is subtly observable in the charge distributions shown here.

the reconstructed energy and have implications in particle identification and shower energy determination.

In a LArTPC, an event time is usually given by an external triggering system. The DUNE far detector will rely on the instantaneous detection of photons produced from the immediate recombination of the ionisation electrons with positive Ar ions. In the 35 ton, an additional external system was provided by the scintillation counters. Since the sample of APA-crossing muons used in this analysis were all selected and reconstructed using counter information, an interaction time is immediately known.

Without correctly accounting for T0, the tracks on each side of the APAs appear offset from the planes. This is evident from the event display shown in Figure 7.6. By aligning the track segments on either side of the APAs, a measurement of T0 can be made directly from the TPC data.

#### 7.4.1.1 Aligning APA Crossing Tracks

Two complementary methods were used to accurately align the track segments across the APA. Both involved initially correcting for the counter T0,  $T_0^{\text{counter}}$ , before considering a range of alternative T0 hypotheses and minimising a relevant metric to determine the most likely value. In the first method, demonstrated in Figure 7.21, a least square linear fit is applied to the track and the residual minimised (the ‘residual method’). The second method, demonstrated in Figure 7.22, involves fitting a line to each segment in turn and minimising the projected distance between the intersections of the lines with the centre of the APAs

( $x = 0$ ) (the ‘separation point method’). As will be shown, and can be seen from Figs. 7.21b and 7.22b, the two methods agree very well with each other.

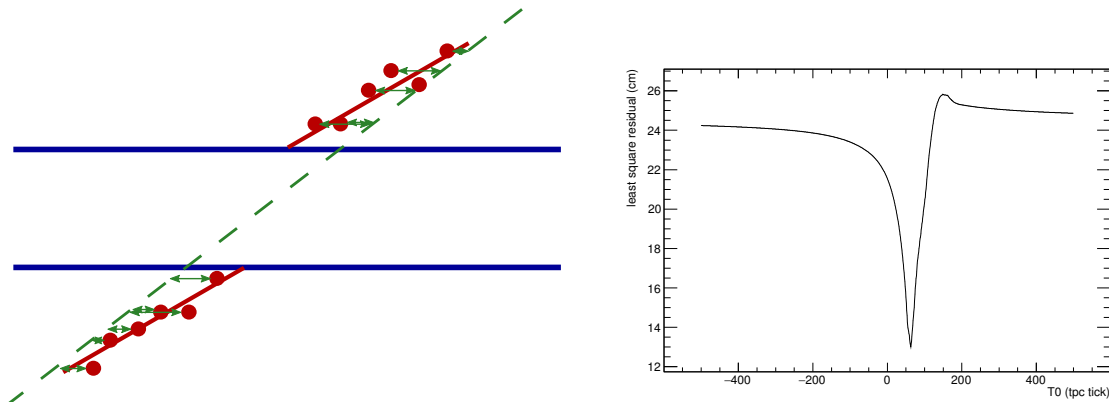
Naively, one would expect the T0 determined using these methods,  $T_0^{\text{TPC}}$ , to agree with  $T_0^{\text{counter}}$ . This is confirmed by applying the analysis to simulated data and demonstrated in Figure 7.23a. However, there appears to be a systematic offset between the T0 given by the counters and measured from the TPC data. The distribution of this discrepancy is shown in Figures 7.23b and 7.23c for each of the two methods described; it peaks around 61 ticks ( $30.5 \mu\text{s}$ ) and is importantly incompatible with zero. This suggests an inconsistency somewhere in the data taking and attempts to understand this track misalignment will be the subject of the remainder of this section. Figure 7.24 shows an example track before and after this disparity is corrected for. As is evident from Figure 7.23, the separation point method provides more consistent results so this will be used exclusively for alignment measurements in the rest of this section.

#### 7.4.1.2 Understanding the Misalignment of APA-Crossing Tracks

The underlying issue described above is essentially a misalignment of the same particle track between the two drift regions, demonstrated plainly in Figure 7.25. This obviously is not physical and stems from an issue with the detector or data readout. The most obvious cause is a miscalibration of the DAQ timing systems for the separate detector components, as previously assumed. There are however other possible solutions to the problem and it is likely the effect arises from a combination of different factors.

**Geometry** Apart from timing, a misunderstanding of the geometry could explain this perceived misalignment. The spacing between the collection planes is one such example, as demonstrated in Figure 7.26a; the spacing necessary to explain this effect, determined by aligning the tracks using the methods discussed above over a range of collection plane spacing hypotheses, is demonstrated in Figure 7.26b. As is evident from the figure, the collection planes must be repositioned in such a way that they would be reversed; the track alignment complications cannot be explained solely by this.

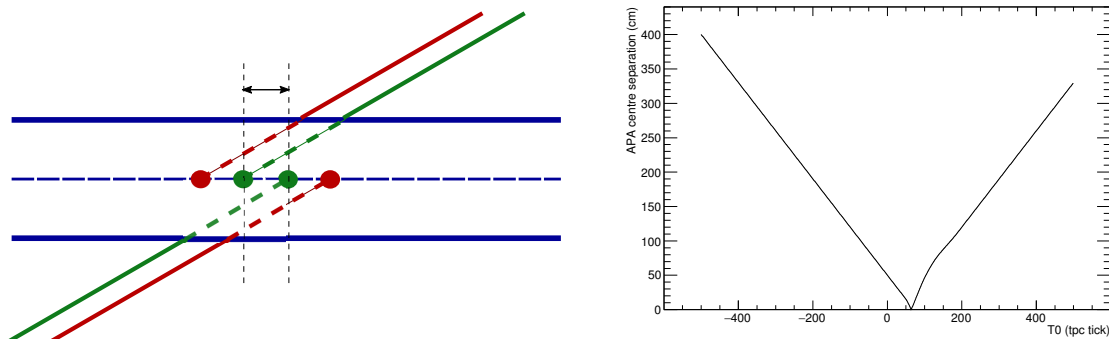
A further problem is related to the wire positioning on the APAs in the  $z$ -direction; it is understood there may be a discrepancy between the two sides of the APA resulting in hits from the long and short drift regions at the same  $z$ -position reconstructed with a systematic offset. Figure 7.27a shows how this could be utilised to explain the apparent track misalignment with Figure 7.27b showing the distribution of corrected  $z$  positions necessary to resolve the issue. Offsets of  $\sim 2 \text{ cm}$ , as suggested by these results, are highly unlikely



(a) Demonstration of the calculation of residuals from a linear fit through all hits. The red points are hits and the green line represents a linear fit through all points on both sides of the APA.

(b) The residuals to the linear fit of the track over a range of  $T_0$  candidates. The value of  $T_0$  which minimises this distribution (62 ticks in this case) is considered the most likely interaction time.

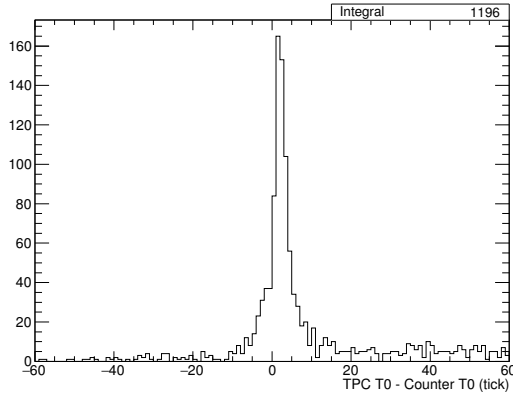
Fig. 7.21 Method to align track segments on either side of the APAs involving minimising residuals from a linear least square fit. A fit is applied to all hits and the resulting residual, a representation of the ‘goodness of fit’, is minimised over a range of  $T_0$  candidates to find the most likely interaction time for the particle leaving the track.



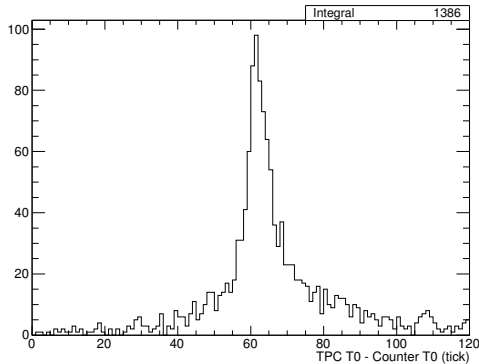
(a) Demonstration of the determination of the distance between the track segments at the centre of the APAs. The red and green lines represent linear fits to the hits (applied separately on each side of the APA) for different values of  $T_0$ .

(b) The separation distance over a range of  $T_0$  candidates. The value of  $T_0$  which minimises this distribution (63 ticks in this case) is considered the most likely interaction time.

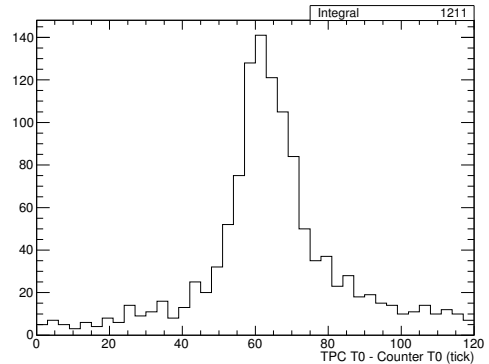
Fig. 7.22 Method to align track segments on either side of the APAs involving minimising the distance between the projected intersection of each with the centre of the APAs. A fit is applied to each track segment separately and the distance between the intersection of these lines with the centre of the APA is minimised over a range of  $T_0$  candidates to find the most likely interaction time for the particle leaving the track.



(a) 35 ton simulation. The difference in the two measurements of  $T_0$  is distributed around zero, as expected, and validates the method. The peak is actually at 1 tick, indicating a slight systematic offset.



(b) 35 ton data using the separation point method.



(c) 35 ton data using the residual method.

Fig. 7.23 Difference between the  $T_0$  calculated from TPC data and the  $T_0$  provided by the counters representing the trigger time of the through-going muon, for simulation (Figure 7.23a) and data (Figures 7.23b and 7.23c). If the two measurements of  $T_0$  agree the distribution would peak around zero, confirmed in simulation; the fact this is not the case for data is indicative of a systematic offset somewhere in the data taking.

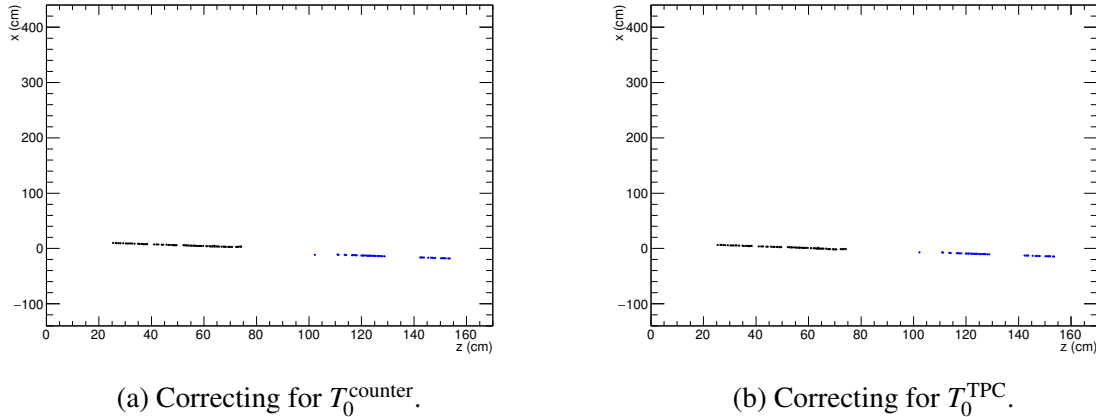


Fig. 7.24 Correcting for  $T_0$  using  $T_0^{\text{counter}}$  (Figure 7.24a) and  $T_0^{\text{TPC}}$  (Figure 7.24b). The difference is subtle but noticeable; the method for determining  $T_0$  directly from the TPC data can be validated by eye. The minimisation of the metrics to determine  $T_0^{\text{TPC}}$  in this case are demonstrated in Figs. 7.21b and 7.22b.

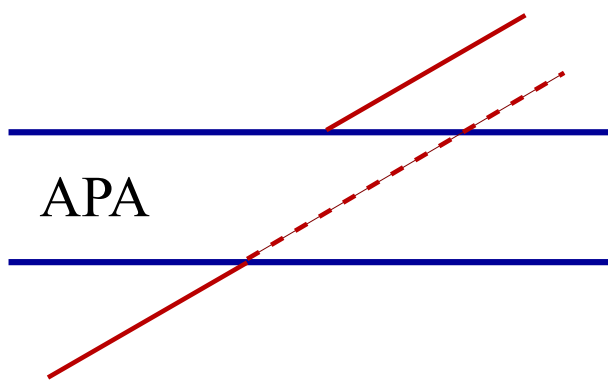
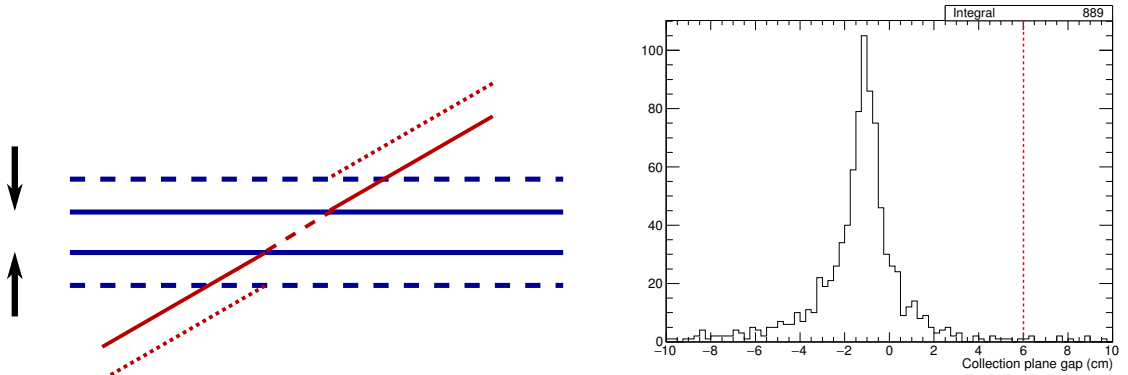


Fig. 7.25 Possibly unnecessary, but helps to explain all the various factors which could explain the offset. Can remake if necessary. Demonstration of the effect observed in the 35 ton data concerning tracks crossing the APAs. Even after correcting for the  $T_0$  provided by the counters, there is still a misalignment of the track segments across the APA frames.



(a) Demonstration of how the track misalignment could be explained by an incorrect collection plane spacing.

(b) Corrected spacing between the collection planes after considering a range of values and aligning the track segments. The red line shows the spacing used in the geometry. The distribution peaks at  $-1.19 \pm 0.05$  cm.

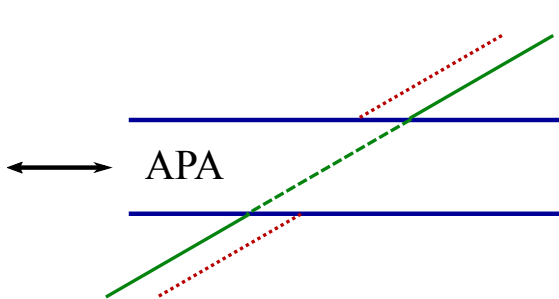
Fig. 7.26 Attemping to correct the track segment misalignment by assuming a misunderstanding of the spacing between the collection planes. It appears the resulting spacing necessary to correct for this issue would involve physically reversing the order of the planes.

given the scale of offsets identified in Section 7.3.1.2, indicating again the track alignment problem cannot be resolved in this way.

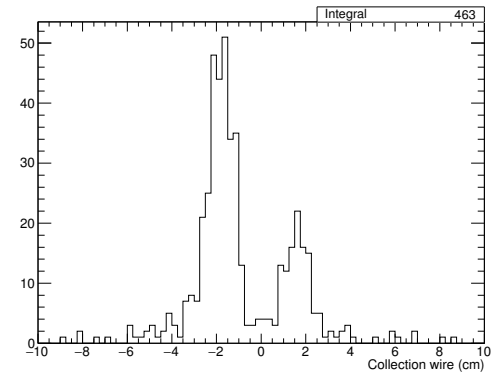
**Drift velocity** The drift velocity affects the angle of the tracks in wire/time space; a high velocity would result in a refraction-like effect towards the APA planes. As demonstrated in Figure 7.28a, this could explain the track segment misalignment if the effect was large enough. Figure 7.28b shows the necessary drift velocity required to account for the disparity observed in data; compared to a nominal value of 109 cm/ms, the scale of the change required to explain the oddity is unreasonably large, around a factor of five.

This can be tested by measuring the drift velocity directly from the data. Taking tracks which pass through opposite counter pairs and comparing this drift distance with drift time is a trivial exercise, demonstrated in Figure. 7.29. The measured value of  $110.2 \pm 0.4$  cm/ms agrees very well with the aformentioned value, determined theoretically, of 109 cm/ms. It may therefore be assumed the drift velocity is as expected and does not contribute at all to the track alignment anomoly.

**Timing** The timing offset calculated in Section. 7.4.1.1,  $32 \mu\text{s}$ , is so large it was assumed another explanation for the track segment misalignment was likely. However, after reviewing all possibilities it appears there must be a significant timing offset present somewhere in the

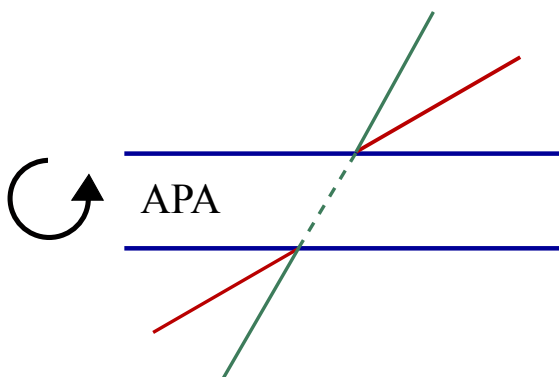


(a) Demonstration of how the track misalignment could be explained by an offset in the wire  $z$ -position on either side of the APA.

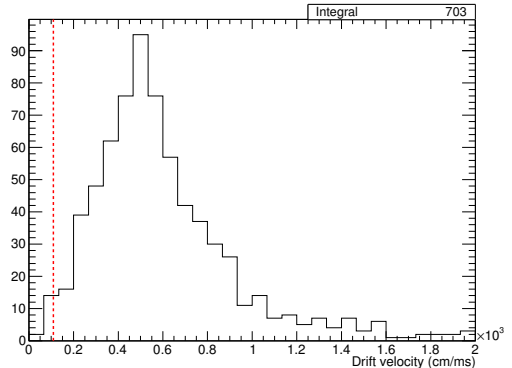


(b) Corrected  $z$ -positions of the APA wires after considering a range of values and aligning the track segments.

Fig. 7.27 Attempting to correct the track segment misalignment by assuming a misunderstanding of the positioning of the collection wires inside the detector. The wire offset would have to be around 2 cm to fix this issue.

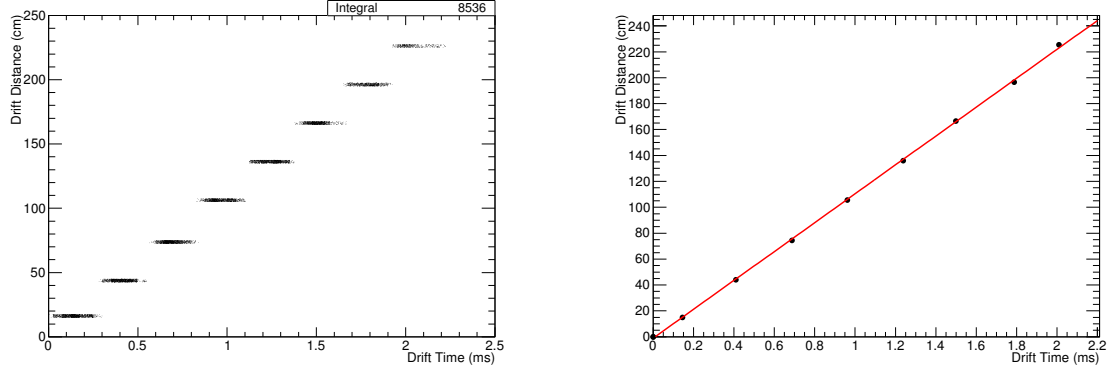


(a) Demonstration of how the track misalignment could be explained by an incorrect drift velocity.



(b) Corrected drift velocity required to align the track across the APAs. The red line shows the assumed value of 109 cm/ms.

Fig. 7.28 Attempting to correct the track segment misalignment by assuming an incorrect drift velocity. In order to account for the effect noted in the data the drift velocity would have to around five times larger than that initially calculated from models.



(a) Distribution of hit drift times for eight sets of counter pairs, assuming all tracks pass through the centres of the counters.

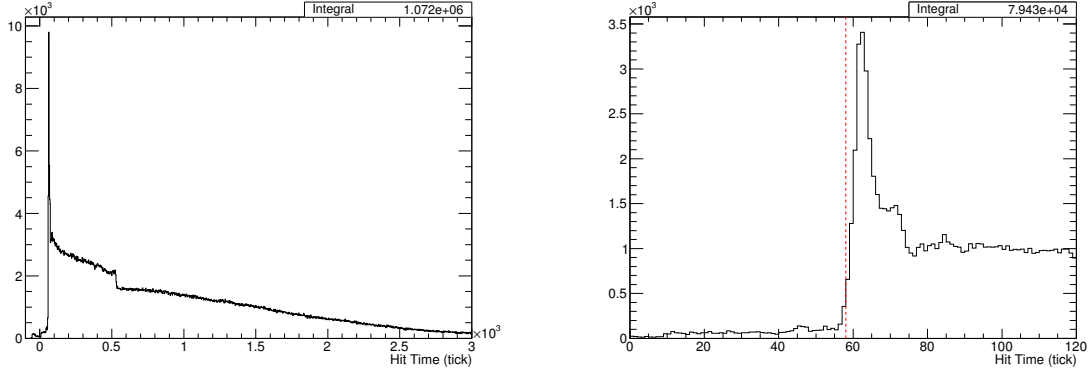
(b) The eight points found from taking the Gaussian mean of the time distributions for each rough drift distance.

Fig. 7.29 Measuring the drift velocity of the ionisation electrons by taking tracks passing through opposite counter pairs and comparing the corresponding drift distance to the drift time. Assuming all tracks pass through the geometric centres of the counters, a poor assumption, a distribution of hit time for this drift distance can be found; this is shown in 7.29a. Taking each counter pair separately and fitting a Gaussian to the distribution of drift times nullifies the assumptions necessary due to a lack of exact knowledge, on a track by track basis, of the exact  $x$ -position. This is shown in the graph in Figure 7.29b.

data. Further evidence for this hypothesis is presented in Figure 7.30 which displays the T0-corrected time distribution for all hits on the APA-crossing track. The minimum drift time these hits may have, since they pass directly through the planes, is the interaction time, T0. As is evident from the distribution in Figure 7.30b, this is around 58 ticks (29  $\mu$ s) and is notably inconsistent with zero. The curious spike at the interaction time motivates the work presented in Section 7.4.2 and will be discussed there. Additionally, it is possible to compare the T0 provided by the counters with information from the photon detectors. This is shown in Figure 7.31 and provides further confirmation for a timing miscalibration in the TPC readout.

This interesting result provoked further investigation into the notion of a timing offset between detector components, specifically the TPC and counter readout (RCEs and PTB respectively). Confirmation of this miscalibration is displayed in Figure 7.32 which shows the difference between the timestamps recorded by each of the subcomponents upon receiving the trigger.

There are now three measurements of the timing offset with a slight disagreement between each. This will be discussed further in Section 7.4.1.3.



(a) Over the full range of drift times. The sharp dip around 500 ticks corresponds to the maximum drift time for hits in the short drift region; beyond this only hits in the long drift region contributes to the distribution.

(b) Zoomed in on the interaction time. The red line is drawn at 58 ticks ( $29 \mu\text{s}$ ) and represents, by eye, the start of the distribution.

Fig. 7.30 The T0-corrected drift time for hits on APA-crossing tracks. The lower leading edge of this distribution is an indication of the interaction time, T0.

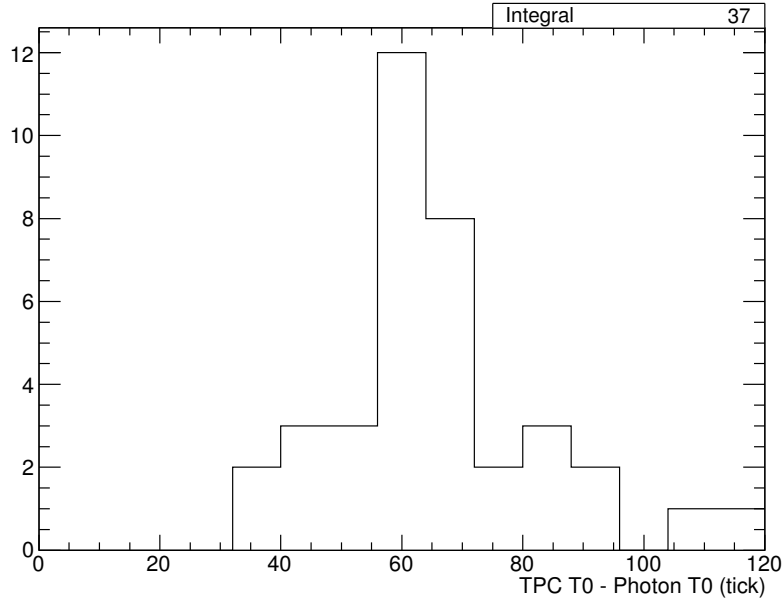


Fig. 7.31 Difference between the interaction time measured by the TPC data and that provided by photon detector information. Only events with a single reconstructed flash are considered, with each assumed to have been caused by the triggering particle. This results in very few events, but clear supporting evidence of a timing offset on the order of 60 ticks is found.

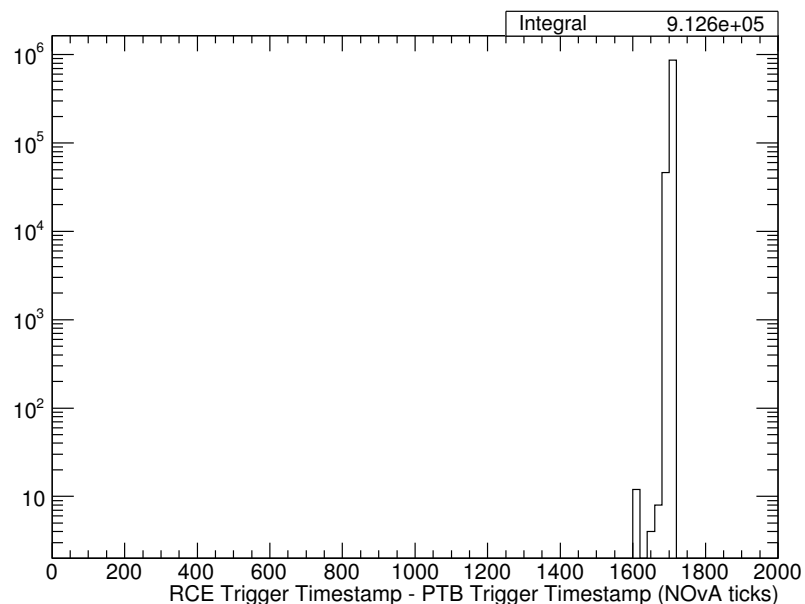


Fig. 7.32 The difference between the timestamps recorded by the PTB and the RCEs upon receiving a trigger. The absolute timing for the DAQ system is given, along with most experiments at FNAL, by ‘NOvA time’: a 64 MHz clock starting on 1st January, 2010 (with one NOvA tick therefore being 15.625 ns). The distribution peaks sharply at 1705 NOvA ticks, or 26.6  $\mu$ s.

### 7.4.1.3 Combined Offset Analysis

The discussion in Section 7.4.1.2 hints strongly at an intrinsic timing offset present in the data. However, as already shown in Section 7.3, it is understood there are geometrical offsets in the positions of the APAs in the  $x$ - and  $z$ -dimensions. Attempting to measure all these offsets simultaneously presents challenges since they all affect each other. It is possible the tension between the measurements of the timing offset may be resolved by combining the results from each of the offset calculations.

The timing offset will not influence the determination of the geometrical APA gaps (found in Section 7.3) unless the track segments used to measure the gaps cross through the APA frames; the timing is consistent for each drift region. A simple cut was used to exclude such events when making these measurements. However, the geometrical offsets will have an impact on the APA crossover analysis. For example, the drift times measured for each hit will be affected by the physical positions of the APAs. Figure 7.33 shows the distribution of the drift times for all track hits corrected for the offsets implied by the  $x$ -gap measurements. It can be seen this accounts for the disparity between the previous measurements. It does not appear to agree completely with the offsets found between the timestamps but serves to demonstrate differences from the assumed positions of the APAs have a very sizeable effect on distributions such as these.

Correcting for this timing offset, along with those in the  $x$ - and  $z$ -positions of the APAs, does not entirely account for the initial inconsistency observed in Figure 7.23. A similar evaluation to that undertaken in Section 7.4.1.2, namely considering the required disparities in various quantities to account for this, may be used to facilitate a complete understanding. After correcting for the three aforementioned offsets, Figure 7.34 demonstrates the necessary misunderstandings in the collection plane spacing and the  $z$ -positions of the collection wires to account for the remaining discrepancy. It seems highly likely that the offsets between the APA gaps left unresolved in the short drift region, incalculable in the 35 ton data, can account for the outstanding misalignment between the track segments. Nothing conclusive can be extracted from Figure 7.34b with regards to the values of these uncertainties since this considers differences between all short drift region TPCs and long drift region TPCs together but implies further offsets at a similar scale to those measured in the long drift region may still be present. With corrected APA gaps in the short drift region, it is reasonable to argue the track segment misalignment between drift regions would be completely resolved.

This is the first time tracks crossing the readout planes have been used in a LArTPC experiment and have proven to be a valuable way of calibrating inter-detector components and finding other inconsistencies in the data. Without studying this data set, the timing offset between the TPC and the external counters would not have been discovered and all

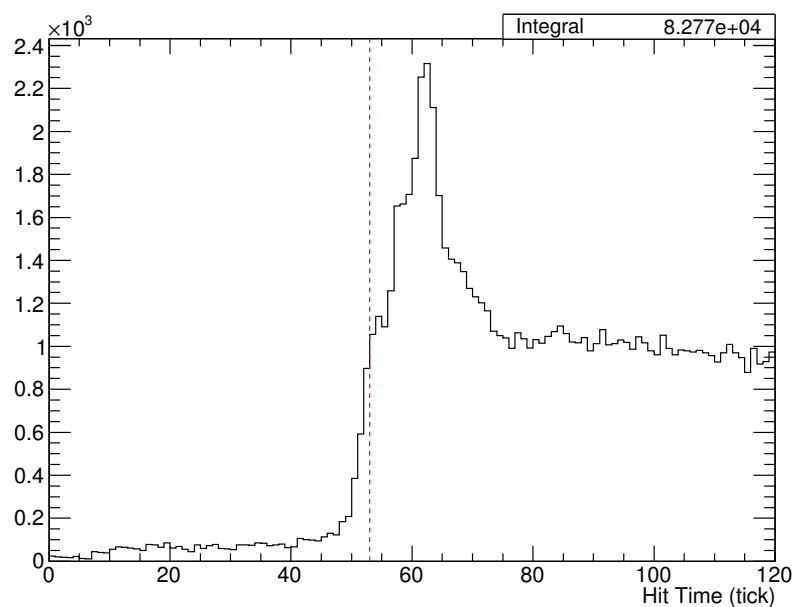
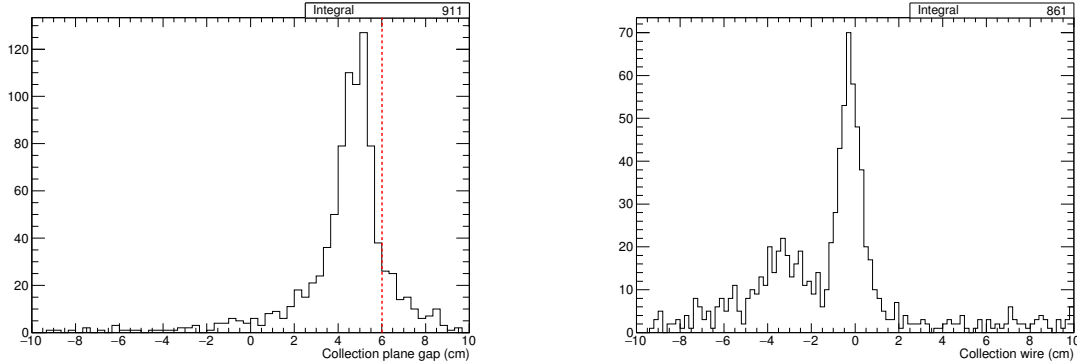


Fig. 7.33 The distribution of the drift times of all hits on APA-crossing tracks after correcting for the APA offsets along the direction parallel to the drift direction, found in Section 7.3. The red line represents a T0 of 53 ticks, representing the difference observed between the trigger timestamps between the scintillation counter and TPC readout systems. The hit time distribution appears to agree with this value to a greater extent than previously (Figure 7.30b).



(a) Assuming a misunderstanding in the spacing between the collection planes, a value of  $4.74 \pm 0.04$  cm is measured. This is a difference of  $1.27 \pm 0.04$  cm from the assumed spacing, a discrepancy which is highly unlikely.

(b) Assuming a misunderstanding in the alignment of the collection planes in  $z$  between the two drift regions, an offset of  $-0.24 \pm 0.03$  cm is found. Given the scale of the corrections determined in Section 7.3.1.2, and the incapability to measure the gaps in the short drift regions, this is emminently credible.

Fig. 7.34 Accounting for the extra discrepancy in track alignment after fixing for all the measured offsets by assuming a misunderstanding in the collection plane spacing (Figure 7.34a) and the  $z$ -positions of the collection wires (Figure 7.34b).

analyses would naively use the incorrect  $T_0$ . The experience in characterising the offsets in the 35 ton, in time,  $x$  and  $z$ , will be crucial when understanding the eventual DUNE far detector. Based on experience here, it is imperative these misunderstandings are mitigated as much as possible at the far detectors, with each module containing 150 APAs and four drift regions.

## 7.4.2 Charge Deposited by APA Crossing Tracks

The intriguing distribution of the  $T_0$ -corrected hit times observed in the data, shown in Figure 7.30a, hints at some aspect of the detector response that needs to be understood. In the DUNE far detector, a large number of events will contain particles which pass through the APA frames so characterising resulting effects is critical. The equivalent plot for simulated data is shown in Figure 7.35. Comparing these distributions, there is a very obvious difference around the interaction time. It appears there is an effect present in the data, not currently being simulated, which manifests in around twice the amount of hits occurring at  $T_0$  on the collection planes for APA-crossing tracks. This is described in Section 7.4.2.1 and the phenomenon is visible on event displays presented in Section 7.4.2.2.

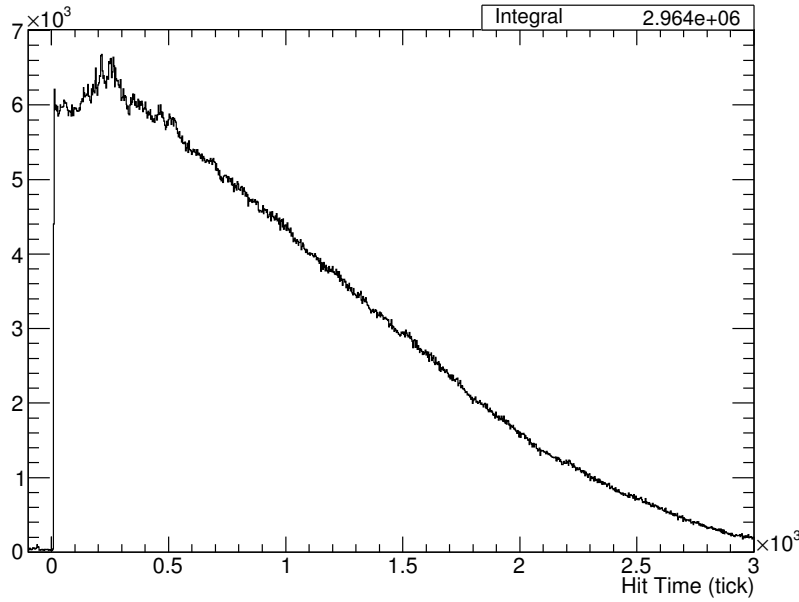


Fig. 7.35 The T0-corrected drift time for all hits on an APA-crossing track in simulation. The equivalent plot for 35 ton data is shown in Figure 7.30a.

#### 7.4.2.1 Interaction Time Hits

The excess of hits at the interaction time is due to the use of a grounded ‘mesh’ at the centre of the APAs. The purpose of such a design choice is to ensure a uniform electric field across the face of the APA; without it the field would be ill-defined given the presence of the grounded, rectangular APA frames with positively biased planes on either side. It is plausible therefore to consider a ‘backward-facing’ field being set up between the grounded mesh and the positively biased collection planes which would lead to hits drifting the ‘wrong’ way when produced in this region; APA-crossing tracks would hence leave twice as many hits on the collection plane as the other planes. This is demonstrated schematically in Figure 7.36.

A convenient way of confirming whether or not the mesh can explain this excess of hits at the interaction time is possible since one of the four APAs in the 35 ton was constructed without the mesh, precisely for this purpose. Unfortunately, this was the APA which was more plagued by noise issues so very little good data is available from channels on this APAs. It is however possible to make a crude comparison; this is shown in Figure 7.37. The appears to confirm the shark peak of hits occurring at the interaction time comes from the APAs which use a mesh.

Using the 35 ton dataset, it is also possible to confirm that the mesh is functioning as expected. Without a mesh, one may expect a difference between the hits deposited on wires

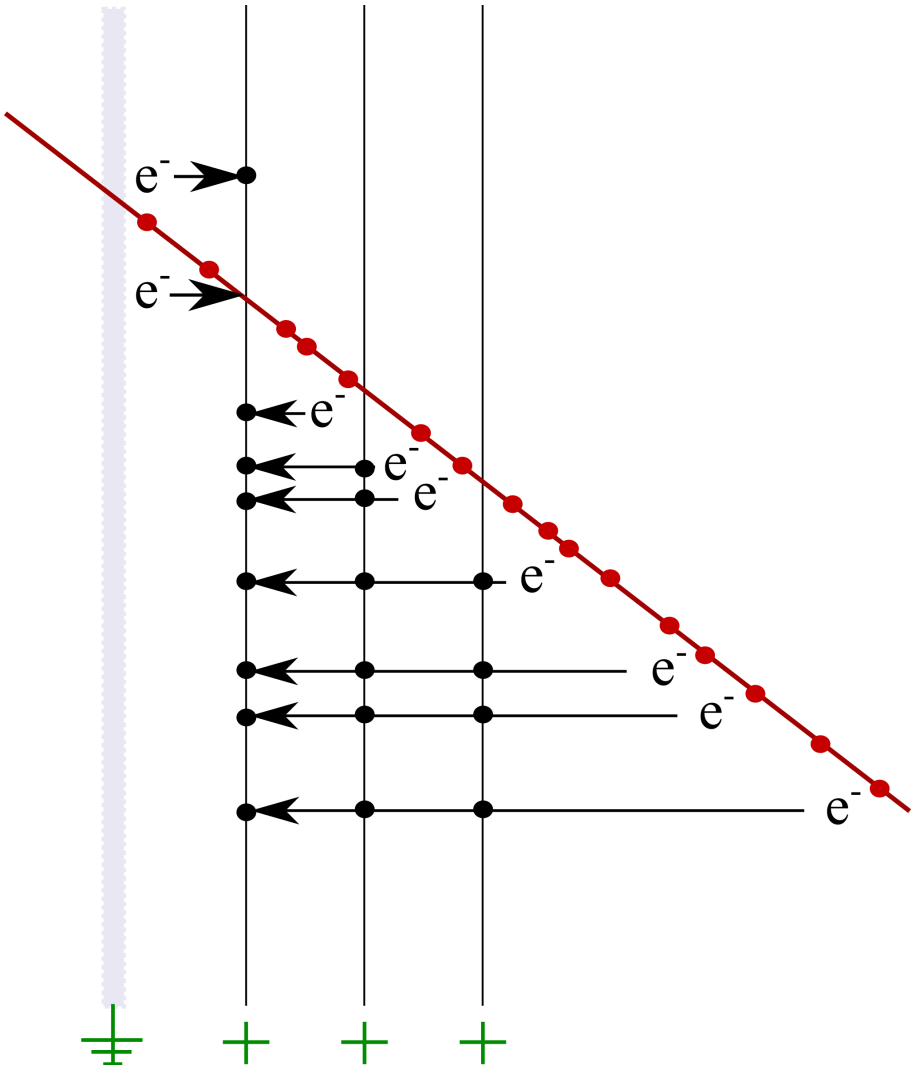
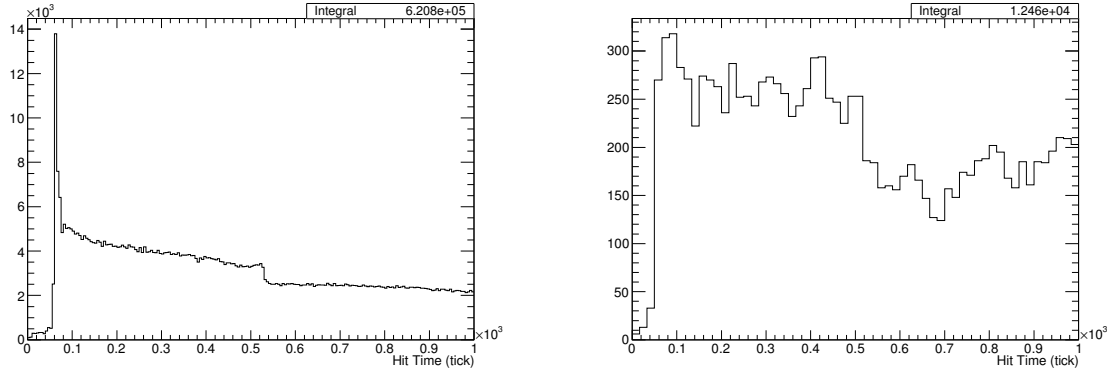


Fig. 7.36 Demonstration of the ionisation and hit collection for APA-crossing tracks. The red line represents a track passing through the anode planes, shown in black. The grey region is the centre of the APA frame on which the grounded mesh is afixed. The red dots correspond to the ionisation of electrons which then drift, depositing charge (black dots) on the readout wires. The three planes shown are, from left to right, the collection plane and the two induction planes. The biasing of each of the planes and mesh sets up field lines which all terminate on the collection wires, resulting in charge collected from before the track passes through and after.



(a) Hit times for all hits on APAs 0, 2 and 3; these are the three APAs containing the grounded mesh at the centre.

(b) Hit times for all hits on APA 1, the APA without a grounded mesh at its centre.

Fig. 7.37 Comparison between the T0-corrected hit time distributions on APAs with and without the grounded mesh. Even given the very low stats in Figure 7.37b, there is a noticeable difference in the distribution of hits around the interaction time.

towards the centre of an APA face and wires at the edges, in front of the grounded frame. The functionality of the grounded mesh ensures there is no difference between any wires on a given APA. Figure 7.38 confirms this is the case.

A natural question to pose at this point is to ask if these ‘extra’ hits deposited by APA-crossing tracks as a result of this ‘backwards’ field have similar properties to the ‘correct’ hits. The most important property to consider is the charge of the hits; Figure 7.39 shows the average charge per hit for hits occurring at the interaction time and all other hits. It is clear from this there is nothing different about these additional hits and they can be treated in the same way.

As alluded to earlier, the DUNE simulation software is simplistic and does not simulate any ionisations within the region of the APA planes; in the case of APA-crossing muons this results in no hits being created after the track passes through the first induction wires. Evidently, this is an important region and must be understood and well simulated in order to test reconstruction and analyses. When this is added to the software, the 35 ton data will be essential for validation purposes.

#### 7.4.2.2 Event Displays of APA-Crossing Tracks

The effect investigated in Section 7.4.2.1 is directly observable in the raw data, as shown in Figure 7.40. The electrons ionised as the particle track passes between the collection

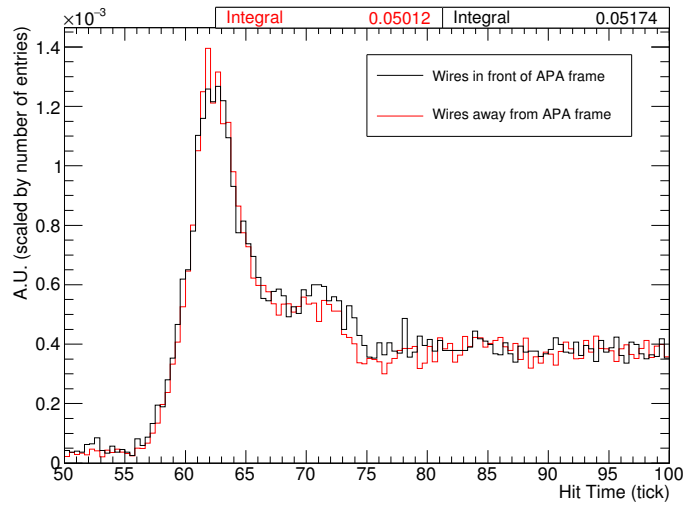
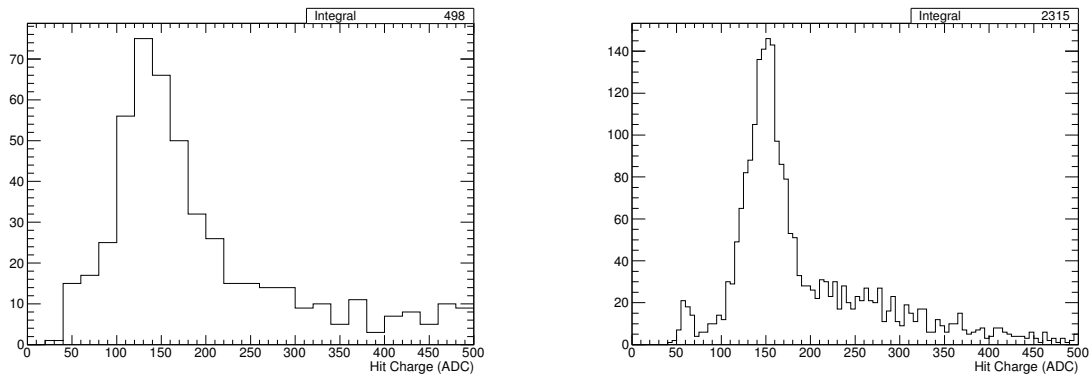


Fig. 7.38 Comparison between the distribution of T0-corrected hit times for hits on wires in front of the APA frame and away from the APA frame to validate the functionality of the mesh. Both distributions are normalised by the number of entries. There is no evidence of any differences between the two distributions so this suggests the mesh is working as intended.



(a) Hits occurring around the interaction time;  $50 < \text{tick} < 70$ . A fitted Gaussian of the peak yields a mean of 149 and width of 49.

(b) Hits occurring away from the interaction time;  $\text{tick} < 50, \text{tick} > 70$ . A fitted Gaussian of the peak yields a mean of 152 and a width of 28.

Fig. 7.39 Average lifetime-corrected charge per hit for hits on an APA-crossing track separated according to whether or not the hit was collected around the interaction time. There is no evidence to suggest the ‘extra’ hits collected around the interaction time have significantly more or less average charge than ‘regular’ hits.

plane and the mesh are observable as hits which appear to have drifted in the negative time direction. The outcome is a little ‘hook’ shape in the data.

### 7.4.3 Comparing Drift Regions with APA-Crossing Tracks

APA-crossing tracks may be utilised to make unique, specific measurements of the detector made possible since they originate from the same particle. For example, any drift velocity differences between the drift regions may be observed and the noise levels on the collection readouts on either side of the APA can be studied and compared.

The drift velocity is given by the angle of the track in wire/time space and any difference between this velocity in the two drift regions would be noticeable in a refraction-like effect. This is demonstrated in Figure 7.41a. A measure of the angle between the track segments in the different regions would therefore be a measure of the change in drift velocity; this is shown in Figure 7.41b.

The relative noise on the two collection planes can be evaluated by considering the number of hits present in the counter shadow, in each drift region, which were not reconstructed as part of the track associated with the triggering particle. The difference between each collection plane for a given event should peak at zero if similar levels of noise were observed in each drift region; this is confirmed in Figure 7.42.

## 7.5 Shower Reconstruction in 35 ton Data

The developments to the reconstruction in LArSoft, discussed in Chapter 5, were originally motivated by an interest in reconstructing and analysing  $\pi^0$  mesons in the 35 ton data. Given the unfortunate eventual problems prevalent in the data, such analyses would be extremely challenging and likely impossible. Since it is still interesting and instructive to analyse how well the reconstruction performs on a sample of real data, this will be briefly explored in the present section.

Considerations relevant when applying the reconstruction developed on simulation to data are discussed in Section 7.5.1 before the necessary reanalysis of the calorimetry is presented in Section 7.5.2. The algorithms are applied to a shower and a  $\pi^0$  candidate found in the data in Sections 7.5.3 and 7.5.4 respectively.

### 7.5.1 Data Specific Reconstruction

The BlurredCluster and EMShower algorithms, outlined in Sections 5.4.2 and 5.4.3 respectively, were applied to the data in an attempt to reconstruct particle objects. In general, the

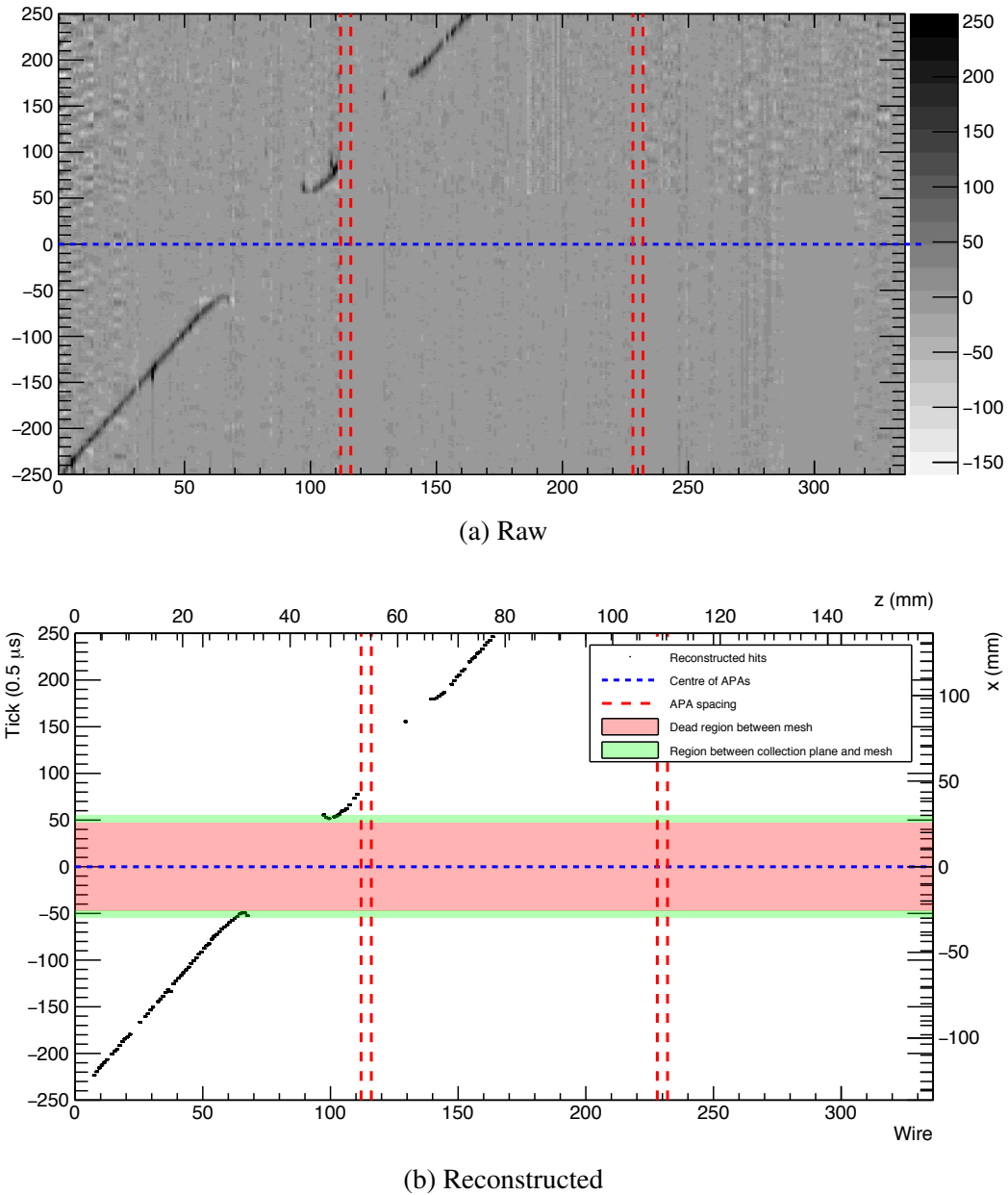
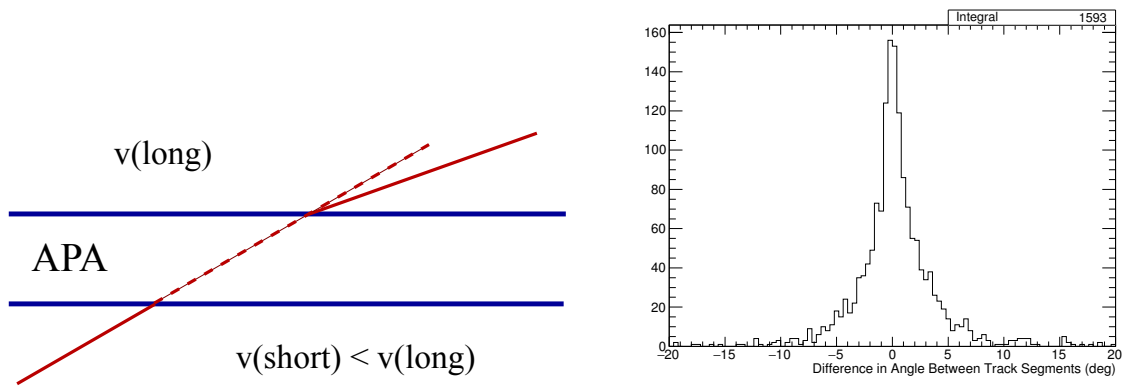


Fig. 7.40 Event display of an APA-crossing track with the charge deposited as it passes through the APAs evident. Figure 7.40a shows the raw charge and Figure 7.40b shows the reconstructed hits. The ‘hook’-like effect is visible, with hits at apparently negative drift time. The cm scale on Figure 7.40b is provided as a guide and is not completely correct due to the differing fields.



(a) Demonstration of how differing drift velocities between the drift regions would manifest in the data. A refraction-like effect would result in an angle between the two track segments.

(b) The angle between the track segments on either side of the APAs. The distribution peaks around zero, implying, as expected, the drift velocity is constant in both regions.

Fig. 7.41 Using APA-crossing tracks to confirm the drift velocity is consistent between the two drift regions.

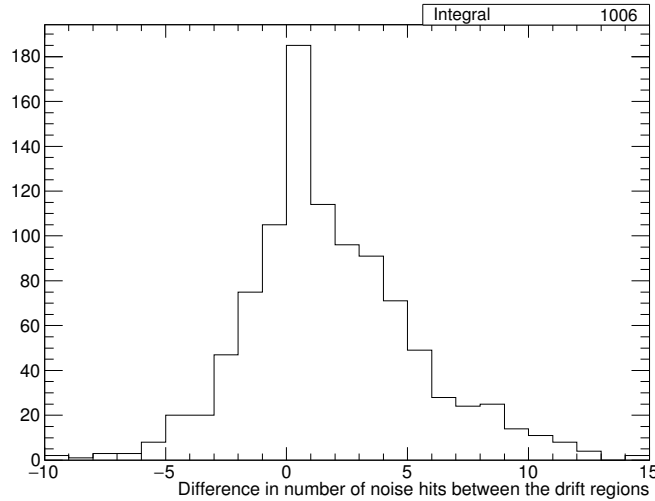


Fig. 7.42 Comparison of noise levels between the two drift regions using APA-crossing tracks. The number of noise hits in the counter shadow for each drift region was considered separately by neglecting all hits identified as track hits, all hits on noisy wires and all hits which have a large number of closely neighbouring hits (which could be symptomatic of unrelated particle tracks). The difference between the number of noise hits in each peaks around zero, implying similar levels of noise.

algorithms worked out the box and required no tuning. Since this requires real 3D reconstruction, as opposed to the subtle techniques developed to circumvent the issues with the induction planes (described in Section 7.1.3), the use of more than just the collection plane is necessitated. Reconstruction is therefore only possible for showers with large enough signals on induction planes, following the coherent noise removal, and following hit disambiguation.

As showering particles are unlikely to be associated with through-going muons, an unassociated method for obtaining the interaction time is required. In general, the photon detectors are designed for this purpose so the use of these seems natural.

Since it is highly unlikely the electronics models and detector responses used in the simulation are perfectly accurate, applying the calorimetric reconstruction to the data without modification would be inappropriate. The relevant calorimetric constants and functions must be determined from the data; this is essential for complete reconstruction and is discussed in Section 7.5.2.

### 7.5.2 Calorimetry Reconstruction

There are two relevant calorimetric conversions which are pertinent to shower reconstruction (both previously discussed in Section 5.3): the calorimetry constant and the shower energy conversion. The methods used to determine these for data will be discussed in this section.

It should be stressed that due to the large noise levels, accurate calorimetry will not be possible in the 35 ton data. This may be understood by considering the distribution of charge deposited by ionising particles; typically this is sampled from a Landau distribution with a most probable value dependent on the electron drift distance (due to lifetime effects). Since hit reconstruction tends to put cut on the hit ‘threshold’, the height of the peak above pedestal, this compromises lower energy hits populating the full charge distribution and biases the reconstruction toward higher energies. This is demonstrated in Figure 7.43. As far as possible, steps to mitigate these effects have been applied in the proceeding discussion. There will however be an inevitable bias so the following should not be treated as a full, rigorous assessment.

Calorimetric reconstruction is only attempted for the collection planes where the effects of noise are mitigated somewhat compared to the induction views. Since the data used were taken at a drift field of 250 V/cm (half the nominal voltage), the recombination factor used must take this into account. At 500 V/cm the value is 0.63 whilst at 250 V/cm a factor of 0.52 is used.

The procedure invoked to determine the calorimetry constant is largely identical to that used in simulation: the  $dE/dx$  of a through-going MIP is calculated and the constant varied until the expected distribution is obtained. The through-going muons used in the analyses

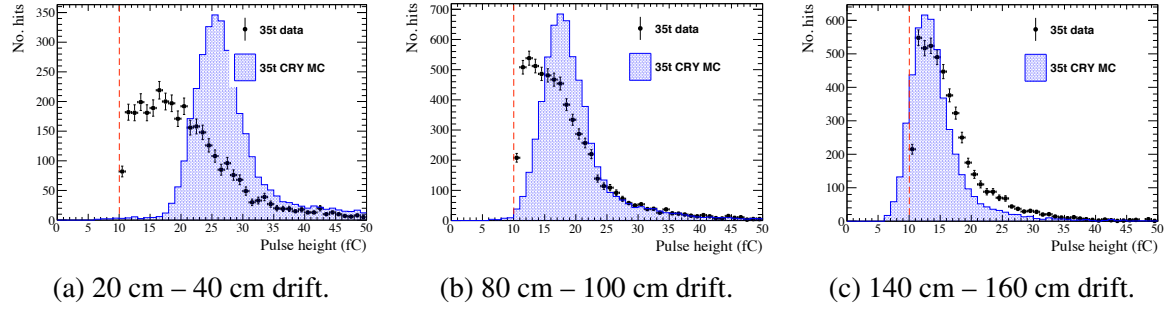


Fig. 7.43 The bias in the hit selection due to a high noise level in the 35 ton data. The charge distribution for through-going muons is shown for three different displacements along the drift direction,  $20 \text{ cm} < x < 40 \text{ cm}$ ,  $80 \text{ cm} < x < 100 \text{ cm}$  and  $140 \text{ cm} < x < 160 \text{ cm}$ . The red line represents a typical hit finding threshold. The most probable value of the distribution is close to this boundary in each of the cases, resulting in the lower charge hits being missed. This introduces a bias towards higher charge and has implications for the reliability of calorimetry in the 35 ton data sample.

described in Sections 7.4 and 7.3 were utilised to make these measurements. Additional necessary information, such as the interaction time (to correct the charge for lifetime) and the track angle (to correct the  $dE/dx$  for track pitch), is provided by the counters. In order to produce reliable results, an additional cut requiring at least 20 consecutive wires with a single hit on each was applied, with the  $dE/dx$  measurement obtained using just these hits. The eventual  $dE/dx$  distribution is demonstrated in Figure 7.44 and implies a calorimetry constant of  $7.4 \times 10^{-3}$  (for comparison, the value used for the collection plane in simulation is  $5.4 \times 10^{-3}$ ).

In simulation, truth information was used to find a general charge to energy conversion used in, for example, the determination of total shower energy. This obviously is not possible in data so a similar technique to the calculation of the calorimetry constant described above was used. The lifetime-corrected charge and track pitch information can be utilised to find a value of  $dQ/dx$  (ADC/cm), which may then be converted into a measure of  $dE/dx$  (MeV/cm) using the calorimetry constant previously determined. This may in turn be used to find the total deposited energy by taking into account the distance travelled by the associated track in the collection view. As demonstrated in Figure ??, there exists a linear relationship between total deposited lifetime-corrected charge and the particle energy; this is also seen in data in Figure 7.45. This may then be used as a conversion in shower energy reconstruction.

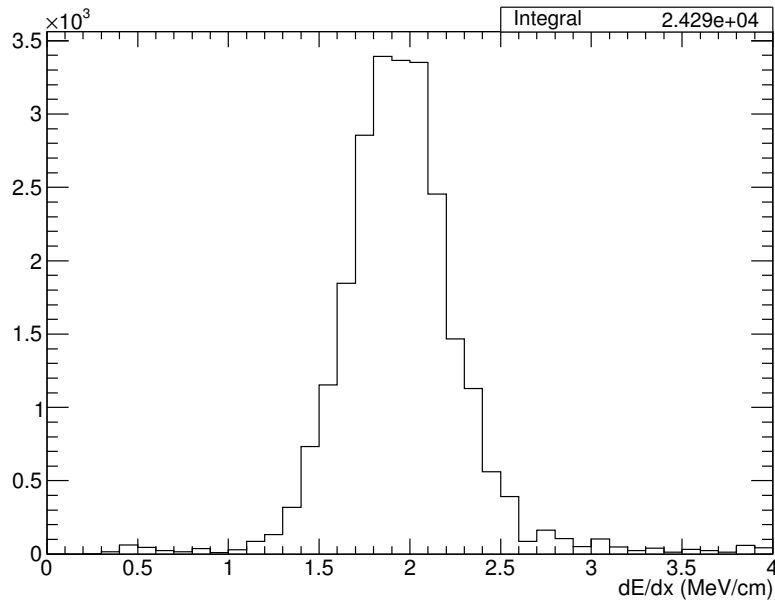


Fig. 7.44 The  $dE/dx$  distribution for MIPs passing through the 35 ton TPC. The calorimetry constant is chosen to ensure the peak of the distribution, which ideally follows a Landau, is around 1.8-1.9 MeV/cm.

### 7.5.3 Shower Reconstruction

Using the modifications discussed in Sections 7.5.1 and 7.5.2, the performance of the showering reconstruction on real data can be assessed by applying it to an electromagnetic shower. The result of applying the algorithms to the famous 35 ton shower depicted in Figure 4.27 is shown in Figure 7.46. The calorimetric reconstruction yields a  $dE/dx$  of 1.1 MeV/cm and a total shower energy of 188 MeV. These results appear feasible and are consistent with an electron shower, for which one would expect a  $dE/dx$  peaked around 2.1 MeV/cm; 1.1 MeV/cm is not an unreasonable value in the tail of this distribution. Given the electron energy, it is likely to have been produced by Compton scattering.

The T0 for this particle was determined to be 4740 ticks from reconstructing flash information collected by the photon detectors – this makes this shower the only fully automated reconstructed particle object in the 35 ton dataset.

### 7.5.4 $\pi^0$ Reconstruction

An important calorimetric test of particle detectors involves demonstrating a reasonable reconstructed  $\pi^0$  mass peak. It was for this reason that the shower reconstruction discussed in Chapter 5 was developed. An analysis of a  $\pi^0$  candidate event is briefly considered here.

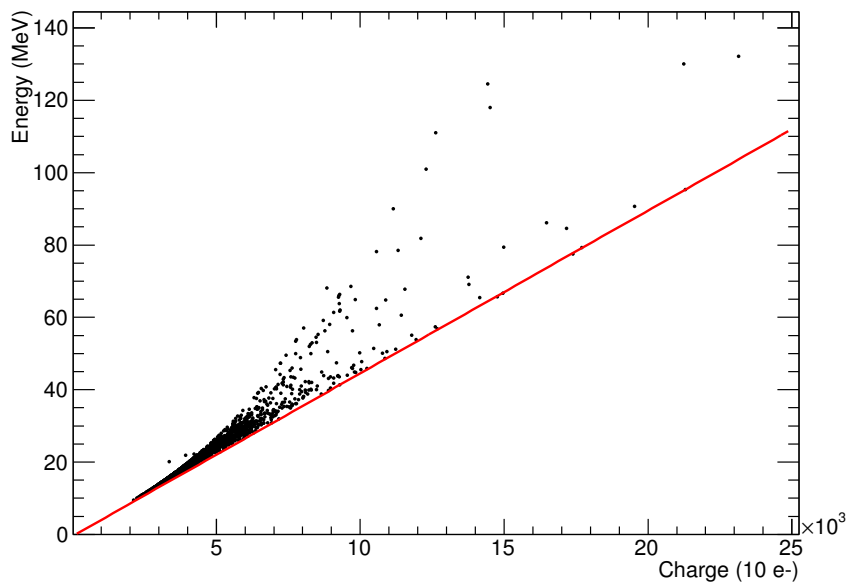


Fig. 7.45 Relationship between deposited charge and energy for 35 ton data, calculated using through-going MIPs. The lower edge of the distribution follows a linear pattern and it is this which the conversion is chosen to represent. Deviations from this linear fit observed above it are related to the fundamental issues with the 35 ton data and arise from missed charge due to the problems illustrated in Figure 7.43. This results in hits reconstructed with a lower charge for the implied energy deposited by the MIP. It should be noted there are no cases of extra charge deposited; this concurs with this interpretation and ensures confidence in the displayed line as the correct conversion may be assumed.

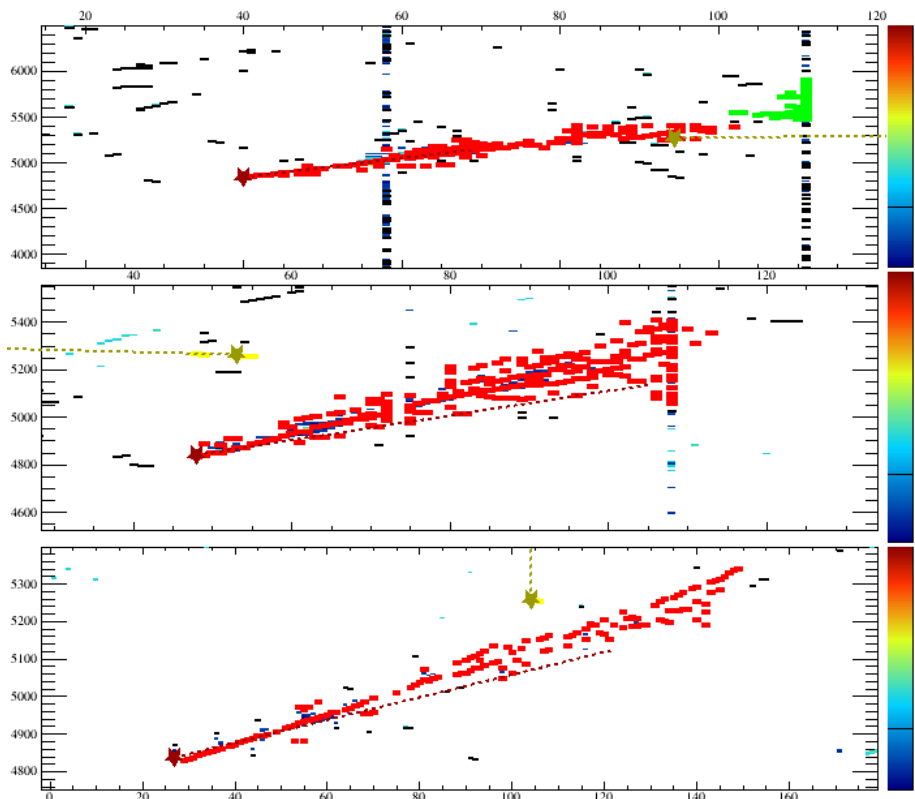


Fig. 7.46 Result of applying the shower reconstruction on a shower observed in the 35 ton data. Each small rectangle represents a reconstructed hit and the colour associated with each corresponds to a reconstructed shower object. The stars and dotted lines represent the reconstructed start point and direction for each shower.

Without full reconstruction and selection, identifying candidate events is very difficult. Such an event was observed in the online event display however and is shown in Figure 7.47. Unlike the shower discussed in Section 7.5.3, there is no associated photon detector informa-

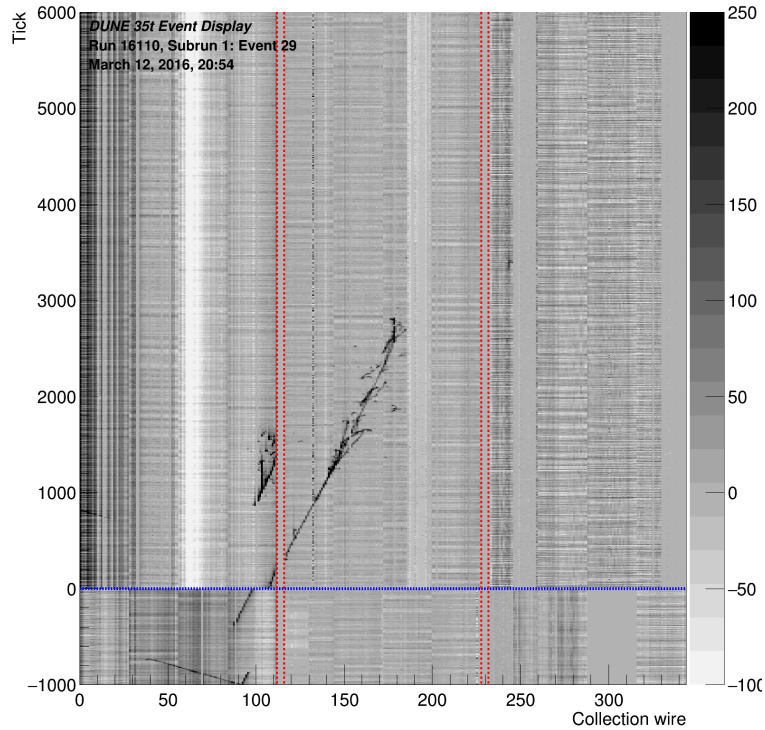


Fig. 7.47 A candidate  $\pi^0$  event observed in the online event display during the run.

tion for this event; however, one of the candidate photons passes through the APA frames so techniques developed for the APA-crosser analysis (Section 7.4) may be employed to determine the relevant interaction time. Applying the calorimetry reconstruction, the  $dE/dx$  information associated with the high energy candidate photon (the one which crosses the APAs) gives a value of 4.75 MeV/cm, entirely consistent with the expectation for a photon of a distribution centred around 4.2 MeV/cm. The low energy candidate photon travels almost completely along the collection view direction resulting in unreliable  $dE/dx$  information. The total energy for each shower is determined to be 161.8 MeV and 500.5 MeV with an implied invariant mass of

$$m_{\pi^0?} = 156.6 \text{ MeV}, \quad (7.4)$$

comparable to the true  $\pi^0$  mass of 140 MeV.

Without fully considering uncertainties and biases present, it is not possible to make a judgement as to the performance of the basic calorimetric reconstruction discussed in Section 7.5.2 or to confirm whether or not the event displayed in Figure 7.47 represents a  $\pi^0$  decay. However,  $dE/dx$  values of 1.1 MeV/cm and 4.75 MeV/cm for different showers appear consistent with electron and photon particles respectively and, within the limits of the analysis presented here, it is believable the particle with invariant reconstructed mass of 156.6 MeV is indeed a  $\pi^0$ .

## 7.6 35 ton Data Analysis Summary

Despite initial problems with the 35 ton good progress has been made in analyses, specifically focussing on understanding the detector. Techniques developed will be directly applicable to the data collected with the eventual far detector



# References

- [1] Sheldon L Glashow. Partial-symmetries of weak interactions. *Nuclear Physics*, 22(4):579–588, 1961.
- [2] Steven Weinberg. A Model of Leptons. *Phys. Rev. Lett.*, 19(21):1264–1266, 1967.
- [3] G. Aad, et al. Observation of a new particle in the search for the Standard Model Higgs boson with the ATLAS detector at the LHC. *Physics Letters B*, 716(1):1–29, 2012.
- [4] S. Chatrchyan, et al. Observation of a new boson at a mass of 125 GeV with the CMS experiment at the LHC. *Physics Letters, Section B: Nuclear, Elementary Particle and High-Energy Physics*, 716(1):30–61, 2012.
- [5] Tara Shears. The Standard Model. *Phil. Trans. Roy. Soc. Lond.*, A370:805–817, 2012.
- [6] S M Bilenky. Neutrino in standard model and beyond. *Physics of Particles and Nuclei*, 46(4):475–496, 2015.
- [7] John Ellis. Outstanding questions: Physics beyond the Standard Model. *Phil. Trans. Roy. Soc. Lond.*, A370:818–830, 2012.
- [8] Y Fukuda, et al. Evidence for Oscillation of Atmospheric Neutrinos. *Phys. Rev. Lett.*, 81(8):1562–1567, 1998.
- [9] Q R Ahmad, et al. Direct Evidence for Neutrino Flavor Transformation from Neutral-Current Interactions in the Sudbury Neutrino Observatory. *Phys. Rev. Lett.*, 89(1):11301, 2002.
- [10] Wolfgang Pauli. Open letter to the participants of the conference in Tübingen, 1930.
- [11] E Fermi. Trends to a Theory of beta Radiation. (In Italian). *Nuovo Cim.*, 11:1–19, 1934.
- [12] E Fermi. Versuch einer Theorie der  $\beta$ -Strahlen. I. *Zeitschrift für Physik*, 88(3):161–177, 1934.
- [13] F. Wilson. Fermi’s Theory of Beta Decay. *American Journal of Physics*, 36(12):1150–1160, 1968.
- [14] G M Lewis. *Neutrinos*. Wykeham publications, London; Winchester, 1970.

- [15] C M G Lattes, et al. Processes Involving Charged Mesons. *Nature*, 159:694–697, 1947.
- [16] C M G Lattes, G P S Occhialini, and C F Powell. Observations on the Tracks of Slow Mesons in Photographic Emulsions. 1. *Nature*, 160:453–456,486–492, 1947.
- [17] R Brown, et al. Observations With Electron Sensitive Plates Exposed to Cosmic Radiation. *Nature*, 163:82, 1949.
- [18] C L Cowan, et al. Large Liquid Scintillation Detectors. *Phys. Rev.*, 90(3):493–494, 1953.
- [19] F. Reines and C. L. Cowan. A proposed experiment to detect the free neutrino, 1953.
- [20] F. Reines and C. L. Cowan. Detection of the free neutrino. *Physical Review*, 92(3):830–831, 1953.
- [21] C L Cowan, et al. Detection of the Free Neutrino: a Confirmation. *Science*, 124(3212):103–104, 1956.
- [22] Raymond Davis Jr. and Don S Harmer. Attempt to observe the  $\text{Cl}^{37}(\bar{\nu}e^-)\text{Ar}^{37}$  reaction induced by reactor antineutrinos. *Bull. Am. Phys. Soc.*, 4:217, 1959.
- [23] G Danby, et al. Observation of High-Energy Neutrino Reactions and the Existence of Two Kinds of Neutrinos. *Phys. Rev. Lett.*, 9(1):36–44, 1962.
- [24] M. L. Perl, et al. Evidence for anomalous lepton production in  $e^+e^-$  annihilation. *Physical Review Letters*, 35(22):1489–1492, 1975.
- [25] G J Feldman, et al. Inclusive Anomalous Muon Production in  $e^+e^-$  Annihilation. *Phys. Rev. Lett.*, 38(3):117–120, 1977.
- [26] J Burmester, et al. Anomalous muon production in  $e^+e^-$  annihilations as evidence for heavy leptons. *Physics Letters B*, 68(3):297–300, 1977.
- [27] D. DeCamp, et al. Determination of the number of light neutrino species. *Physics Letters B*, 231(4):519–529, 1989.
- [28] B Adeva, et al. A determination of the properties of the neutral intermediate vector boson Z0. *Physics Letters B*, 231(4):509–518, 1989.
- [29] M Z Akrawy, et al. Measurement of the Z0 mass and width with the opal detector at LEP. *Physics Letters B*, 231(4):530–538, 1989.
- [30] P Aarnio, et al. Measurement of the mass and width of the Z0-particle from multi-hadronic final states produced in  $e^+e^-$  annihilations. *Physics Letters B*, 231(4):539–547, 1989.
- [31] S. Schael, et al. Precision electroweak measurements on the Z resonance. *Physics Reports*, 427(5-6):257–454, 2006.
- [32] K. Kodama, et al. Observation of tau neutrino interactions. *Physics Letters, Section B: Nuclear, Elementary Particle and High-Energy Physics*, 504(3):218–224, 2001.

- [33] H A Bethe. Energy Production in Stars. *Phys. Rev.*, 55(5):434–456, 1939.
- [34] John N Bahcall, Neta A Bahcall, and Giora Shaviv. Present Status of the Theoretical Predictions for the  $^{37}\text{Cl}$  Solar-Neutrino Experiment. *Phys. Rev. Lett.*, 20(21):1209–1212, 1968.
- [35] John N. Bahcall, Aldo M. Serenelli, and Sarbani Basu. New Solar Opacities, Abundances, Helioseismology, and Neutrino Fluxes. *The Astrophysical Journal*, 621(1):L85–L88, 2005.
- [36] B. T. Cleveland, et al. Update on the measurement of the solar neutrino flux with the Homestake chlorine detector. *Nuclear Physics B (Proceedings Supplements)*, 38(1-3):47–53, 1995.
- [37] John N Bahcall, M H Pinsonneault, and G J Wasserburg. Solar models with helium and heavy-element diffusion. *Rev. Mod. Phys.*, 67(4):781–808, 1995.
- [38] J. N. Abdurashitov, et al. Results from SAGE (The Russian-American gallium solar neutrino experiment). *Physics Letters B*, 328(1-2):234–248, 1994.
- [39] P. Anselmann, et al. Solar neutrinos observed by GALLEX at Gran Sasso. *Physics Letters B*, 285(4):376–389, 1992.
- [40] W. Hampel, et al. GALLEX solar neutrino observations: Results for GALLEX IV. *Physics Letters, Section B: Nuclear, Elementary Particle and High-Energy Physics*, 447:127–133, 1999.
- [41] E. Gaisser, T. K.; Engel, R.; Resconi. *Cosmic Rays and Particle Physics*. Cambridge University Press, 1990.
- [42] T J Haines, et al. Calculation of Atmospheric Neutrino-Induced Backgrounds in a Nucleon-Decay Search. *Phys. Rev. Lett.*, 57(16):1986–1989, 1986.
- [43] K S Hirata, et al. Experimental study of the atmospheric neutrino flux. *Physics Letters B*, 205(2):416–420, 1988.
- [44] W Anthony Mann. Atmospheric neutrinos and the oscillations bonanza. *Int. J. Mod. Phys.*, A15S1:229–256, 2000.
- [45] B Pontecorvo. Neutrino Experiments and the Problem of Conservation of Leptonic Charge. *Sov. Phys. JETP*, 26:984–988, 1968.
- [46] V Gribov and B Pontecorvo. Neutrino astronomy and lepton charge. *Physics Letters B*, 28(7):493–496, 1969.
- [47] B Pontecorvo. Mesonium and anti-mesonium. *Sov. Phys. JETP*, 6:429, 1957.
- [48] D Casper, et al. Measurement of atmospheric neutrino composition with the IMB-3 detector. *Phys. Rev. Lett.*, 66(20):2561–2564, 1991.
- [49] R Becker-Szendy, et al. Electron- and muon-neutrino content of the atmospheric flux. *Phys. Rev. D*, 46(9):3720–3724, 1992.

- [50] Y Fukuda, et al. Atmospheric  $\nu\mu/\nu e$  ratio in the multi-GeV energy range. *Physics Letters B*, 335(2):237–245, 1994.
- [51] J N Bahcall. Solar Models and Solar Neutrinos. *Physica Scripta*, 2005(T121):46, 2005.
- [52] Ziro Maki, Masami Nakagawa, and Shoichi Sakata. Remarks on the Unified Model of Elementary Particles. *Progress of Theoretical Physics*, 28(5):870, 1962.
- [53] John N Bahcall, Concepción M Gonzalez-Garcia, and Carlos Pena-Garay. Before and After: How has the SNO NC measurement changed things? *Journal of High Energy Physics*, 2002(07):54, 2002.
- [54] A Yu. Smirnov. The MSW effect and solar neutrinos. In *Neutrino telescopes. Proceedings, 10th International Workshop, Venice, Italy, March 11–14, 2003. Vol. 1+2*, pages 23–43, 2003.
- [55] L Wolfenstein. Neutrino oscillations in matter. *Phys. Rev. D*, 17(9):2369–2374, 1978.
- [56] S P Mikheev and A Yu. Smirnov. Resonance Amplification of Oscillations in Matter and Spectroscopy of Solar Neutrinos. *Sov. J. Nucl. Phys.*, 42:913–917, 1985.
- [57] S P Mikheev and A Yu. Smirnov. Resonant amplification of neutrino oscillations in matter and solar neutrino spectroscopy. *Nuovo Cim.*, C9:17–26, 1986.
- [58] K Eguchi, et al. First Results from KamLAND: Evidence for Reactor Antineutrino Disappearance. *Phys. Rev. Lett.*, 90(2):21802, 2003.
- [59] T Araki, et al. Measurement of Neutrino Oscillation with KamLAND: Evidence of Spectral Distortion. *Phys. Rev. Lett.*, 94(8):81801, 2005.
- [60] Abhijit Bandyopadhyay, et al. The Solar neutrino problem after the first results from KamLAND. *Phys. Lett.*, B559:121–130, 2003.
- [61] Pedro Cunha de Holanda and A Yu. Smirnov. LMA MSW solution of the solar neutrino problem and first KamLAND results. *JCAP*, 0302:1, 2003.
- [62] G L Fogli, et al. Evidence for Mikheyev-Smirnov-Wolfenstein effects in solar neutrino flavor transitions. *Phys. Lett.*, B583:149–156, 2004.
- [63] Thomas Mannel. Theory and Phenomenology of CP Violation. *Nuclear Physics B - Proceedings Supplements*, 167:115–119, 2007.
- [64] Tommy Ohlsson, He Zhang, and Shun Zhou. Radiative corrections to the leptonic Dirac CP-violating phase. *Phys. Rev. D*, 87(1):13012, 2013.
- [65] Tommy Ohlsson, He Zhang, and Shun Zhou. Probing the leptonic Dirac CP-violating phase in neutrino oscillation experiments. *Physical Review D - Particles, Fields, Gravitation and Cosmology*, 87(5):1–8, 2013.
- [66] DUNE Collaboration. Long-Baseline Neutrino Facility (LBNF) and Deep Underground Neutrino Experiment (DUNE): The LBNF and DUNE Projects. 1, 2016.

- [67] K Abe, et al. Physics potential of a long-baseline neutrino oscillation experiment using a J-PARC neutrino beam and Hyper-Kamiokande. *Progress of Theoretical and Experimental Physics*, 2015(5):053C02, 2015.
- [68] F Kaether, et al. Reanalysis of the Gallex solar neutrino flux and source experiments. *Physics Letters B*, 685(1):47–54, 2010.
- [69] J N Abdurashitov, et al. Measurement of the solar neutrino capture rate with gallium metal. III. Results for the 2002–2007 data-taking period. *Phys. Rev. C*, 80(1):15807, 2009.
- [70] B Aharmim, et al. Combined analysis of all three phases of solar neutrino data from the Sudbury Neutrino Observatory. *Phys. Rev. C*, 88(2):25501, 2013.
- [71] A Gando, et al. Reactor on-off antineutrino measurement with KamLAND. *Phys. Rev. D*, 88(3):33001, 2013.
- [72] R Wendell, et al. Atmospheric neutrino oscillation analysis with subleading effects in Super-Kamiokande I, II, and III. *Phys. Rev. D*, 81(9):92004, 2010.
- [73] M G Aartsen, et al. Determining neutrino oscillation parameters from atmospheric muon neutrino disappearance with three years of IceCube DeepCore data. *Phys. Rev. D*, 91(7):72004, 2015.
- [74] P Adamson, et al. Measurement of Neutrino and Antineutrino Oscillations Using Beam and Atmospheric Data in MINOS. *Phys. Rev. Lett.*, 110(25):251801, 2013.
- [75] P Adamson, et al. Electron Neutrino and Antineutrino Appearance in the Full MINOS Data Sample. *Phys. Rev. Lett.*, 110(17):171801, 2013.
- [76] K Abe, et al. Precise Measurement of the Neutrino Mixing Parameter  $\theta_{23}$  from Muon Neutrino Disappearance in an Off-Axis Beam. *Phys. Rev. Lett.*, 112(18):181801, 2014.
- [77] P Adamson, et al. First measurement of muon-neutrino disappearance in NOvA. *Phys. Rev. D*, 93(5):51104, 2016.
- [78] M C Gonzalez-Garcia, Michele Maltoni, and Thomas Schwetz. Updated fit to three neutrino mixing: status of leptonic CP violation. *Journal of High Energy Physics*, 2014(11):52, 2014.
- [79] Ivan Esteban, et al. Updated fit to three neutrino mixing: exploring the accelerator-reactor complementarity. *Journal of High Energy Physics*, 2017(1):87, 2017.
- [80] F P An, et al. Observation of Electron-Antineutrino Disappearance at Daya Bay. *Phys. Rev. Lett.*, 108(17):171803, 2012.
- [81] J K Ahn, et al. Observation of Reactor Electron Antineutrinos Disappearance in the RENO Experiment. *Phys. Rev. Lett.*, 108(19):191802, 2012.
- [82] K Abe, et al. Observation of Electron Neutrino Appearance in a Muon Neutrino Beam. *Phys. Rev. Lett.*, 112(6):61802, 2014.

- [83] P Adamson, et al. First Measurement of Electron Neutrino Appearance in NOvA. *Phys. Rev. Lett.*, 116(15):151806, 2016.
- [84] K Abe, et al. Combined Analysis of Neutrino and Antineutrino Oscillations at T2K. *Phys. Rev. Lett.*, 118(15):151801, 2017.
- [85] V N Aseev, et al. Upper limit on the electron antineutrino mass from the Troitsk experiment. *Phys. Rev. D*, 84(11):112003, 2011.
- [86] Ch Kraus, et al. Final results from phase II of the Mainz neutrino mass search in tritium  $\beta$ -decay. *The European Physical Journal C - Particles and Fields*, 40(4):447–468, 2005.
- [87] Planck Collaboration, et al. Planck 2013 results. XVI. Cosmological parameters. *Astronomy & Astrophysics*, 571:A16, 2014.
- [88] DUNE Collaboration. Long-Baseline Neutrino Facility (LBNF) and Deep Underground Neutrino Experiment (DUNE): The Physics Program for DUNE at LBNF. 2, 2015.
- [89] DUNE Collaboration. Long-Baseline Neutrino Facility (LBNF) and Deep Underground Neutrino Experiment (DUNE): Long Baseline Neutrino Facility for DUNE. 3, 2016.
- [90] DUNE Collaboration. Long-Baseline Neutrino Facility (LBNF) and Deep Underground Neutrino Experiment (DUNE): The DUNE Detectors at LBNF. 4, 2016.
- [91] S. Amerio, et al. Design, construction and tests of the ICARUS T600 detector. *Nuclear Instruments and Methods in Physics Research, Section A: Accelerators, Spectrometers, Detectors and Associated Equipment*, 527(3):329–410, 2004.
- [92] C Anderson, et al. The ArgoNeuT detector in the NuMI low-energy beam line at Fermilab. *Journal of Instrumentation*, 7(10):P10019, 2012.
- [93] F Cavanna, et al. LArIAT: Liquid Argon In A Testbeam. 2014.
- [94] R Acciarri, et al. Design and construction of the MicroBooNE detector. *Journal of Instrumentation*, 12(02):P02017, 2017.
- [95] B Baller, et al. Liquid Argon Time Projection Chamber research and development in the United States. *Journal of Instrumentation*, 9(05):T05005, 2014.
- [96] David R Nygren. The Time Projection Chamber - A New 4pi Detector for Charged Particles. *eConf*, C740805(PEP-0144):58–78, 1974.
- [97] Carlo Rubbia. The Liquid Argon Time Projection Chamber: A New Concept For Neutrino Detectors.pdf, 1977.
- [98] Mitch Soderberg. The MicroBooNE Proposal, 2008.
- [99] V Chepel and H Araújo. Liquid noble gas detectors for low energy particle physics. *Journal of Instrumentation*, 8(04):R04001, 2013.

- [100] P. Derwent, et al. Proton Improvement Plan-II (PIP-II). Technical Report December, 2013.
- [101] Patrick Huber and Joachim Kopp. Two experiments for the price of one? The role of the second oscillation maximum in long baseline neutrino experiments. *Journal of High Energy Physics*, 2011(3):13, 2011.
- [102] LBNE Collaboration. Long-Baseline Neutrino Experiment (LBNE) Project: The LBNE Project. 1, 2012.
- [103] LBNE Collaboration. Long-Baseline Neutrino Experiment (LBNE) Project: Detectors At The Near Site. 3, 2012.
- [104] LBNE Collaboration. Long-Baseline Neutrino Experiment (LBNE) Project: Liquid Argon Detector At The Far Site. 4, 2012.
- [105] Margherita Buizza Avanzini. The LAGUNA-LBNO Project. *Physics Procedia*, 61:524–533, 2015.
- [106] HEPAP Subcommittee. Building for Discovery: Strategic Plan for U.S. Particle Physics in the Global Context. 2014.
- [107] M. Convery and Z. Djurcic. The 35-Ton Liquid Argon TPC Prototype for the Long Baseline Neutrino Experiment (Poster). In *Neutrino 2014 Conference Proceedings*, 2014.
- [108] T Kutter. Proposal for a Full-Scale Prototype Single-Phase Liquid Argon Time Projection Chamber and Detector Beam Test at CERN. Technical Report CERN-SPSC-2015-020. SPSC-P-351, CERN, Geneva, 2015.
- [109] I De Bonis and Others. LBNO-DEMO: Large-scale neutrino detector demonstrators for phased performance assessment in view of a long-baseline oscillation experiment. 2014.
- [110] CERN Courier. Neutrinos take centre stage.
- [111] D Finley, et al. Work at FNAL to achieve long electron drift lifetime in liquid argon. 2006.
- [112] R Andrews, et al. A system to test the effects of materials on the electron drift lifetime in liquid argon and observations on the effect of water. *Nucl. Instrum. Meth.*, A608:251–258, 2009.
- [113] A Curioni, et al. A regenerable filter for liquid argon purification. *Nuclear Instruments and Methods in Physics Research Section A: Accelerators, Spectrometers, Detectors and Associated Equipment*, 605(3):306–311, 2009.
- [114] B Rebel, et al. Results from the Fermilab materials test stand and status of the liquid argon purity demonstrator. *J. Phys. Conf. Ser.*, 308:12023, 2011.
- [115] P Cennini, et al. Argon purification in the liquid phase. *Nuclear Instruments and Methods in Physics Research Section A: Accelerators, Spectrometers, Detectors and Associated Equipment*, 333(2):567–570, 1993.

- [116] P Benetti, et al. A three-ton liquid argon time projection chamber. *Nuclear Instruments and Methods in Physics Research Section A: Accelerators, Spectrometers, Detectors and Associated Equipment*, 332(3):395–412, 1993.
- [117] F Arneodo, et al. Performance of a liquid argon time projection chamber exposed to the CERN West Area Neutrino Facility neutrino beam. *Phys. Rev. D*, 74(11):112001, 2006.
- [118] G Carugno, et al. Electron lifetime detector for liquid argon. *Nuclear Instruments and Methods in Physics Research Section A: Accelerators, Spectrometers, Detectors and Associated Equipment*, 292(3):580–584, 1990.
- [119] Terry Tope and Others. Extreme argon purity in a large, non-evacuated cryostat. *AIP Conf. Proc.*, 1573:1169–1175, 2014.
- [120] M Adamowski, et al. The Liquid Argon Purity Demonstrator. *Journal of Instrumentation*, 9(07):P07005, 2014.
- [121] C Bromberg, et al. Design and operation of LongBo: a 2 m long drift liquid argon TPC. *Journal of Instrumentation*, 10(07):P07015, 2015.
- [122] David Montanari and Others. First scientific application of the membrane cryostat technology. *AIP Conf. Proc.*, 1573:1664–1671, 2014.
- [123] Alan Hahn, et al. The LBNE 35 Ton Prototype Cryostat. In *Proceedings, 21st Symposium on Room-Temperature Semiconductor X-ray and Gamma-ray Detectors (RTSD 2014): Seattle, WA, USA, November 8-15, 2014*, page 7431158, 2014.
- [124] David Montanari, et al. Performance and results of the LBNE 35 ton membrane cryostat prototype. *Physics Procedia*, 67:308–313, 2015.
- [125] Fermi National Accelerator Laboratory Visual Media Services, 2015.
- [126] T Alion. 35~ton Geometry, 2014.
- [127] 35ton. 35 ton Photon Detectors. *NOT PUBLISHED YET*.
- [128] M. Stancari. 35 ton Counter Locations, 2015.
- [129] D S Akerib and Others. LUX-ZEPLIN (LZ) Conceptual Design Report. 2015.
- [130] A Blatter, et al. Experimental study of electric breakdowns in liquid argon at centimeter scale. *Journal of Instrumentation*, 9(04):P04006, 2014.
- [131] N McConkey, et al. Cryogenic CMOS cameras for high voltage monitoring in liquid argon. *Journal of Instrumentation*, 12(03):P03014, 2017.
- [132] 35~ton Phase~II LAr filling monitored by camera system, 2016.
- [133] L Bagby, et al. 35~ton Noise. *DUNE Document Database*, 1834, 2016.
- [134] J. Freeman. Courtesy of John Freeman, Fermilab, 2014.